行政院原子能委員會

委託研究計畫研究報告

LSM 鍍層對 SOFC 接合件高溫機械性質之影響

Effect of LSM Coating on High-Temperature Mechanical Properties of SOFC Joint

計畫編號：**1062001INER008**

受委託機關(構)：國立中央大學

計畫主持人：林志光 教授

聯絡電話：**03-4267340**

E-mail address：**t330014@cc.ncu.edu.tw**

協同主持人：

研究期程：中華民國 **106** 年 **3** 月至 **106** 年 **12** 月

研究經費：新臺幣柒拾貳萬元

核研所聯絡人員：吳思翰

報告日期：**106** 年 **11** 月 **30** 日

目錄

中文摘要

本研究目的在探討錳鈷酸鑭鍍層對於固態氧化物燃料電池玻璃陶瓷接合劑和金屬連接板接合件的潛變性質與破壞模式之影響，所使用的玻璃陶瓷為核能研究所開發一款代號為 GC-9 的材質，LSM 鍍層材質為 $La_{0.67}Sr_{0.33}MnO_3$，金屬連接板則是使用代號為 Crofer 22 H 的商用肥粒鐵系不銹鋼。在 800 ℃ 的氧化環境下，對於接合件施予剪力及張力固定負載來進行潛變實驗並量測其室溫及 800 ℃ 下的張力與剪力強度，同時評估氧化環境時效處理對接合件機械強度及潛變性質的影響，並比較未含有鍍層及含有鍍層接合件之高溫機械強度與潛變性質的差異。

實驗結果顯示，含有 LSM 鍍層與未含有 LSM 鍍層的未時效試片相比較，其剪力強度在常溫及 800 ℃ 分別下降約 78%與 92%，而張力強度在常溫及 800 ℃ 分別下降約 59%與 72%。試片在高溫接合過程中，鑭元素從 LSM 鍍層中擴散並與 GC-9 玻璃陶瓷反應生成稀土氧基磷灰石層 ($Ca_2La_8(SiO_4)_6O_2$)。此氧化層的形成及結晶化後的結構體積收縮以及與 GC-9 玻璃陶瓷和 Crofer 22 H 的熱膨脹係數不匹配導致微孔洞的產生，進而主導了接合件的破裂模式。另一方面，潛變試驗的結果顯示不論在未時效及 1000 小時時效處理後，接合件於 800 ℃ 氧化環境下的剪力及張力潛變壽命皆隨著負載減少而增加。未時效剪力試片具 1000 小時壽命的潛變強度約為剪力接合件強度的 42%，而未時效張力試片具 1000 小時壽命的潛變強度則約為張力接合件強度的 3%。與未時效且未含有鍍層之接合件相比，含有 LSM 鍍層之接合件具 1000 小時壽命的剪力及張力潛變強度分別下降約 85%與 89%。含有 LSM 鍍層的張力與剪力接合件，隨著潛變時間增加，由破裂於氧基磷灰石層中，轉變為氧基磷灰石與鉻酸鋇($BaCrO_4$)的介面。

經 1000 小時氧化環境時效處理後，含有 LSM 鍍層的接合件其剪力強度不論在常溫及高溫下皆提升，相同的時效處理提升了常溫下的張力強度卻降低了其高溫下的機械強度。在潛變強度方面，時效剪力試片具 1000 小

時壽命的潛變強度較未時效試片提升約 13%，而時效張力試片具 1000 小時壽命的潛變強度較未時效試片提升約 216%。藉由觀察破斷面微結構發現，時效張力試片在高溫下的破裂位置由氧基磷灰石與鉻酸鋇的介面，轉變為氧基磷灰石與尖晶石($(Cr,Mn)_3O_4$)的介面。此現象顯示氧基磷灰石與尖晶石的介面對張應力較為敏感，並在承受張應力時為接合件中最為脆弱的介面層。對於時效處理試片而言，氧基磷灰石與鉻酸鋇層主導了時效剪力試片的潛變破裂模式，而對於張應力較敏感的尖晶石層則與其他氧化層同時主導了時效張力試片的潛變破裂模式。

Abstract

The objective of this study is to investigate the effect of LSM coating on the creep properties of a SOFC joint between a glass-ceramic sealant and an interconnect steel with no and 1000-h thermal aging in air. The materials used are a GC-9 glass-ceramic sealant developed at the Institute of Nuclear Energy Research and a commercial Crofer 22 H ferritic steel. The creep test is conducted by applying a constant load (shear or tensile mode) on the joint at 800 ℃. Comparison of the joint strength and creep properties between LSM-coated and non-coated specimens is also made for the non-aged condition.

With the LSM coating, the shear strength of the non-aged joint specimen is reduced by 78% and 92% at RT and 800 ℃, respectively. On the other hand, the tensile strength of the joint is reduced by 59% and 72% at RT and 800 ℃, respectively. During the joining process, La diffuses out from LSM film and reacts with GC-9 to form a rare-earth oxyapatite ceramic. Volume shrinkage during crystallization of oxyapatite and thermal mismatch at high operation temperature lead to the formation of microcracks and the fracture is mainly related to this oxyapatite phase.

The creep rupture time of LSM-coated joint is increased with a decrease in the applied constant shear and tensile loading at 800 ℃ regardless of thermal aging condition. The shear creep strength of non-aged joint at 1000 h in air is about 42% of the average shear strength, while the tensile creep strength at 1000 h is only about 3% of the average tensile strength. Compared to the non-aged, non-coated specimens, the creep strength at 1000 h for the LSM-coated shear and tensile specimens is significantly reduced by 85% and 89% at 800 ℃, respectively. For both non-aged shear and tensile specimens with a short creep

rupture time less than 100 h, fracture mainly takes place in the oxyapatite layer. For a medium-term creep rupture time (100 h < t_r < 1000 h), fracture site changes from the oxyapatite interlayer to the mixed oxyapatite/$BaCrO_4$ layer with an increase of creep rupture time to exceed 100 h.

A thermal aging treatment at 800 ℃ for 1000 h significantly enhances the joint strength of shear specimen at RT and 800 ℃. However, a similar thermal aging treatment enhances the joint strength of tensile specimen at RT but degrades it at 800 ℃. For tensile loading mode, fracture site changes from the interface between GC-9/oxyapatite and $BaCrO_4$ to the interface between GC-9/oxyapatite and $(Cr,Mn)_3O_4$ when the testing temperature increases from RT to 800 ℃. The interface between GC-9/oxyapatite and $(Cr,Mn)_3O_4$ becomes the weakest path when subjected to tensile loading at high temperature.

After 1000-h thermal aging, the shear and tensile creep strength at 1000 h of the thermally aged joint is enhanced by 13% and 216%, respectively, compared to the non-aged counterparts. Oxyapatite and $BaCrO_4$ dominate the creep failure mechanism for 1000 h-aged shear specimens, while the $(Cr,Mn)_3O_4$ spinel layer becomes thicker after thermal aging and might also play a role in the creep failure of 1000-h aged tensile specimens in addition to the oxyapatite and $BaCrO_4$ phases.

1. INTRODUCTION

1.1. Solid Oxide Fuel Cell

Solid Oxide Fuel Cell (SOFC) is a solid state device that generates electricity through an electrochemical reaction between fuel and oxidant at high temperature. It is the most promising candidate for future energy conversion technology. It converts chemical energy directly into electrical energy by series reactions. Therefore, SOFCs have a higher efficiency and low pollutant emission than traditional power generation systems. Compared with other fuel cells, SOFCs have several advantages: (1) the electrolyte is made of solid oxides such that it can prevent leakage or evaporation; (2) utilization of fuel is flexible, such as pure hydrogen or hydrocarbon; (3) because of a high operation temperature of 600 ℃-1000 ℃, electrochemical reactions directly occur without noble catalyst and fuel can be internally reformed without complex external reformer [1].

The general operating principle of SOFC using hydrogen as fuel is shown in Fig 1 [2]. There are two gas flows in SOFC, namely fuel and air. Hydrogen as the fuel flows into the anode side of the cell for an oxidation reaction. On the other hand, air is fed to the cathode that accepts electrons from the external circuit and undergoes a reduction reaction. The electrochemical reactions involved are expressed below,

Anode: $H_2 + O^{2-} \rightarrow H_2O + 2e^-$ (1)

Cathode: $\frac{1}{2}O_2 + 2e^- \rightarrow O^{2-}$ (2)

Overall: $H_2 + \frac{1}{2}O_2 \rightarrow H_2O$ (3)

There are two typical configuration designs for SOFC, namely tubular and planar cells. Recently, planar SOFCs (pSOFCs) attract more attention than tubular ones because of easy fabrication and lower ohmic loss which contribute to low cost and higher efficiency. Figure 2 shows the structural design of a typical pSOFC stack [3]. A typical unit cell of pSOFC consists of a positive electrode-electrolyte-negative electrode (PEN) plate, interconnects, a nickel mesh, and sealants. In order to increase the power density and fulfill the requirement of electrical application, several unit cells are connected in series by interconnects and sealants. The roles of interconnect in SOFCs are the electrical connection between cells and the separation of fuel and oxidant gas. It must have high electric conductivity and chemical stability in both oxidizing and

reducing environments as well as thermal expansion match with other components at high operating temperature. A nickel mesh is inserted in the middle between interconnect and PEN plate as a current collector. The hermetic sealant is another crucial part in pSOFCs. Sealant must also be stable in both fuel and oxidant gas sides and prevent from leakage and mixing. Undesired chemical reaction and mismatch of coefficient of thermal expansion (CTE) between interconnect and sealant may cause damages in a pSOFC stack leading to degradation of cell performance.

1.2. Glass Sealant

The development of suitable sealants for long-term performance stability of SOFC is a major challenge. Sealants must have good resistance to both oxidizing and reducing environments and chemical compatibility with adjacent components. Furthermore, the electrical insulation is also required to avoid short circuits when stacking cells and interconnects [4]. Sealants for SOFC can be classified into two main groups, namely rigid and compressive seals. The compressive seals, such as mica and metallic seals, allow a difference in CTE and close the gap between adjacent components to prevent leakage in stack. However, this type of sealant must be deformed by applying compressive stress to tight the seals, which results in a difficulty of assembling and choosing of material [5]. Another group of sealant is rigid seal which can be further divided to glass, glass-ceramic, and brazing. The glass and glass-ceramic seals are hermetic and they may crystalize during the operation of SOFC to form a more rigid glass-ceramic seal [6]. The CTE of sealants must be compatible with other neighboring components like electrode and interconnect to reduce thermal stress. During thermal cycles of SOFC operation, thermal stresses are generated due to thermal mismatch and may cause crack formation leading to failure of sealant. Another system of rigid seal is braze sealing. This sealing technology creates a bond on cooling and solidification of a braze alloy which is melted and reacts with the surface of joining material. Because of lower stiffness and higher mechanical strength, braze seals can undergo plastic deformation and sustain the thermal stresses generated by thermal mismatch. However, in order to meet the requirement of chemical stability in a dual atmosphere, the material of braze sealing normally uses expensive silver or gold with other oxide mixture to form a metal oxide-noble metal system, which results in much higher cost compared to glass and glass-ceramic systems [7].

Thanks to low cost and effective manufacturing process, glass and

glass-ceramic sealants are the most common materials used in pSOFC stacks. Two important properties for design of suitable glass sealant are the glass transition temperature (T_g) and CTE [5]. T_g is a temperature at which glass starts to become viscous and can flow to create a hermetic seal between the components. In addition, this property provides a self-healing effect of seal which can release thermal stress and heal cracks that are generated by thermal mismatch [8]. Therefore, T_g of glass sealant must be lower than the operation temperature of SOFC.

During the long-term operation at high temperature, glass phase will crystallize and become glass-ceramic, which will increase the mechanical strength of sealant. At the same time, the remaining glass still has the viscosity and keeps the integrity of sealant. However, material properties like CTE and T_g change over time during crystallization process. These changes may generate additional thermal stresses in the sealants or at the interfaces with other components. Therefore, it is important to control the crystallization of glass phase so that the glass-ceramic can have both flowability and stiffness satisfying the requirement of stack integrity.

Several systems of glass sealant have been developed for pSOFC stack such as phosphate, borosilicate, boroaluminosilicat, and silicate glasses and glass-ceramics [3,6]. Recently, most of the research has been focused on BaO-containing glass systems because of lower activation energy for crystallization of barium, which results in more crystallization and low crystallizing temperature [5]. In addition, adding BaO content tends to reduce the values of T_g and softening temperature (T_s), while at the same time CTE is increased by formation of barium silicate ($BaSiO_3$) [5,8]. However, BaO could easily react with Cr at the interface of metallic interconnect leading to formation of barium chromate ($BaCrO_4$). The CTE of $BaCrO_4$ (around 20×10^{-6} $℃^{-1}$) is significantly higher than glass and other crystalline phases resulting in detachment and spallation of the sealant [8,9]. Therefore, other research is focused on the glass with low barium content or other elements that could replace Ba. Listed in Table 1 are some common composition modifiers added in glass-ceramic sealants to improve chemical and mechanical properties [10].

Recently, Institute of Nuclear Energy Research (INER) has developed a new glass sealant (designated as GC-9) of the BaO-B_2O_3-Al_2O_3-SiO_2 system for use in intermediate-temperature pSOFC (IT-pSOFC) at 700 ℃-750 ℃. Properties of this glass sealant such as CTE, viscosity, crystallization, and chemical interaction with other pSOFC components (electrolyte, electrode, interconnect, and frame) have been investigated [11-13]. In addition, high

temperature mechanical properties of this glass sealant has been studied by Chang [14]. In that study [14], to investigate the effect of crystallization, GC-9 glass powders were sintered at 850 ℃ for 4 h as non-aged condition and at 750 ℃ for 100 h as aged condition. Mechanical and thermal properties at different temperatures were measured. As a result, the flexure strength of both non-aged and aged samples increases with temperature below T_g due to a crack healing effect [14]. Crystalline phases in GC-9 glass enhance the flexural strength at 650 ℃-700 ℃ leading to a comparable or greater strength than that at room temperature [14]. However, because of viscous effect at temperature above T_g, the flexural strength and elastic modulus are reduced for both non-aged and aged conditions and are lower than those at room temperature when the testing temperature increases to 800 ℃ [14]. On the other hand, aged GC-9 exhibits a greater strength and stiffness than non-aged one at temperature above 700 ℃ because of a greater extent of crystallization.

1.3. Protective Coating on Metallic Interconnect

With a reduction of SOFC operating temperature to the range of 600 ℃-800 ℃, metallic alloys become the most promising candidate material to replace the traditional ceramic interconnect due to lower cost, better manufacturability, higher electrical conductivity, and high mechanical strength. Recently, ferritic stainless steels with high Cr concentration have been practically applied in SOFC interconnect due to their high oxidation resistance at high temperature and match of CTE with other components [15,16]. However, Cr-containing alloys have two major challenges, namely rapid chromium oxide (Cr_2O_3) scale growth and evaporation of Cr^{6+} species from interconnect into cathode [15]. The rapid Cr_2O_3 scale growth at high temperature leads to increase of area specific resistance (ASR) or spallation of interface between interconnect and other components. On the other hand, volatile Cr^{6+} species deposited on the surface of cathode also increases the electrical resistance. This phenomenon which is called Cr poisoning could result in degradation of cell performance and long-term durability of SOFC stack. To address these limitations, several approaches have been considered, such as developing new interconnect material with lower Cr concentration or using protective coating on interconnect. Recently, many researchers prefer to apply a coating on the interconnect and focus on developing effective and low-cost protective coatings [15-19].

The protective coating provides a layer which reacts with the surface of interconnect to decelerate oxide growth kinetics, increase electric conductivity,

improve the adhesion of oxide scale to metal, and decrease or inhibit the outer diffusion of Cr [15,16]. In addition, coating material should have good chemical stability and CTE match with adjacent components. To satisfy these requirements, several materials are considered, including reactive element oxides (REOs), rare earth perovskites, and composite spinel oxides [15,16,18,19]. The reactive elements, such as Ce, La, Y, Hf or their oxides, added into the coating system have been proved to reduce the high-temperature oxidation rate and contact resistance, as well as to restrict spallation between oxide scale and metal [15,16,19]. Because of great affinity for oxygen, reactive element ions which migrate through the scale grain boundaries to surface can block the short circuit paths and inhibit outward diffusion of oxide forming cations (i.e., Cr) [16]. It also prevents vacancy injection into interface and nucleation of interfacial voids [16]. However, REO coatings are normally thin (less than 0.2 μm) and porous and accordingly could not effectively serve as a Cr migration barrier. Another kind of coating material, rare earth perovskites, has a general formula of ABO_3 in which A is a trivalent rare earth cation (e.g. La, Y, or Sr) and B is a transition metal cation (e.g. Cr, Ni, Fe, Co, Cu, or Mn). This type of coating material exhibits p-electronic conduction in oxidizing environments and is stable in low oxygen partial pressure [15,16]. Perovskites can be doped with other elements such as Cu, Fe, and Ni to increase electric conductivity and modify CTE. In addition, perovskites containing reactive elements (e.g. La) can also decrease oxidation rate and improve oxide scale adhesion. As a result, application of this type of coating can improve oxidation behavior and CTE match and reduce the ASR. However, similar to REOs, perovskites cannot substantially inhibit Cr diffusion or absorb migrating Cr^{6+} species because of the ionically conducting nature in the rare earth perovskites leading to the Cr-poisoning of cathode [16]. Furthermore, this type of coating acts as an oxygen diffuser but not a barrier resulting in difficulty of depositing a fully dense layer. The composite spinel oxides, which have a general formula of AB_2O_4, attract more attention because of an excellent capability in suppressing volatile Cr^{6+} species from Cr_2O_3-rich scale to surface. A and B represents divalent, trivalent, or quadrivalent cations in octahedral and tetrahedral sites. The properties of spinel can be adjusted by substituting different A and B cations so as to have good electric conductivity and excellent CTE match with ferritic stainless steels and other cell components, including anode and cathode. Listed in Table 2 are comparison of various coatings in terms of electric conductivity, Cr migration inhibition, and oxidation rate reduction [15].

The rare earth perovskites and composite spinel oxides have been widely

studied in recent years due to their good electric conductivity and CTE match with other components in SOFC stack [20-30]. The effectiveness of rare earth perovskite coatings such as lanthanum chromite ($LaCrO_4$), lanthanum strontium chromite ($La_{1-x}Sr_xCrO_3$), lanthanum strontium manganite ($La_{1-x}Sr_xMnO_3$), and lanthanum strontium cobaltite ($La_{1-x}Sr_xCoO_3$) have been investigated [20-26]. In addition, various spinel coatings such as $(Mn,Co)_3O_4$, $MnCu_{0.5}Co_{1.5}O_4$, and $Cu_{0.5}Mn_{0.5}Fe_2O_4$ have also been investigated [27-30]. In the study of Palcut et al. [20], oxidation behavior of Crofer 22 APU, Crofer 22 H, E-Brite, and AL 29-4C steels coated with $La_{0.85}Sr_{0.15}MnO_{3-\delta}$ (LSM) were investigated. The results show that the LSM coating acts as an oxygen transport barrier and reduces oxygen partial pressure at the coating/chromium oxide scale interface leading to an improvement of electric conductivity [20]. In addition, a duplex oxide layer that has a small amount of manganese-chromium spinel phase is formed on the outer side of Cr_2O_3 in Crofer 22 APU and Crofer 22 H, which is referred to as Cr_2O_3-$(Cr,Mn)_3O_4$ [20]. This spinel phase has been proved that it can increase overall electric conductivity and prevent chromium evaporation at high temperature [20]. However, LSM has a relatively high cation diffusivity and oxide ion diffusivity along grain boundary at SOFC operating temperature so that it is not sufficient to inhibit the outward Cr diffusion completely. For composite spinel coating, Zhu et al. [27] revealed that CeO_2 doped $(Co,Mn)_3O_4$ spinel coating applied on Crofer 22 APU exhibits excellent performance in blocking Cr diffusion/migration and reducing Cr scale growth, leading to great electric conductivity and low ASR. Since each coating material has some drawbacks itself, some researchers focused on combining different materials into a composite layer [17,19,20,27]. Palcut et al. [20] revealed that the drawback of LSM coating, such as high oxide ion diffusivity, can be overcome by combining with materials of sufficiently small ionic diffusivity, e.g., spinels. On the other hand, doping reactive elements into perovskites and spinels can make an improvement in reducing the oxide scale growth and enhancing the adhesion of coating layer [17,19,27].

1.4. Joint of Glass-Ceramic Sealant and Metallic Interconnect

For IT-pSOFC systems, glass-ceramic sealants are commonly used to join metallic interconnects and frames. Figure 2 [3] shows the locations where glass-ceramic seals are applied to join metallic interconnects and metallic internal gas manifolds. Common seals include: (a) cell to metal frame; (b) metal

frame to metal interconnect; (c) frame/interconnect pair to electrically insulating spacer; (d) stack to base manifold plate [3]. Normally, metal frame and manifold plate are made of the same material as interconnect, so joints of (b) and (d) can be referred to as the joints of glass-ceramic sealant and metallic interconnect.

In the complex configuration of SOFC stack, interconnect/sealant interface plays a key role in the stack reliability, efficiency, and durability. During a long-term operation at high temperature, glass-ceramic sealant may have chemical reactions in itself and with metallic interconnect, which significantly affect the properties of their joint. In particular, the interfacial reaction between glass-ceramic and metallic interconnect often leads to formation of chromate phases with a relatively high CTE, which may result in separation of glass-ceramic sealant from metallic interconnect [31-35]. Recently, protective coatings are widely applied on metallic interconnect to avoid outward diffusion of Cr and cathode poisoning. Since any interaction between glass-ceramic sealant and interconnect will affect interfacial properties of their joint, the chemical reaction between protective coating and glass-ceramic sealant should also be considered. The compatibility of coated metallic interconnect with glass based sealant was investigated in a few studies [36-38]. It is suggested that reactions between protective coating, sealant, and interconnect should be limited; otherwise spallation and delamination at the interface may occur and lead to degradation of SOFC [36-38].

In addition to the undesired reactions mentioned above, thermal stresses may be generated during cyclic operation of SOFC leading the seals to be subjected to tensile and shear stresses [39,40]. Once the thermal stress exceeds the corresponding strength of joint, seals may fail resulting in leakage and degradation of cell performance. Therefore, it is necessary to investigate the mechanical properties of the joint between glass-ceramic sealant and metallic interconnect. Various testing techniques were applied to characterize the joint strength between glass-ceramic sealant and interconnect in SOFCs [31,35,41,42]. In the study of Malzbender et al. [41], symmetric shear test method was developed to characterize the shear strength of the joint between a glass-ceramic sealant (BaO-CaO-Al_2O_3-SiO_2, BCAS) and a metallic interconnect (Crofer 22 APU) [41]. Shear modulus and viscosity of the joint were also determined by a rheological model [41]. The results indicated that an additional annealing enhances crystallization leading to a higher shear modulus and shear strength [41]. On the other hand, Smeacetto et al. [42] designed sandwich-like samples with barium- and boron-free glass-ceramic sealant (SiO_2-Al_2O_3-CaO-Na_2O, SACN) and interconnect (Crofer 22 APU) to investigate bonding strength of

joint by a uni-axial tension test at room temperature (RT) [42]. The results revealed that fracture at RT occurred within the glass-ceramic layer rather than at the interface of interconnect and glass-ceramic [42].

Lin et al. [31,35] investigated both the tensile and shear joint strength of GC-9 glass-ceramic sealant and Crofer 22 H interconnect at RT and 800 ℃ in oxidizing and reducing environments. Their studies also considered the effect of thermal aging on the mechanical strength of joint in both environments for 1000 h at 800 ℃ [31,35]. The results revealed that both tensile and shear strengths at RT are higher than those at 800 ℃ in both environments [31,35]. It was found that the joint strength is similar between oxidizing and reducing environments due to a limited testing time at both RT and 800 ℃, and the fracture sites are also the same in both environments [31,35]. Fracture occurring within the glass-ceramic accompanies a greater joint strength, while a lower joint strength corresponds to fracture involving interfacial cracking at the interfaces of glass-ceramic/chromate or metal/chromia [31]. For specimens with a 1000-h thermal aging treatment, joint strength is decreased at 800 ℃ in both oxidizing and reducing environments compared to non-aged ones, indicating that thermal aging may generate detrimental effects for the joint [31,35]. Yeh [43] further investigated the effect of interconnect with LSM coating on shear and tensile joint strength at 800 ℃. Both tensile and shear strength of coated samples are significantly decreased compared to non-coated ones [43]. Analysis of interfacial microstructure revealed that such a coating dramatically degrades the joint strength because of generation of microvoids and microcracks in the chromate layer during sintering process [43].

1.5. Creep of Joint of Glass-Ceramic Sealant and Metallic Interconnect

Creep is referred to as the time-dependent deformation of a material subjected to constant stress/load at high temperature. The rate of deformation is a function of time, temperature, and applied load. For metals and crystalline ceramics, creep deformation is sufficiently large at a high temperature in the range of 30 to 60% of the melting temperature (T_m) in kelvin scale [44]. In addition, large creep strain can occur for glass and polymer at the temperature above T_g. Figure 3 [44] shows the strain versus time relation during creep under constant load. There is an initial instantaneous response of elastic and plastic strain, followed by a gradual accumulation of creep strain [44]. The strain rate is relatively high in primary stage but decreases and becomes approximately constant at secondary stage, which is called steady-state creep. At the end of

secondary stage, strain rate increases in an unstable manner and formation of necking or voids in material may occur resulting in rupture failure [44]. Figure 4 [44] shows the stress versus time to rupture (t_r) relation of S-590 alloy subjected to constant load at various temperatures. A stress versus t_r plot analogous to an *S-N* curve for fatigue, except that the life is a rupture time rather than a number of cycles [44].

As mentioned above, joint of sealant and interconnect plays an important role in reliability, efficiency, and durability of pSOFC system. Thermal stress generated in high-temperature operation of SOFC may not cause immediate failure of such a joint, but creep strain will accumulate during long-term steady-state operation leading to a possible final failure. Since it is difficult to repair a pSOFC stack during long-term operation, the creep properties of such a joint is important and need systematic investigations. High temperature creep properties of various components in pSOFC stack, such as anode, electrodes, glass-ceramic sealant, and metallic interconnect, have been investigated in a few studies [33,43,45-52]. Some of these studies investigated the creep properties of glass-ceramic sealant/interconnect joints in SOFC stacks [33,43,52].

In the study of Lin et al. [33], they investigated creep properties of a joint of metallic interconnect (Crofer 22 H) and glass-ceramic sealant (GC-9) at 800 ℃ in oxidizing environment. The shear creep strength at a creep life of 1000 h is about 25% of the average shear strength at 800 ℃ while the corresponding tensile creep strength is about 9% of the average tensile strength [33]. For both shear and tensile joint specimens, failure pattern shows that creep cracking initiates at the interface of spinel and $BaCrO_4$, penetrates through the $BaCrO_4$ layer, and propagates along the interface between the chromate layer and glass-ceramic substrate [33]. Finally, the fast fracture occurs within the glass-ceramic layer [33]. Furthermore, Hsu [52] investigated the environmental effect on the creep properties of the joint between glass-ceramic sealant and metallic interconnect. The shear and tensile creep strength at a creep life of 1000 h in a reducing environment is about 18% and 0.67% of the average shear and tensile joint strength, respectively [52]. Compared to the results of Lin et al. [33], it reveals that the creep resistance of the joint is significantly degraded when the testing environment is changed from oxidizing environment to reducing environment since the water in a given humidified hydrogen might relax joint structure [52].

With regard of thermal aging effect on the joint between glass-ceramic sealant and metallic interconnect, microstructure of glass-ceramic sealant might change during long-term operation of SOFC stack and affect the mechanical

strength and creep resistance. Hsu [52] further investigated the thermal aging effect on the creep properties of the joint between glass-ceramic sealant and metallic interconnect in reducing environment after 1000-h thermal aging. The results show that a thermal aging makes the amorphous glassy phase transform into crystalline phases and changes the flaw size and morphology [52]. Therefore, the fracture site for both non-aged tensile and shear specimens changes from the GC-9 layer to the interface of Cr_2O_3/GC-9 with an increase of creep rupture time up to 100 h [52]. With a longer in-situ thermal aging during creep test, water diffuses into the GC-9 layer to relax glass-ceramic structure, which causes the GC-9 glass-ceramic layer to become the weakest path for creep cracking in the non-aged joint with a creep rupture time over 100 h [52]. On the other hand, the shear and tensile creep strength of the 1000-h aged joint is about 49% and 38% of those without a thermal aging [52]. Microstructural analysis reveals that micro-voids are formed in the aged samples due to CTE difference between the ceramic and glassy phases [52]. Therefore, thermally aged joint has a lower creep strength [52].

1.6. Purpose

With a reduction of SOFC operating temperature to the range of 600 ℃-800 ℃, ferritic stainless steels with high Cr concentration have been practically applied in SOFC interconnect due to their high oxidation resistance at high temperature and match of CTE with other components. However, highly corrosive environment in high-temperature operation of SOFC causes the outward diffusion of Cr to form volatile Cr^{6+} species leading to degradation of cell performance and long-term durability of SOFC stack. Such a phenomenon is called Cr poisoning. Recently, LSM has been practically applied as a protective coating on metallic interconnect to prevent Cr poisoning and improve the long-term durability of SOFC. Oxidation behavior and microstructural characteristics of LSM coating have been investigated in a few studies [20-23,25]. As mentioned above, the undesired reactions may damage the joint of glass-ceramic sealant and metallic interconnect in pSOFC stacks leading to failure of seals. Although a few studies were focused on the mechanical properties of the joint between glass-ceramic sealant and LSM-coated metallic interconnect [43,53], study on the influence of the interaction between glass-ceramic sealant, metallic interconnect, and protective coating on creep behavior of such a joint is still lack. For these reasons, the objective of this study is to investigate the effect of LSM coating on the creep properties of a joint

between glass-ceramic sealant and metallic interconnect.

Two loading modes, tensile and shear force, are applied to characterize the creep properties of the joint at 800 ℃ in oxidizing environment. In addition, some specimens are tested after thermal aging at 800 ℃ for 1000 h in oxidizing environment to investigate the aging effect on the interaction between LSM coating and glass-ceramic sealant. Fractographic and microstructural analyses are conducted with scanning electron microscopy (SEM) and chemical composition within the interlayers are characterized using energy dispersive spectrum (EDS) and X-ray diffractometer (XRD). Microstructural analysis results are then correlated with creep testing results. It is hoped that results of the current study and previous work can provide an insight for assessing the long-term structural reliability of pSOFC stacks.

2. MATERIALS AND EXPERIMENTAL PROCEDURES

2.1. Materials and Specimen Preparation

In order to simulate the conditions of a joint subjected to thermal stresses at SOFC operation temperature, two types of sandwich-like specimens (metal/sealant/metal) are designed in this study for determining the creep properties of the joint and investigating the interfacial reactions. In this study, the metallic parts of the sandwich joint specimen are made of a commercial ferritic stainless steel, Crofer 22 H (ThyssenKrupp VDM GmbH, Werdohl, Germany), which is a heat-resistant alloy developed for application in SOFCs. Chemical compositions and mechanical properties of the Crofer 22 H alloy are listed in Tables 3 and 4 [54], respectively. As shown in Table 4, the yield strength, ultimate tensile strength, and Young's modulus of Crofer 22 H are decreased but the elongation is increased with an increase in temperature [54]. The GC-9 glass sealant used was developed at INER for IT-pSOFC. The major chemical composition of the GC-9 glass sealant includes 34 mol% BaO, 34 mol% SiO_2, 9.5 mol% B_2O_3, 12 mol% CaO, 5 mol% La_2O_3, 4.5 mol% Al_2O_3, and 1 mol% ZrO_2 [55]. It was made by mixing the constituent oxide powders followed by melting at 1550 ℃ for 10 h. After melting, it was poured into a mold preheated to 680 ℃ to produce GC-9 glass ingots. The GC-9 glass ingots were then annealed at 680 ℃ for 8 h and cooled down to RT. GC-9 glass powders were made by crushing the as-cast glass ingots and sieving with 325 mesh sieves. The average size of the glass powder is 45 μm. Slurries were made by adding into the GC-9 powders the desired amounts of solvent (alcohol), binder (ethyl celluloid), and plasticizer (polyethylene glycol). Table 5 [43] lists the average biaxial flexural strength of the sintered GC-9 glass at various temperatures.

Figure 5 shows the scheme of two types of joint specimens for tensile test (Fig. 5(a)) and shear test (Fig. 5(b)), respectively. The as-received metal plates were cut into slices in the dimensions of 95 mm x 25 mm x 2.5 mm. A pin hole was drilled in each steel slice for applying pin loading. It is effective to minimize bending and twisting effects during a creep test by means of pin loading. For shear specimens, an edge of each steel slice was milled from the original thickness of 2.5 mm to 1 mm with an area of about 8 mm x 25 mm. The apparent joining areas are 25 mm x 2.5 mm and 25 mm x 6 mm for tensile and shear specimens, respectively. After machining, a thin LSM layer was sputtered on the joining area first. The steel slices were deposited with $La_{0.67}Sr_{0.33}MnO_3$

using a pulsed direct current magnetron sputtering system (Fig. 6) in a vacuum chamber. A high-purity (99.9%) $La_{0.67}Sr_{0.33}MnO_3$ bulk (in sintered form) was used as the sputter target in the coating process. The distance between the specimen and the target is 5 cm. Sputter coating was performed in an argon atmosphere at a pressure of 0.99 Pa and a flow rate of 0.22 Pa m^3 s^{-1} for 90 min. The coated specimen was then calcined at 850 ℃ for 4 h to form a perovskite protecting layer. The thickness of LSM coated on the Crofer 22 H slice is about 3 μm. After the coating process, a GC-9 glass slurry was spread on the joining region of each steel slice to make a half-specimen. The glass slurry was made of a mixture of glass powder dispersed in ethanol. The half-specimen was then put in a furnace at 70 ℃ to dry the slurry.

A joint specimen was assembled by placing one half-specimen onto another half-specimen to form a Crofer 22 H/LSM/GC-9/LSM/Crofer 22 H sandwich specimen through designed heat treatments. Based on the assembling process developed for SOFC at INER, the joint specimens were firstly heated to 500 ℃ and held for 1 h and then heated to 900 ℃ followed by a hold time of 4 h. The heating rate at each heating step is 5 ℃/min. For investigating the effect of long-term operation in an oxidizing environment, some samples were thermally aged in air at 800 ℃ for 1000 h. The thermal aging treatment was carried out in a high-temperature box furnace. Photograph of this furnace is shown in Fig. 7.

2.2. Mechanical Testing

2.2.1. Tensile test

To determine the mechanical properties of the joint at RT and 800 ℃ in air, the shear and tensile joint specimens were tested under uni-axial loading on a commercial closed-loop servo-hydraulic test machine (MTS 810) attached with a high-temperature furnace (Model 653). The precision of the load cell for measuring the applied load is 1 N. For high-temperature tests, the specimens were heated to 800 ℃ with a rate of 5 ℃/min and held for 15 min to reach thermal equilibrium before applying mechanical loads. The mechanical tests were conducted by means of displacement control with a loading rate of 0.5 mm/min. For each case, about 3-5 specimens were repeatedly tested and the average strength was determined. Photograph of the experimental setup for mechanical test is given in Fig. 8.

2.2.2. Creep test

Tensile and shear creep tests were conducted at 800 ℃ under a constant load using a direct-load creep test machine, as shown in Fig. 9. Based on the results of mechanical results, various weights were selected as the loading source for applying constant loads to generate the creep rupture time distributed in the orders of 1, 10, 100, and 1000 h. The smallest size of the weight applied in the creep test is 1 N. For the high-temperature creep tests, the specimens were heated to 800 ℃ with a rate of 5 ℃/min and held for 15 min to reach thermal equilibrium before applying force.

2.3. Microstructural Analysis

After creep testing, fracture surface of each specimen was examined with an optical microscope to determine the true joining area. In order to investigate the characteristics of interfaces in the joint, some samples were cut along the longitudinal direction to observe the cross sections. The cross sections were finely polished to optical finish. SEM was also used to examine the interfacial morphology between the glass-ceramic sealant and metallic interconnect. EDS module was used for composition analysis in order to understand the elemental distribution around the joining area. The creep fracture modes of the joint under tensile stress and shear stress were then characterized.

3. RESULTS AND DISCUSSION

As mentioned above, glass-ceramic sealant may have chemical reactions in itself and with metallic interconnect and protective coating during long-term operation of SOFC, which significantly affects the properties of their joint. In addition, thermal stresses of shear and tensile modes generated by CTE mismatch may damage the joint leading to failure of sealant. Since Cr poisoning is unavoidable by using bare metallic interconnect of high Cr content, effect of protective coating on the joint strength between glass-ceramic sealant and metallic interconnect becomes a critical issue in mechanical integrity of pSOFC stack. Formation of adhesive oxide layers is the main mechanism of interfacial joining between glass-ceramic sealant and metallic interconnect. The bonding strength of the joint originates from the mutual van der Waals force of the formed oxide layers. The high-temperature joining mechanism of the GC-9 glass-ceramic and bare Crofer 22 H alloy involves formation of two oxide layers with a Cr_2O_3 layer on the surface of Crofer 22 H and a $BaCrO_4$ layer on the surface of GC-9 [56]. A spinel ($(Cr,Mn)_3O_4$) layer is formed between these two oxide layers. Since the LSM film is coated on the surface of Crofer 22 H, interfacial reactions between LSM film, Crofer 22 H, and GC-9 are characterized in this study. In addition, influence of these reactions on the creep properties of the joint between GC-9 and LSM-coated Crofer 22 H is investigated.

3.1. Non-aged Joint of Glass-Ceramic Sealant and LSM-Coated Metallic Interconnect

3.1.1. Joint strength

Typical force-displacement curves for the non-aged shear specimens tested at RT and 800 ℃ in air are shown in Fig. 10. The force-displacement curve at RT exhibits a typical pattern of brittle fracture with fracture taking place at the linear portion. Note that the initial non-linear behavior in each force-displacement curve is due to some compliance of the pin-loading rigs. In addition, the force-displacement curve at 800 ℃ exhibits a non-linear failure mode. As the testing temperature of 800 ℃ is higher than the softening temperature (745 ℃) of the GC-9, the failure behavior at 800 ℃ changes from a brittle mode to a ductile one.

Shear strength of the non-aged specimens tested in air at RT and 800 ℃ are

shown in Fig. 11. In Fig. 11 and the following similar figures, the height of a column indicates the average strength and the attached error bar represents the standard deviation for each given condition. For shear loading mode, the average strength is of 1.45 ± 0.41 MPa at RT and 0.38 ± 0.07 MPa at 800 ℃. The joint strength under shear loading is significantly reduced by 74% when the testing temperature is increased from RT to 800 ℃. Figure 12 shows the failure patterns of non-aged shear specimens tested at RT and 800 ℃. As shown in Fig. 12(a) and 12(b), the upper steel slice is still adhered with the GC-9 glass-ceramic layer and the lower one is separated from the glass-ceramic layer after testing. In the upper part of Fig. 12(a) and 12(b), the white region and spots are identified to be GC-9. On the other hand, the dark red region is an area mixed with GC-9 and LSM film. Optical and SEM micrographs of two outlined regions of the fracture surface in the upper and lower micrographs of Fig. 12(b) are shown in Fig. 13. Needle-shape crystalline phase which is observed in Fig. 13(b) is identified as α-$Ba(Al_2Si_2O_8)$. In addition, the fracture surface exhibits a characteristic of dimple shape, indicating the fracture mode is ductile failure and concurs with the force-displacement curve shown in Fig. 10. By means of EDS analysis, La, Si, Ba, Al, Sr, Ca, and O elements are all detected in Fig. 13(b) and 13(c), indicating it is a region in which the GC-9 glass-ceramic layer might react with LSM. EDS results of Fig. 13(b) and 13(c) are shown in Fig. 14. Note that Pt is also detected (Fig. 14) as a thin Pt layer is coated on the specimen for SEM observation. In order to characterize the interaction between GC-9 and LSM, XRD is applied to further check the phase structures in the specimen of Fig. 12(b), as shown in Fig. 15. In addition to the phase of α-$Ba(Al_2Si_2O_8)$, the diffraction peaks present in Fig. 15 also match with those of $Ca_2La_8(SiO_4)_6O_2$ and La_2O_3, indicating that GC-9 indeed reacts with LSM film and forms a rare-earth oxyapatite layer. Accordingly, for non-aged shear specimens tested at RT and 800 ℃, fracture occurs mostly at the oxyapatite interlayer between LSM and GC-9 and occasionally within the GC-9 layer.

Typical force-displacement curves for the non-aged tensile specimens tested at RT and 800 ℃ in air are shown in Fig. 16. The force-displacement curves at RT and 800 ℃ in air both exhibit a typical linear brittle fracture pattern (Fig. 16). Figure 17 shows the tensile strength of the non-aged joint specimens tested at RT and 800 ℃. For tensile loading mode, the average strength is of 9.37 ± 1.7 MPa at RT and 3.58 ± 0.25 MPa at 800 ℃. The joint strength under tensile loading is significantly reduced by 62% when the testing temperature is increased from RT to 800 ℃.

Figure 18 shows the failure patterns of non-aged tensile specimens tested at

RT and 800 ℃. Similar to those under shear loading, the white region is GC-9 and the dark red region is an area mixed with GC-9 and LSM film. Optical and SEM micrographs of two outlined regions of the fracture surface in the upper and lower micrographs of Fig. 18(b) are shown in Fig. 19(a). Similar to the shear specimens, needle-shape crystalline phase α-$Ba(Al_2Si_2O_8)$ is observed in the fracture surface, as shown in Fig. 19(b). The corresponding EDS analysis results (Fig. 20(a)) show a similar pattern to that in Fig. 13(b) and 13(c), indicating it is a region in which GC-9 reacts with LSM and can be referred to as $Ca_2La_8(SiO_4)_6O_2$. In addition, a small and dense crystalline phase is observed underneath the mixed LSM/GC-9 layer, as shown in Fig. 19(c) and 19(d). This crystalline phase is identified as $(Cr,Mn)_3O_4$ spinel based on the EDS result shown in Fig. 20(b). It indicates that some Cr is trapped by LSM and reacts with Mn to form a spinel structure. As a result, the outward diffusion of Cr from the metallic interconnect to ambient environment is inhibited. Accordingly, fracture occurs mostly at the oxyapatite interlayer between LSM and GC-9 and occasionally within the GC-9 layer for non-aged tensile specimens tested at RT and 800 ℃.

In order to investigate the characteristics of interactions at the interface between GC-9 and LSM, some non-aged tensile specimens were cut along the longitudinal direction before and after the joining process to observe the cross section. Cross-sectional view of a tensile specimen before the joining process is shown in the SEM micrograph of Fig. 21. As shown in Fig. 21, a distinct dense LSM coating layer with a thickness of 3 μm is observed. EDS analysis and elemental mapping results (Figs. 22 and 23) further confirm that it is indeed an LSM coating film. Figure 24 shows the cross-sectional view of the tensile specimen after joining with GC-9. Note that the LSM film cannot be clearly identified in Fig. 24 as that observed in Fig. 21. Instead, an interlayer with a thickness of about 10 μm is observed between GC-9 and Crofer 22 H, as shown in Fig. 24. According to XRD result (Fig. 15) and SEM observation (Fig. 21), it can be concluded that the LSM coating reacts with GC-9 to form the rare-earth oxyapatite layer during the joining process. In addition, some defects are observed within this layer, which may serve as a stress concentrator and become the weakest position in the joint. Since the shrinkage during crystallization of LSM in the sintering process may cause formation of these defects [25], crystallization of the oxyapatite layer might further lead to formation of microcracks. On the other hand, CTE of oxyapatite ceramics (less than 7×10^{-6} $℃^{-1}$) is significantly lower than that of other crystalline phases and Crofer 22 H, resulting in formation of defects or cracks because of thermal mismatch at

high-temperature operation [57].

Comparison of shear and tensile joint strength for the non-coated and LSM-coated joint specimens tested in air are shown in Figs. 25 and 26, respectively. Note that the data of non-coated specimens are taken from Ref. [56]. The average shear strength of non-coated joint specimens is of 6.6 ± 1.6 MPa at RT and 4.7 ± 0.3 at 800 ℃, while the average tensile strength is of 23.0 ± 3.3 MPa at RT and 12.7 ± 3.3 MPa at 800 ℃. As shown in Figs. 25 and 26, for both loading modes, the average strength of the non-aged joint is significantly degraded when the specimens is coated with an LSM film. With the LSM coating, the shear strength of the joint is reduced by 78% and 92% at RT and 800 ℃, respectively. On the other hand, the tensile strength of the joint is reduced by 59% and 72% at RT and 800 ℃, respectively. It indicates that while using the LSM protective coating to prevent Cr poisoning, however, the bonding strength of the joint is significantly decreased due to the formation of defects in the oxyaptite layer. In addition, since fracture mostly occurs at the interlayer between LSM and GC-9 for coated specimens, it can be concluded that this interlayer is the weakest position of the joint.

3.1.2. Creep rupture behavior

Creep rupture behavior of the non-aged joint of GC-9 glass-ceramic sealant and LSM-coated metallic interconnect under constant shear and tensile loads at 800 ℃ in air are shown in Fig. 27 by plotting applied stress versus creep rupture time. As shown in Fig. 27, the relationship between the applied stress and creep rupture time can be well described by a simple power law for each loading mode. The fitted equation and correlation coefficient (r) for each loading mode in Fig. 27 are expressed as follows,

shear loading: $\tau {t_r}^{0.020} = 0.18, \quad r^2 = 0.68$ (4)

tensile loading: $\sigma {t_r}^{0.345} = 1.26, \quad r^2 = 0.83$ (5)

where τ and σ, respectively, are the applied shear and tensile stresses in unit of MPa and t_r is time to rupture in unit of h. Note that the runout points are not included in determining the fitted equations as they are not ruptured in the test. The creep rupture time for the joint specimen subjected to a constant shear or tensile load at 800 ℃ in air can be estimated through these power-law relations thanks to the high correlation coefficient values. As shown in Fig. 27, the creep

rupture time increases with a decrease in applied stress for both loading modes. With an applied constant stress greater than 0.17 MPa and 0.57 MPa, respectively, for shear and tensile loading modes, the creep rupture time is less than 10 h according to Eqs. (4) and (5). On the other hand, for a creep rupture time longer than 1000 h, the applied constant stress should be smaller than 0.16 MPa and 0.12 MPa for shear and tensile loading modes, respectively. Accordingly, the shear creep strength of non-aged joint at 1000 h in air is about 42% of the average shear strength (0.38 MPa), while the tensile creep strength at 1000 h is only about 3% of the average tensile strength (3.58 MPa). Apparently, the given joint is more sensitive to creep damages under tensile loading than shear loading.

3.1.3. Failure analysis

In the present study, the creep rupture time is divided into three intervals, namely short creep rupture time (t_r < 100 h), medium-term creep rupture time (100 h < t_r < 1000 h), and long-term creep rupture time (t_r > 1000 h). Figure 28 shows the failure patterns in the non-aged shear specimens test at 800 ℃. As shown in Fig. 28(a), for a short creep rupture time (t_r < 100 h), fracture mostly occurs at the oxyapatite layer and occasionally in the GC-9 layer. Evidences of microstructural observation for selected regions in the fracture surfaces of Fig. 28(a) are provided as follows. Optical and SEM micrographs of two outlined regions of the fracture surface in Fig. 28(a) are shown in Fig. 29. Relevant EDS results of Fig. 29(b) and 29(c) are shown in Fig. 30. Fig. 29(b) and Fig. 29(c) show a microstructure of the oxyapatite ceramic. In addition, some needle-shape crystalline phases, α-Ba($Al_2Si_2O_8$), are observed in Fig. 29(b). Since Ca, Ba, Al, Si, La, Sr and O are detected in Fig. 30(a) and 30(b), the microstructure presented in Fig. 29(b) and 29(c) indeed is the $Ca_2La_8(SiO_4)_6O_2$ oxyapatite ceramic. The failure patterns and microstructural analysis results of shear specimens with a short creep rupture time (Fig. 28(a)) show similar features to those of shear strength testing specimens (Fig. 12(b)).

As shown in Fig. 28(b), for a medium-term creep rupture time (100 h < t_r < 1000 h), failure pattern shows that the oxyapatite ceramic is partially covered with a yellow and brown layer. Fig. 31 shows the optical and SEM micrographs of two outlined regions of the fracture surface in the lower part of Fig. 28(b). Relevant EDS results of Fig. 31(b) and 31(c) are shown in Fig. 32. It is noticed that large crystalline phases are observed in Fig. 31(b) and Fig. 31(c). By means of EDS analysis, Ba, Cr and O are detected in these large crystalline phases

indicating they are $BaCrO_4$ chromate. It reveals that for a medium-term creep rupture time over 100 h, Cr diffuses from Crofer 22 H to GC-9 and reacts with Ba to form a $BaCrO_4$ layer. In addition, the CTE of $BaCrO_4$ is relatively large compared to oxyapatite ceramic such that fracture occurs at the interface of $BaCrO_4$/oxyapatite.

As shown in Fig. 28(c), for a long-term creep rupture time (t_r > 1000 h), failure pattern shows that almost half of the fracture surface is covered with a yellow $BaCrO_4$ layer. Note that this specimen is actually a runout specimen but it was broken during the cooling process after the test was terminated. Fig. 33 shows the optical and SEM micrographs of an outlined region of the fracture surface in the upper part of Fig. 28(c). The crystalline phase shown in Fig. 33(b) is $BaCrO_4$, but oxyapatite ceramic could not be identified in this region. Compared to Fig. 28(b), it indicates that the amount of $BaCrO_4$ increases with time staying at high temperature. Accordingly, for a long-term creep rupture time, fracture occurs at the interface of $BaCrO_4$/oxyapatite and inside the $BaCrO_4$ layer.

Figure 34 shows the failure patterns in the tensile specimens tested at 800 ℃. As shown in Fig. 34(a), for a short creep rupture time (t_r < 100 h), fracture mostly occurs at the oxyapatite layer and occasionally in the GC-9 layer. Optical and SEM micrographs of two outlined regions of the fracture surface in Fig. 34(a) are shown in Fig. 35. Fig. 35(b) and Fig. 35(c) show a microstructure of the oxyapatite ceramic mixed with α-$Ba(Al_2Si_2O_8)$. In addition, dense and small $(Cr,Mn)_3O_4$ spinel phases are observed at some defects in Fig. 35(c) as a result of the reaction between Cr and Mn. The failure patterns and microstructural analysis results of tensile specimens with a short creep rupture time (Fig. 34(a)) show similar features to those of tensile strength testing specimen (Fig. 18(b)).

As shown in Fig. 34(b), for a medium-term creep rupture time (100 h < t_r < 1000 h), failure pattern shows that the fracture surface is mixed with oxyapatite and $BaCrO_4$. Fig. 36 shows the optical and SEM micrographs of two outlined regions of the fracture surface in the lower part of Fig. 34(b). Same as the shear specimen with a medium-term creep rupture time, large $BaCrO_4$ phases are observed in Fig. 36(b) and 36(c), indicating that Cr diffuses outward from Crofer 22 H to GC-9 and reacts with Ba. Therefore, the fracture site changes from oxyapatite to $BaCrO_4$ layer with an increase of creep rupture time to exceed 100 h.

A non-ruptured, runout tensile specimen with a creep rupture time over 1000 h is cut along a direction paralleled to the applied loading for observing the interface between glass-ceramic sealant, LSM coating, and metallic interconnect

in a cross-sectional view, as shown in Fig. 37. In Fig. 37(a) and 37(b), large cracks through the interface of GC-9 and Corfer 22 H are observed. It indicates that cracks developed at the interface after 1000 h of creep loading, although the specimen did not rupture. High-magnification views shown in Fig. 37(c) and 37(d) reveal that cracking mainly takes place in the $BaCrO_4$ layer. In addition, a continuous Cr_2O_3 layer about 1 μm in thickness and discontinuous $(Cr,Mn)_3O_4$ spinel layers are observed between $BaCrO_4$ and Crofer 22 H. It is concluded that some Cr is initially trapped by the LSM film and becomes Cr_2O_3 and $(Cr,Mn)_3O_4$. However, the outward diffusion of Cr may not be fully inhibited resulting in the formation of $BaCrO_4$ and cracks inside this $BaCrO_4$ layer after a long-term operation at high temperature.

3.2. Aged Joint of Glass-Ceramic Sealant and LSM-Coated Metallic Interconnect

3.2.1. Joint strength

Typical force-displacement curves for the 1000 h-aged shear specimens tested at RT and 800 ℃ in air are shown in Fig. 38. Similar to the non-aged shear specimens, the force-displacement curve exhibits a typical pattern of brittle fracture with fracture taking place at the linear portion at RT and a non-linear failure mode at 800 ℃. Figure 39 shows the shear strength of the 1000 h-aged joint specimens tested at RT and 800 ℃. For shear loading mode, the average strength is of 4.47 ± 0.38 MPa at RT and 1.98 ± 0.11 MPa at 800 ℃. The joint strength under shear loading is significantly reduced by 56% when the testing temperature is increased from RT to 800 ℃.

Figure 40 shows the failure patterns of 1000 h-aged shear specimens tested at RT and 800 ℃. As shown in Fig. 40(a) and 40(b), a yellow $BaCrO_4$ layer is identified on the fracture surface of specimens tested at RT and 800 ℃, indicating that Cr diffuses from Crofer 22 H to GC-9 and reacts with Ba to form a $BaCrO_4$ layer during the thermal aging treatment. Optical and SEM micrographs of three outlined regions of the fracture surface in the upper micrograph of Fig. 40(b) are shown in Fig. 41. Fig. 41(b) and Fig. 41(c) show a microstructure of mixed GC-9 and $BaCrO_4$ crystalline phases. Note that some $BaCrO_4$ crystalline phases are embedded in an oxyapatite layer (Fig. 41(c)). Relevant EDS results of Fig. 41(b) shown in Fig. 42 further confirm that the flaky crystalline phase is GC-9. In addition, mixed oxyapatite and GC-9 are identified in Fig. 41(d). Compared to the non-aged shear specimens tested at 800

℃ (Fig. 12(b)), it seems that the LSM film fully reacts with GC-9 to form the mixed GC-9/oxyapatite layer after 1000-h thermal aging. Accordingly, fracture mostly occurs at the mixed GC-9/$BaCrO_4$ layer and occasionally penetrates through the GC-9/oxyapatite layer for 1000 h-aged shear specimens tested at RT and 800 ℃.

Typical force-displacement curves for the 1000 h-aged tensile specimens tested at RT and 800 ℃ in air are shown in Fig. 43. Similar to the non-aged tensile specimens, the force-displacement curves at RT and 800 ℃ in air both exhibit a typical linear brittle fracture pattern (Fig. 43). Figure 44 shows the tensile strength of the 1000 h-aged joint specimens tested at RT and 800 ℃. For tensile loading mode, the average strength is of 19.91 ± 2.39 MPa at RT and 2.41 ± 0.29 MPa at 800 ℃. The joint strength under tensile loading is significantly reduced by 88% when the testing temperature is increased from RT to 800 ℃.

Figure 45 shows the failure patterns of 1000 h-aged tensile specimens tested at RT and 800 ℃. As shown in Fig. 45(a), fracture occurs with a cracking path going through the GC-9/oxyapatite/$BaCrO_4$ layer for specimen tested at RT. On the other hand, fracture occurs in the mixed GC-9/oxyapatite layer for specimen tested at 800 ℃. Note that $BaCrO_4$ is not observed at the fracture surface for specimen tested at 800 ℃. Optical and SEM micrographs of two outlined regions of the fracture surface in the upper and lower micrographs of Fig. 45(b) are shown in Fig. 46. In Fig. 46(b), mixed GC-9/oxyapatite and peeled $(Cr,Mn)_3O_4$ are observed at the fracture surface. In addition, dense $(Cr,Mn)_3O_4$ layer and peeled GC-9/oxyapatite are identified in the opposite side of fracture surface, as shown in Fig. 46(c). It reveals that the fracture site changes from the interface between GC-9/oxyapatite and $BaCrO_4$ to the interface between GC-9/oxyapatite and $(Cr,Mn)_3O_4$ when the testing temperature increases from RT to 800 ℃.

In order to characterize the effect of thermal aging on joint and interaction between LSM/Crofer 22 H/GC-9, some 1000 h-aged tensile specimens were cut along the longitudinal direction to observe the cross sections. Cross-sectional views of a tensile specimen after 1000 h thermal aging are shown in the SEM micrographs of Fig. 47. As shown in Fig. 47(a), many defects are observed at the interface between $BaCrO_4$ and mixed GC-9/oxyapatite layer. In addition, a clear continuous spinel layer is identified between Crofer 22 H and $BaCrO_4$ layer, as shown in Fig. 47(b). The defects between $BaCrO_4$ and mixed GC-9/oxyapatite layer apparently are the weakest positions in the joint and the fracture takes place here for tensile specimens tested at RT. However, for tensile specimens

tested at 800 ℃, fracture site changes from the interface between GC-9/oxyapatite and $BaCrO_4$ to the interface between GC-9/oxyapatite and $(Cr,Mn)_3O_4$. The reason for this change is unknown at this moment. Compared to the failure pattern of 1000 h-aged shear specimen tested at 800 ℃ (Fig. 40(b)), it reveals that the 1000 h-aged specimens is more sensitive to tensile loading than shear loading and the interface between GC-9/oxyapatite and $(Cr,Mn)_3O_4$ might become the weakest position when subjected to tensile loading at high temperature.

Comparison of shear and tensile joint strength for the non-aged and 1000 h-aged joint specimens tested in air are shown in Figs. 48 and 49, respectively. As shown in Fig. 48, for shear loading mode, the average strength of the 1000 h-aged joint is significantly enhanced compared to non-aged joint tested at RT and 800 ℃. However, for tensile loading mode, the average strength of the 1000 h-aged joint is increased at RT but decreased at 800 ℃. Accordingly, a thermal aging treatment at 800 ℃ in air for 1000 h enhances the joint strength of shear loading at RT and 800 ℃ by 208% and 421%, respectively. A thermal aging treatment at 800 ℃ in air for 1000 h enhances the joint strength of tensile loading at RT by 112% and degrades it at 800 ℃ by 32%. A tendency of increasing joint strength at RT after thermal aging in air may be related to the relaxation of residual stresses, a greater extent of crystallization in glass-ceramic, and a self-healing effect of glass-ceramic during aging treatment. In addition, the joint strength of 1000 h-aged tensile specimen at 800 ℃ is slightly lower than that of non-aged tensile specimen may be due to that the oxide scales are more sensitive to tensile loading.

3.2.2. Creep rupture behavior

Creep rupture behavior of the 1000 h-aged joint of GC-9 glass-ceramic sealant and LSM-coated metallic interconnect under constant shear and tensile loads at 800 ℃ in air are shown in Fig. 50 by plotting applied stress versus creep rupture time. As shown in Fig. 50, the relationship between the applied stress and creep rupture time can be well described by a simple power law for each loading mode. The fitted equation and correlation coefficient (r) for each loading mode in Fig. 50 are expressed as follows,

shear loading: $\tau {t_r}^{0.151} = 0.52, \quad r^2 = 0.80$ (6)

tensile loading: $\sigma {t_r}^{0.034} = 0.48, \quad r^2 = 0.75$ (7)

As shown in Fig. 50, the creep rupture time increases with a decrease in applied stress for both loading modes. With an applied constant stress greater than 0.37 MPa and 0.44 MPa, respectively, for shear and tensile loading modes, the creep rupture time is less than 10 h according to Eqs. (6) and (7). On the other hand, for a creep rupture time longer than 1000 h, the applied constant stress should be smaller than 0.18 MPa and 0.38 MPa for shear and tensile loading modes, respectively. Accordingly, the shear creep strength of 1000 h-aged joint at 1000 h in air is about 9% of the average shear strength (1.98 MPa), while the tensile creep strength at 1000 h is about 16% of the average tensile strength (2.41 MPa).

3.2.3. Failure analysis

Figure 51 shows the creep failure patterns in the 1000 h-aged shear specimens test at 800 ℃. As shown in Fig. 51(a), for a short creep rupture time (t_r < 100 h), a yellow $BaCrO_4$ layer is identified on the fracture surface and fracture mostly occurs at the mixed GC-9/$BaCrO_4$ layer and occasionally penetrates through the GC-9/oxyapatite layer. The failure pattern of 1000 h-aged shear specimens with a short creep rupture time (Fig. 51(a)) shows similar features to those of 1000 h-aged shear strength testing specimens (Fig. 40(b)). It reveals that for a short creep rupture time, the failure mechanism is similar to that in the mechanical strength test due to a short loading time.

As shown in Fig. 51(b), for a medium-term creep rupture time (100 h < t_r < 1000 h), the failure pattern shows that almost three quarters of the fracture surface are covered with a yellow $BaCrO_4$ layer. Optical and SEM micrographs of three outlined regions of the fracture surface in the upper and lower micrographs of Fig. 51(b) are shown in Fig. 52. Fig. 52(b) shows a microstructure composed of dense $BaCrO_4$ crystalline phases mixed with oxyapatite ceramic. In addition, a few microcracks are observed on the $BaCrO_4$ layer. As shown in Fig. 52(c), mixed oxyapatite and GC-9 are identified on the fracture surface. The micrograph in Fig. 52(d) shows a microstructure of some $BaCrO_4$ phases embedded in the oxyapatite ceramic. It is noticed that $BaCrO_4$ phases (Fig. 52(d)) become more dense compared to the non-aged shear specimens with a medium-term creep rupture time (Fig. 31(b) and 31(c)). It indicates that crystallization of $BaCrO_4$ is promoted by thermal aging and the thickness of $BaCrO_4$ layer increases after aging treatment. In addition, as mentioned above, the CTE of $BaCrO_4$ is relatively large compared to oxyapatite ceramic such that cracking occurs at the interface of $BaCrO_4$/oxyapatite.

Figure 53 shows the creep failure patterns in the 1000 h-aged tensile specimens tested at 800 ℃. As shown in Fig. 53(a), for a short creep rupture time (t_r < 100 h), fracture surface shows similar features to those of 1000 h-aged tensile strength testing specimens (Fig. 45(b)). Same as the 1000 h-aged shear creep specimens with a short creep rupture time, the failure mechanism is similar to that in the mechanical strength test due to a short loading time.

As shown in Fig. 53(b), for a medium-term creep rupture time (100 h < t_r < 1000 h), the failure pattern looks similar to that in the 1000 h-aged tensile specimens with a short creep rupture time. Note that in contrast to the 1000 h-aged shear specimens with a medium creep rupture time, only a small yellow $BaCrO_4$ region can be identified by optical microscopic observation. Optical and SEM micrographs of four outlined regions of the fracture surface in the upper and lower micrographs of Fig. 53(b) are shown in Fig. 54. GC-9, oxyapatite, and $BaCrO_4$ are all identified in Fig. 54(b) and 54(c), indicating that cracking penetrates through the mixed GC-9/oxyapatite and $BaCrO_4$ layer. On the opposite fracture surface shown in Fig. 54(d), $BaCrO_4$ phases are embedded in that oxyapatite layer and some $(Cr,Mn)_3O_4$ phases are further found in Fig. 54(e). The $(Cr,Mn)_3O_4$ spinel phases are also observed on the fracture surface of 1000 h-aged tensile strength test specimens (Fig. 46(b) and 46(c)). It reveals that in contrast to the 1000 h-aged shear specimens, $BaCrO_4$ might not be the only phase to dominate the failure mechanism in the 1000 h-aged tensile specimens. Increase in crystallization of $(Cr,Mn)_3O_4$ after thermal aging makes it become a dense and continuous layer (Fig. 47(b)), which might also affect the failure mechanism when subjected to tensile loading.

3.3. Effect of LSM Coating on Joint Strength and Creep Rupture Behavior

In order to avoid Cr diffusion from metallic interconnect to poison the cathode and to ensure the service life of planar SOFC over 40,000 h, it is important to understand the effect of protective LSM coating on the mechanical properties of the joint. For joint strength at RT and 800 ℃, both shear and tensile strengths of non-aged, LSM-coated joint specimens are significantly decreased compared to the non-coated counterparts (Figs. 25 and 26). The failure patterns of both non-aged, LSM-coated shear and tensile specimens tested at 800 ℃ (Figs. 12(b) and 18(b)) show that fracture mostly occurs at the oxyapatite interlayer between Crofer 22 H and GC-9. On the other hand, fracture mostly occurs at the interface of Cr_2O_3/GC-9 and takes place in GC-9 for the non-aged, non-coated shear and tensile specimens tested at RT and 800 ℃ (Figs.

55 and 56) [56], respectively. Cross-sectional views of the as-joined tensile specimen before and after joining process (Figs. 21 and 24) reveal that the entire LSM film almost reacts with GC-9 to form a rare-earth oxyapatite layer during joining process. In addition, some defects are observed within this layer resulting in the failure of the joint. Note that Cr_2O_3 layer is not identified in the cross-sectional views of as jointed LSM-coated specimens (Fig. 24) and dense $(Cr,Mn)_3O_4$ spinel phases are observed on the surface of interconnect (Fig. 19(d)). It indicates that some Cr is trapped by LSM and reacts with Mn to form a spinel structure, compared to the non-coated specimens.

For non-aged shear and tensile specimens, the creep strength at 1000 h for the LSM-coated specimen is about 15% and 11% of the non-coated counterparts (1.1 MPa) [33], respectively, as shown in Fig. 57. The fracture takes place between $BaCrO_4$ and GC-9 layer for non-coated shear and tensile specimens no matter whether they have a short or medium-term creep rupture time (Figs. 58 and 59) [33]. For both non-aged, LSM-coated shear and tensile specimens with a short creep rupture time (Figs. 28(a) and 34(a)), the failure patterns show similar features to those of shear and tensile strength testing specimens (Figs. 12(b) and 18(b)), respectively, indicating the failure mechanism of specimens with a short creep rupture time is similar to that of strength testing specimens. For both non-aged, LSM-coated shear and tensile specimens with a medium-term creep rupture time, the fracture site changes from oxyapatite interlayer to mixed oxyapatite/$BaCrO_4$ layer with an increase of creep rupture time to exceed 100 h (Figs. 31 and 36). In addition, large cracks are observed in the $BaCrO_4$ layer and a continuous Cr_2O_3 layer is identified between $BaCrO_4$ and Crofer 22 H in a non-ruptured, runout tensile specimen with a creep testing time over 1000 h (Fig. 37). It reveals that some Cr is initially trapped by the LSM film and becomes Cr_2O_3 and $(Cr,Mn)_3O_4$ for the LSM-coated specimens. However, since the LSM film almost fully reacts with GC-9 and disappears, the outward diffusion of Cr could not be completely inhibited resulting in the formation of $BaCrO_4$ and cracking inside this layer after a long-term operation at high temperature.

3.4. Effects of Thermal Aging on LSM-Coated Joint

As the service life of planar SOFCs is expected for 40,000 h or more, it is important to investigate the effect of thermal aging on the joint during long-term operation at high temperature. In mechanical strength test of 1000 h-aged joint specimens at RT, joint strength of both shear and tensile specimens is significantly enhanced by thermal aging treatment compared to the non-aged

specimens. However, in mechanical strength test of 1000 h-aged joint specimens at 800 ℃, shear strength is increased but the tensile strength is slightly decreased in comparison with the non-aged specimens. The failure patterns of 1000 h-aged shear specimens (Figs. 40 and 41) show that fracture mostly occurs at mixed GC-9/$BaCrO_4$ layer and occasionally penetrates through the GC-9/oxyapatite layer. For 1000 h-aged tensile specimens, facture site changes from the interface between GC-9/oxyapatite and $BaCrO_4$ to the interface between GC-9/oxyapatite and $(Cr,Mn)_3O_4$ when the testing temperature increases from RT to 800 ℃. A continuous $(Cr,Mn)_3O_4$ spinel layer is formed between Crofer 22 H and $BaCrO_4$ layer after 1000-h thermal aging. Apparently, thermal aging promotes the crystallization of glass-ceramic sealant and oxide scales such as chromia, barium chromate, and spinel phase. A greater extent of crystallization in glass-ceramic makes the joint strength is enhanced after a thermal aging treatment. However, increased crystallization of oxide scales causes them to become thicker and weaker and might dominate the failure mechanism. Overall, it seems that the 1000 h-aged specimens are more sensitive to tensile loading than shear loading and the interface between GC-9/oxyapatite and $(Cr,Mn)_3O_4$ is the weakest path when subjected to tensile loading at high temperature.

After 1000-h thermal aging, the shear and tensile creep strength at 1000 h of the thermally aged joint is enhanced by 13% and 216%, respectively, compared to those without thermal aging, as shown in Fig. 60. Note that the creep strength at 1000 h of 1000 h-aged tensile specimen is significantly increased but the joint strength is reduced at 800 ℃. The true mechanism is still unknown at this moment. However, since the $(Cr,Mn)_3O_4$ phases are observed on the fracture surface of 1000 h-aged tensile strength and creep test specimens, it indicates that these crystalline phases might have a better ability to sustain the creep damage rather than a fast fracture at 800 ℃. For 1000 h-aged shear and tensile specimens with a short creep rupture time, the fracture surfaces show similar patterns to those of 1000 h-aged shear and tensile strength testing specimens, respectively. Oxyapatite and $BaCrO_4$ dominate the failure mechanism for 1000 h-aged shear specimens regardless of the length of creep rupture time. On the other hand, $(Cr,Mn)_3O_4$ spinel layer might have more influence on creep behavior when the specimens are subjected to tensile loading after thermal aging.

3.5. Overall Comparison of Fracture Site

In previous sections, effects of LSM coating and thermal aging on the joint strength and creep properties between the given GC-9 glass-ceramic sealant and Crofer 22 H steel have been investigated. An overall comparison of fracture modes for all the given specimens and testing conditions is made and discussed in this section. Table 6 lists the joint strength and creep strength at 1000 h for all the mechanical test specimens. On the other hand, Table 7 and Table 8 list the fracture site for all the strength test and creep test specimens, respectively. Fracture modes are characterized in 6 types according to the observation described above. Fracture occurring in the oxyapatite, GC-9, and $BaCrO_4$ layer is designated as "A," "B," and "C," respectively. Fracture occurring at the interface between the mixed GC-9/oxyapatite and $BaCrO_4$ layer is designated as "D." Fracture site in the mixed oxyapatite/$BaCrO_4$ layer is designated as "E," and the fracture occurring at the interface between mixed GC-9/oxyapatite and $(Cr,Mn)_3O_4$ layer is designated as "F." If the fracture involves multisite, these fracture sites are marked together.

As listed in Table 6, for both non-aged and 1000 h-aged specimens, shear and tensile joint strengths are reduced as the testing temperature increases from RT to 800 ℃. In addition, a thermal aging treatment generally enhances the joint strength and creep strength at 1000 h except for the joint strength of 1000 h-aged tensile specimens at 800 ℃ (Table 6). An increase of crystallization in GC-9 glass-ceramic sealant makes the joint strength and creep strength enhanced after a thermal aging treatment. However, the oxide scale growth, such as spinel and chromate, is also promoted by thermal aging and might dominate the failure mechanism. Schematic diagrams of the microstructure at interfaces for non-aged and 1000 h-aged specimens with different conditions are shown in Fig. 61, based on the microstructural analysis results mentioned above. In addition, the fracture sites listed in Table 7 and Table 8 are also labelled in Fig. 61. As shown in Fig. 61(a), a dense LSM film is coated on the surface of Crofer 22 H followed by spreading with GC-9 glass-ceramic. As shown in Fig. 61(b), LSM film reacts with GC-9 to form an oxyapatite layer after joining process and the defects are generated due to volume shrinkage in crystallization or thermal mismatch at high temperature. With a medium-term creep rupture time, Cr diffuses from Crofer 22 H to GC-9 and forms a $BaCrO_4$ layer (Fig. 61(c)). In addition, a continuous Cr_2O_3 layer is formed again between Crofer 22 H and spinel layer. Microcracks are generated within the $BaCrO_4$ layer due to the thermal mismatch at high temperature and dominate the failure mechanism. A thermal aging

treatment for 1000 h promotes the crystallization of GC-9 and all oxide scales leading to a more dense oxide layer such as $BaCrO_4$, spinel, and oxyapatite (Fig. 61(d)). It is noted that after a thermal aging treatment, different oxide scales are more easily mixed together at the interface or even form a mixed oxide layer, as described in previous sections. As a result, the fracture site of 1000 h-aged specimens tends to occur at the mixed oxide layer or penetrates through these oxide layers. In addition, It seems that a thicker $(Cr,Mn)_3O_4$ spinel layer might have more influence on the joint strength and creep behavior when the specimens are subjected to tensile loading after thermal aging.

4. CONCLUSIONS

(1) An LSM coating on the metallic interconnect degrades the joint strength between the given GC-9 glass-ceramic sealant and Crofer 22 H steel. With the LSM coating, the shear strength of the non-aged joint specimen is reduced by 78% and 92% at RT and 800 ℃, respectively. On the other hand, the tensile strength of the joint is reduced by 59% and 72% at RT and 800 ℃, respectively.

(2) For the creep test of non-aged joint specimens at 800 ℃ in air, the creep rupture time is less than 10 h when the applied stress is greater than 0.17 MPa and 0.57 MPa in shear and tensile loading modes, respectively. For a creep rupture time longer than 1000 h, the applied constant stress should be smaller than 0.16 MPa and 0.12 MPa for shear and tensile loading modes, respectively. Accordingly, the shear creep strength of non-aged joint at 1000 h in air is about 42% of the average shear strength, while the tensile creep strength at 1000 h is only about 3% of the average tensile strength.

(3) An LSM coating on the metallic interconnect also degrades the creep strength of such a joint at 800 ℃. Compared to the non-aged, non-coated specimens, the creep strength at 1000 h for the LSM-coated shear and tensile specimens is significantly reduced by 85% and 89%, respectively.

(4) A thermal aging treatment at 800 ℃ for 1000 h significantly enhances the joint strength of both shear and tensile specimens at RT. For high-temperature mechanical strength at 800 ℃, the thermal aging also enhances the joint strength of shear specimen but slightly degrades it for tensile specimen.

(5) For the creep test of 1000 h-aged joint specimens at 800 ℃ in air, the creep rupture time is less than 10 h when the applied stress is greater than 0.37 MPa and 0.44 MPa in shear and tensile loading modes, respectively. For a creep rupture time longer than 1000 h, the applied constant stress should be smaller than 0.18 MPa and 0.38 MPa for shear and tensile loading modes, respectively. Accordingly, the shear creep strength of 1000 h-aged joint at 1000 h is about 9% of the average shear strength, while the tensile creep strength at 1000 h is only about 16% of the average tensile strength. In addition, the shear and tensile creep strength at 1000 h of the thermally aged joint is enhanced by 13% and 216%, respectively, compared to the non-aged one.

(6) Formation of a rare-earth oxyapatite layer between GC-9 and Crofer 22 H is observed after the joining process of specimens. During the joining process,

La diffuses out from LSM film and reacts with GC-9 to form an oxyapatite ceramic. In addition, Mn diffuses into metallic interconnect and reacts with Cr to form a $(Cr,Mn)_3O_4$ spinel layer on the surface of Crofer 22 H. Volume shrinkage during crystallization of oxyapatite and thermal mismatch at high operation temperature lead to the formation of microcracks within this layer, which causes the fracture of both non-aged shear and tensile joint specimens tested at RT and 800 ℃.

(7) For both non-aged shear and tensile specimens with a short creep rupture time less than 100 h, fracture mainly takes place in the oxyapatite layer, which is similar to that of joint strength testing specimens. For a medium-term creep rupture time (100 h < t_r < 1000 h), Cr diffuses from Crofer 22 H to GC-9 and reacts with Ba to form the $BaCrO_4$ chromate. Fracture site changes from the oxyapatite interlayer to the mixed oxyapatite/$BaCrO_4$ layer when the creep rupture time exceeds 100 h.

(8) Since the LSM film almost fully reacts with GC-9 to form the oxyapatite ceramic, the outward diffusion of Cr from Crofer 22 H could not be completely inhibited, leading to the formation of $BaCrO_4$ and associated microcracks due to thermal mismatch after a long-term operation at high temperature. In this regard, for tensile strength testing of aged specimens, fracture site takes place at the interface between GC-9/oxyapatite and $BaCrO_4$ when tested at RT, but it changes to the interface between GC-9/oxyapatite and $(Cr,Mn)_3O_4$ when tested at 800 ℃.

(9) Oxyapatite and $BaCrO_4$ dominate the creep failure mechanism for 1000 h-aged shear specimens regardless of the length of creep rupture time. In addition, $(Cr,Mn)_3O_4$ spinel layer becomes thicker after thermal aging and might affect the creep failure mechanism of 1000 h-aged tensile joint specimens.

REFERENCES

1. K. Kendall, N. Q. Minh, and S. C. Singhal, “Fuels and Fuel Processing,” Chapter 12 in *High Temperature Solid Oxide Fuel Cells: Fundamentals, Design and Applications*, edited by S. C. Singhal and K. Kendall, Elsevier, Kidlington, UK, 2003.
2. W. Z. Zhu and S. C. Deevi, “A Review on the Status of Anode Materials for Solid Oxide Fuel Cells,” *Materials Science and Engineering: A,* Vol. 362, pp. 228-239, 2003.
3. P. A. Lessing, “A Review of Sealing Technologies Applicable to Solid Oxide Electrolysis Cells,” *Journal of Materials Science,* Vol. 42, pp. 3465-3476, 2007.
4. X.-V. Nguyen, C.-T. Chang, G.-B. Jung, S.-H. Chan, W.-T. Lee, S.-W. Chang, and I. C. Kao, “Study of Sealants for SOFC,” *International Journal of Hydrogen Energy,* Vol. 41, pp. 21812-21819, 2016.
5. J. W. Fergus, “Sealants for Solid Oxide Fuel Cells,” *Journal of Power Sources,* Vol. 147, pp. 46-57, 2005.
6. R. N. Singh, “Sealing Technology for Solid Oxide Fuel Cells (SOFC),” *International Journal of Applied Ceramic Technology,* Vol. 4, pp. 134-144, 2007.
7. S. Le, Z. Shen, X. Zhu, X. Zhou, Y. Yan, K. Sun, N. Zhang, Y. Yuan, and Y. Mao, “Effective Ag–Cuo Sealant for Planar Solid Oxide Fuel Cells,” *Journal of Alloys and Compounds,* Vol. 496, pp. 96-99, 2010.
8. A. G. Sabato, G. Cempura, D. Montinaro, A. Chrysanthou, M. Salvo, E. Bernardo, M. Secco, and F. Smeacetto, “Glass-Ceramic Sealant for Solid Oxide Fuel Cells Application: Characterization and Performance in Dual Atmosphere,” *Journal of Power Sources*, Vol. 328, pp. 262-270, 2016.
9. D. U. Tulyaganov, A. A. Reddy, V. V. Kharton, and J. M. F. Ferreira, “Aluminosilicate-Based Sealants for SOFCs and Other Electrochemical Applications − a Brief Review,” *Journal of Power Sources,* Vol. 242, pp. 486-502, 2013.
10. K. D. Meinhardt, D. S. Kim, Y. S. Chou, and K. S. Weil, “Synthesis and

Properties of a Barium Aluminosilicate Solid Oxide Fuel Cell Glass–Ceramic Sealant," *Journal of Power Sources*, Vol. 182, pp. 188-196, 2008.

11. C.-K. Liu, T.-Y. Yung, and K.-F. Lin, "Isothermal Crystallization Properties of SiO_2-B_2O_3-Al_2O_3-BaO Glass," *Proceedings of the Annual Conference of the Chinese Ceramic Society* (CD-ROM), 2008. (in Chinese)

12. C.-K. Liu, T.-Y. Yung, S.-H. Wu, and K.-F. Lin, "Study on a SiO_2-B_2O_3-Al_2O_3-BaO Glass System for SOFC Applications," *Proceedings of the MRS_Taiwan Annual Meeting* (CD-ROM), 2007. (in Chinese)

13. C.-K. Liu, T.-Y. Yung, and K.-F. Lin, "Effect of La Addition on the Thermal and Crystalline Properties of SiO_2-B_2O_3-Al_2O_3-BaO Glasses," *Proceedings of the Annual Conference of the Chinese Ceramic Society* (CD-ROM), 2007. (in Chinese)

14. H.-T. Chang, "High-Temperature Mechanical Properties of a Glass Sealant for Solid Oxide Fuel Cell," Ph.D. Thesis, National Central University, 2010.

15. J. C. W. Mah, A. Muchtar, M. R. Somalu, and M. J. Ghazali, "Metallic Interconnects for Solid Oxide Fuel Cell: A Review on Protective Coating and Deposition Techniques," *International Journal of Hydrogen Energy,* Vol. 42, pp. 9219-9229, 2017.

16. N. Shaigan, W. Qu, D. G. Ivey, and W. Chen, "A Review of Recent Progress in Coatings, Surface Modifications and Alloy Developments for Solid Oxide Fuel Cell Ferritic Stainless Steel Interconnects," *Journal of Power Sources*, Vol. 195, pp. 1529-1542, 2010.

17. J. Xiao, W. Zhang, C. Xiong, B. Chi, J. Pu, and L. Jian, "Oxidation Behavior of Cu-Doped $MnCo_2O_4$ Spinel Coating on Ferritic Stainless Steels for Solid Oxide Fuel Cell Interconnects," *International Journal of Hydrogen Energy,* Vol. 41, pp. 9611-9618, 2016.

18. R. K. Lenka, P. K. Patro, J. Sharma, T. Mahata, and P. K. Sinha, "Evaluation of $La_{0.75}Sr_{0.25}Cr_{0.5}Mn_{0.5}O_3$ Protective Coating on Ferritic Stainless Steel Interconnect for SOFC Application," *International Journal of Hydrogen Energy,* Vol. 41, pp. 20365-20372, 2016.

19. A. Harthøj, T. Holt, and P. Møller, "Oxidation Behaviour and Electrical Properties of Cobalt/Cerium Oxide Composite Coatings for Solid Oxide Fuel Cell Interconnects," *Journal of Power Sources,* Vol. 281, pp. 227-237,

2015.

20. M. Palcut, L. Mikkelsen, K. Neufeld, M. Chen, R. Knibbe, and P. V. Hendriksen, “Improved Oxidation Resistance of Ferritic Steels with LSM Coating for High Temperature Electrochemical Applications,” *International Journal of Hydrogen Energy,* Vol. 37, pp. 8087-8094, 2012.

21. S.-S. Pyo, S.-B. Lee, T.-H. Lim, R.-H. Song, D.-R. Shin, S.-H. Hyun, and Y.-S. Yoo, “Characteristic of $(La_{0.8}Sr_{0.2})_{0.98}MnO_3$ Coating on Crofer22APU Used as Metallic Interconnects for Solid Oxide Fuel Cell,” *International Journal of Hydrogen Energy*, Vol. 36, pp. 1868-1881, 2011.

22. S. Lee, C.-L. Chu, M.-J. Tsai, and J. Lee, “High Temperature Oxidation Behavior of Interconnect Coated with LSCF and LSM for Solid Oxide Fuel Cell by Screen Printing,” *Applied Surface Science,* Vol. 256, pp. 1817-1824, 2010.

23. C. Chu, J. Lee, T. Lee, and Y. Cheng, “Oxidation Behavior of Metallic Interconnect Coated with La–Sr–Mn Film by Screen Painting and Plasma Sputtering,” *International Journal of Hydrogen Energy,* Vol. 34, pp. 422-434, 2009.

24. C. Lee and J. Bae, “Oxidation-Resistant Thin Film Coating on Ferritic Stainless Steel by Sputtering for Solid Oxide Fuel Cells,” *Thin Solid Films,* Vol. 516, pp. 6432-6437, 2008.

25. D.-J. Jan, C.-T. Lin, and C.-F. Ai, “Structural Characterization of $La_{0.67}Sr_{0.33}MnO_3$ Protective Coatings for Solid Oxide Fuel Cell Interconnect Deposited by Pulsed Magnetron Sputtering,” *Thin Solid Films,* Vol. 516, pp. 6300-6304, 2008.

26. Z. Yang, G.-G. Xia, G. D. Maupin, and J. W. Stevenson, “Conductive Protection Layers on Oxidation Resistant Alloys for SOFC Interconnect Applications,” *Surface and Coatings Technology,* Vol. 201, pp. 4476-4483, 2006.

27. J. H. Zhu, M. J. Lewis, S. W. Du, and Y. T. Li, “CeO_2-Doped $(Co,Mn)_3O_4$ Coatings for Protecting Solid Oxide Fuel Cell Interconnect Alloys,” *Thin Solid Films*, Vol. 596, pp. 179-184, 2015.

28. J. Xiao, W. Zhang, C. Xiong, B. Chi, J. Pu, and L. Jian, “Oxidation of $MnCu_{0.5}Co_{1.5}O_4$ Spinel Coated Sus430 Alloy Interconnect in Anode and Cathode Atmospheres for Intermediate Temperature Solid Oxide Fuel Cell,”

International Journal of Hydrogen Energy, Vol. 40, pp. 1868-1876, 2015.

29. Z. Yang, G. Xia, X. Li, and J. Stevenson, "$(Mn,Co)_3O_4$ Spinel Coatings on Ferritic Stainless Steels for SOFC Interconnect Applications," *International Journal of Hydrogen Energy*, Vol. 32, pp. 3648-3654, 2007.

30. J. G. Grolig, P. Alnegren, J. Froitzheim, and J.-E. Svensson, "Copper Iron Conversion Coating for Solid Oxide Fuel Cell Interconnects," *Journal of Power Sources*, Vol. 297, pp. 534-539, 2015.

31. C.-K. Lin, Y.-A. Liu, S.-H. Wu, C.-K. Liu, and R.-Y. Lee, "Joint Strength of a Solid Oxide Fuel Cell Glass–Ceramic Sealant with Metallic Interconnect in a Reducing Environment," *Journal of Power Sources*, Vol. 280, pp. 272-288, 2015.

32. C.-K. Lin, W.-H. Shiu, S.-H. Wu, C.-K. Liu, and R.-Y. Lee, "Interfacial Fracture Resistance of the Joint of a Solid Oxide Fuel Cell Glass–Ceramic Sealant with Metallic Interconnect," *Journal of Power Sources*, Vol. 261, pp. 227-237, 2014.

33. C.-K. Lin, K.-L. Lin, J.-H. Yeh, S.-H. Wu, and R.-Y. Lee, "Creep Rupture of the Joint of a Solid Oxide Fuel Cell Glass–Ceramic Sealant with Metallic Interconnect," *Journal of Power Sources*, Vol. 245, pp. 787-795, 2014.

34. J. Chen, H. Yang, R. Chadeyron, D. Tang, and T. Zhang, "Tuning the Interfacial Reaction Between $CaO–SrO–Al_2O_3–B_2O_3–SiO_2$ Sealing Glass–Ceramics and Cr-Containing Interconnect: Crystalline Structure vs. Glass Structure," *Journal of the European Ceramic Society*, Vol. 34, pp. 1989-1996, 2014.

35. C.-K. Lin, J.-Y. Chen, J.-W. Tian, L.-K. Chiang, and S.-H. Wu, "Joint Strength of a Solid Oxide Fuel Cell Glass–Ceramic Sealant with Metallic Interconnect," *Journal of Power Sources*, Vol. 205, pp. 307-317, 2012.

36. F. Smeacetto, A. De Miranda, S. Cabanas Polo, S. Molin, D. Boccaccini, M. Salvo, and A. R. Boccaccini, "Electrophoretic Deposition of $Mn_{1.5}Co_{1.5}O_4$ on Metallic Interconnect and Interaction with Glass-Ceramic Sealant for Solid Oxide Fuel Cells Application," *Journal of Power Sources*, Vol. 280, pp. 379-386, 2015.

37. M. K. Mahapatra and K. Lu, "Seal Glass Compatibility with Bare and $(Mn,Co)_3O_4$ Coated Crofer 22 Apu Alloy in Different Atmospheres,"

Journal of Power Sources, Vol. 196, pp. 700-708, 2011.

38. J. P. Choi, K. S Weil, Y. M Chou, J. W. Stevenson, and Z. G. Yang, "Development of MnCoO Coating with New Aluminizing Process for Planar SOFC Stacks," *International Journal of Hydrogen Energy,* Vol. 36, pp. 4549-4556, 2011.

39. C.-K. Lin, L.-H. Huang, L.-K. Chiang, and Y.-P. Chyou, "Thermal Stress Analysis of Planar Solid Oxide Fuel Cell Stacks: Effects of Sealing Design," *Journal of Power Sources,* Vol. 192, pp. 515-524, 2009.

40. C.-K. Lin, T.-T. Chen, Y.-P. Chyou, and L.-K. Chiang, "Thermal Stress Analysis of a Planar SOFC Stack," *Journal of Power Sources,* Vol. 164, pp. 238-251, 2007.

41. J. Malzbender, J. Mönch, R. W. Steinbrech, T. Koppitz, S. M. Gross, and J. Remmel, "Symmetric Shear Test of Glass-Ceramic Sealants at SOFC Operation Temperature," *Journal of Materials Science,* Vol. 42, pp. 6297-6301, 2007.

42. F. Smeacetto, M. Salvo, M. Ferraris, V. Casalegno, P. Asinari, and A. Chrysanthou, "Characterization and Performance of Glass–Ceramic Sealant to Join Metallic Interconnects to YSZ and Anode-Supported-Electrolyte in Planar SOFCs," *Journal of the European Ceramic Society,* Vol. 28, pp. 2521-2527, 2008.

43. J.-H. Yeh, "Analysis of High-Tenperature Mechanical Durability for the Joint of Glass Ceramic Sealant and Metallic Interconnect for Solid Oxide Fuel Cell," M.S. Thesis, National Central University, 2011.

44. N. E. Dowling, *Mechanical Behavior of Materials: Engineering Methods for Deformation, Fracture, and Fatigue*, 4th Ed., Prentice Hall, New Jersey, USA, 2012.

45. M. G. Makowska, L. T. Kuhn, H. L. Frandsen, E. M. Lauridsen, S. De Angelis, L. N. Cleemann, M. Morgano, P. Trtik, and M. Strobl, "Coupling between Creep and Redox Behavior in Nickel - Yttria Stabilized Zirconia Observed in-Situ by Monochromatic Neutron Imaging," *Journal of Power Sources,* Vol. 340, pp. 167-175, 2017.

46. L. Esposito, D. N. Boccaccini, G. P. Pucillo, and H. L. Frandsen, "Secondary Creep of Porous Metal Supports for Solid Oxide Fuel Cells by a CDM Approach," *Materials Science and Engineering: A,* Vol. 691, pp.

155-161, 2017.

47. H. L. Frandsen, M. Makowska, F. Greco, C. Chatzichristodoulou, D. W. Ni, D. J. Curran, M. Strobl, L. T. Kuhn, and P. V. Hendriksen, “Accelerated Creep in Solid Oxide Fuel Cell Anode Supports During Reduction,” *Journal of Power Sources*, Vol. 323, pp. 78-89, 2016.

48. C.-K. Lin, K.-L. Lin, J.-H. Yeh, W.-H. Shiu, C.-K. Liu, and R.-Y. Lee, “Aging Effects on High-Temperature Creep Properties of a Solid Oxide Fuel Cell Glass-Ceramic Sealant,” *Journal of Power Sources,* Vol. 241, pp. 12-19, 2013.

49. Y.-T. Chiu and C.-K. Lin, “Effects of Nb and W Additions on High-Temperature Creep Properties of Ferritic Stainless Steels for Solid Oxide Fuel Cell Interconnect,” *Journal of Power Sources,* Vol. 198, pp. 149-157, 2012.

50. J. Wei, G. Pećanac, and J. Malzbender, “Mechanical Behavior of Silver Reinforced Glass–Ceramic Sealants for Solid Oxide Fuel Cells,” *Ceramics International,* Vol. 41, pp. 15122-15127, 2015.

51. Y.-T. Chiu, C.-K. Lin, and J.-C. Wu, “High-Temperature Tensile and Creep Properties of a Ferritic Stainless Steel for Interconnect in Solid Oxide Fuel Cell,” *Journal of Power Sources,* Vol. 196, pp. 2005-2012, 2011.

52. H.-L. Hsu, “Environmental Effects on the Creep Properties of Joints in Solid Oxide Fuel Cell,” M.S. Thesis, National Central University, 2015.

53. F.-L. Hou, “Effect of LSM Coating on Joining Strength Between Metallic Interconnect and Galss-Ceramic Sealant for Solid Oxide Fuel Cell,” M.S. Thesis, National Central University, 2015.

54. Y.-T. Chiu, “Creep and Thermo-Mechanical Fatigue Properties of Ferritic Stainless Steels for Use in Solid Oxide Fuel Cell Interconnect,” Ph.D. Thesis, National Central University, 2012.

55. C.-K. Liu, T.-Y. Yung, K.-F. Lin, R.-Y. Lee, and T.-S. Lee, Glass-Ceramic Sealant for Planar Solid Oxide Fuel Cells, United States Patent No.7,897,530 B2, 2011.

56. J.-Y. Chen, “Analysis of Mechanical Properties for the Joint of Metallic Interconnect and Glass Ceramic in Solid Oxide Fuel Cell,” M.S. Thesis, National Central University, 2010.

57. E. Apel, W. Höland, H. C. Van't, U. Bolle, and V. M. Rheinberger, Apatite Glass Ceramic Based on Siliceous Oxyapatites, United States Patent No. 7,166,548 B2, 2007.

58. P. Yang, C.-K. Liu, J.-Y. Wu, W.-J. Shong, R.-Y. Lee, and C.-C. Sung, “Effects of Pre-Oxidation on the Microstructural and Electrical Properties of $La_{0.67}Sr_{0.33}MnO_{3-\delta}$ Coated Ferritic Stainless Steels,” *Journal of Power Sources*, Vol. 213, pp. 63-68, 2012.

TABLES

Table. 1 Common compositional modifiers for silicate-based glass–ceramic sealants. [10]

Modifier	Function
Al_2O_3	Allows control over viscosity through the rate of crystallization
B_2O_3	Reduces CTE, T_g, T_s, and viscosity and improves wetting
BaO, CaO, MgO	Reduces T_g and T_s, and raises CTE in the glass-ceramic
Cr_2O_3, V_2O_5	Reduces surface tension
La_2O_3, Nd_2O_3, Y_2O_3,	Used as a viscosity modifier and long-term CTE stabilizer
CuO, NiO, CoO, MnO	Improves surface adherence
TiO_2, ZrO_2, SrO	Nucleates crystallization

Table. 2 Comparison of various coating materials in terms of electric conductivity, Cr migration inhibition, and oxidation rate reduction. [15]

Coating material	Electric conductivity	Cr migration inhibition	Oxidation rate reduction
Reactive element oxide	Fair	Poor	Good
Rare earth perovskite	Good	Fair	Poor
Composite spinel oxide	Good	Good	Fair

Table. 3 Chemical composition of Crofer 22 H alloy (in wt.%).

Fe	C	Cr	Mn	Si	Ti	Nb
Bal.	0.007	22.93	0.43	0.21	0.07	0.51
Cu	S	P	Al	W	La	
0.02	<0.002	0.014	0.02	1.94	0.08	

Table. 4 Average of mechanical properties for Crofer 22 H alloy. [54]

Temperature (℃)	Yield strength (MPa)	Ultimate tensile strength (MPa)	Young's modulus (GPa)	Elongation (in 12 mm) (%)
25	406	567	205	27
600	286	359	181	29
650	241	295	161	30
700	204	219	142	39
750	140	147	88	54
800	120	123	86	55

Table. 5 Average biaxial flexural strength (σ_f) for variously aged GC-9 glass at different temperatures. [43]

Average flexural strength	Aged condition	Temperature				
		25 ℃	650 ℃	700 ℃	750 ℃	800 ℃
σ_f (MPa)	Non-aged	38	50	47	33	18
	100 h-aged	38	49	53	54	32
	1000 h-aged	45	59	49	57	36

Table. 6 Average joint strength and creep strength (at 1000 h) of non-aged and 1000 h-aged joint specimens tested in air

Test temperature (℃)	Loading mode	Specimen condition	Average joint strength (MPa)	Creep strength (at 1000 h)
25	Shear	Non-aged	1.45	N/A
25	Shear	1000 h-aged	4.47	N/A
800	Shear	Non-aged	0.38	0.16
800	Shear	1000 h-aged	1.98	0.18
25	Tensile	Non-aged	9.37	N/A
25	Tensile	1000 h-aged	19.91	N/A
800	Tensile	Non-aged	3.58	0.12
800	Tensile	1000 h-aged	2.41	0.38

Table. 7 Fracture site of non-aged and 1000 h-aged shear and tensile strength test specimens

Test temperature (℃)	Loading mode	Specimen condition	Fracture site*
25	Shear	Non-aged	A+B
25	Shear	1000 h-aged	C+D
800	Shear	Non-aged	A
800	Shear	1000 h-aged	C+D
25	Tensile	Non-aged	A+B
25	Tensile	1000 h-aged	C+D
800	Tensile	Non-aged	A
800	Tensile	1000 h-aged	F

*A: in the oxyapatite ceramic layer; B: in the GC-9 glass-ceramic layer; C: in the $BaCrO_4$ layer; D: at the interface between the mixed GC-9/oxyapatite and $BaCrO_4$ layer; E: in the mixed oxyapatite/$BaCrO_4$ layer; F: at the interface between mixed GC-9/oxyapatite and $(Cr,Mn)_3O_4$ layer.

Table. 8 Creep fracture path of non-aged and 1000 h-aged joint specimens

Loading mode	Specimen condition	Creep rupture time	Fracture site*
Shear	Non-aged	0-100	A
Shear	Non-aged	100-1000	D
Shear	1000 h-aged	0-100	D
Shear	1000 h-aged	100-1000	D+E
Tensile	Non-aged	0-100	A
Tensile	Non-aged	100-1000	D
Tensile	1000 h-aged	0-100	F
Tensile	1000 h-aged	100-1000	D+E+F

FIGURES

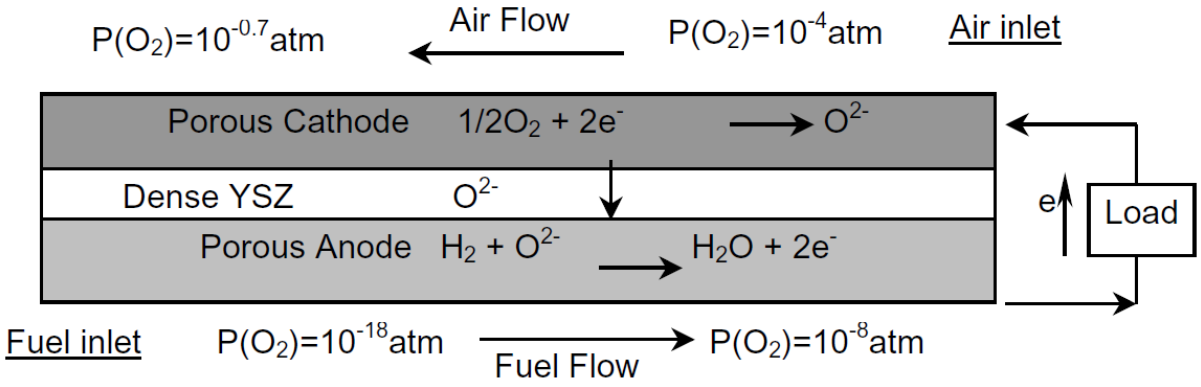

Fig. 1 Operating principle of SOFC using hydrogen as fuel. [2]

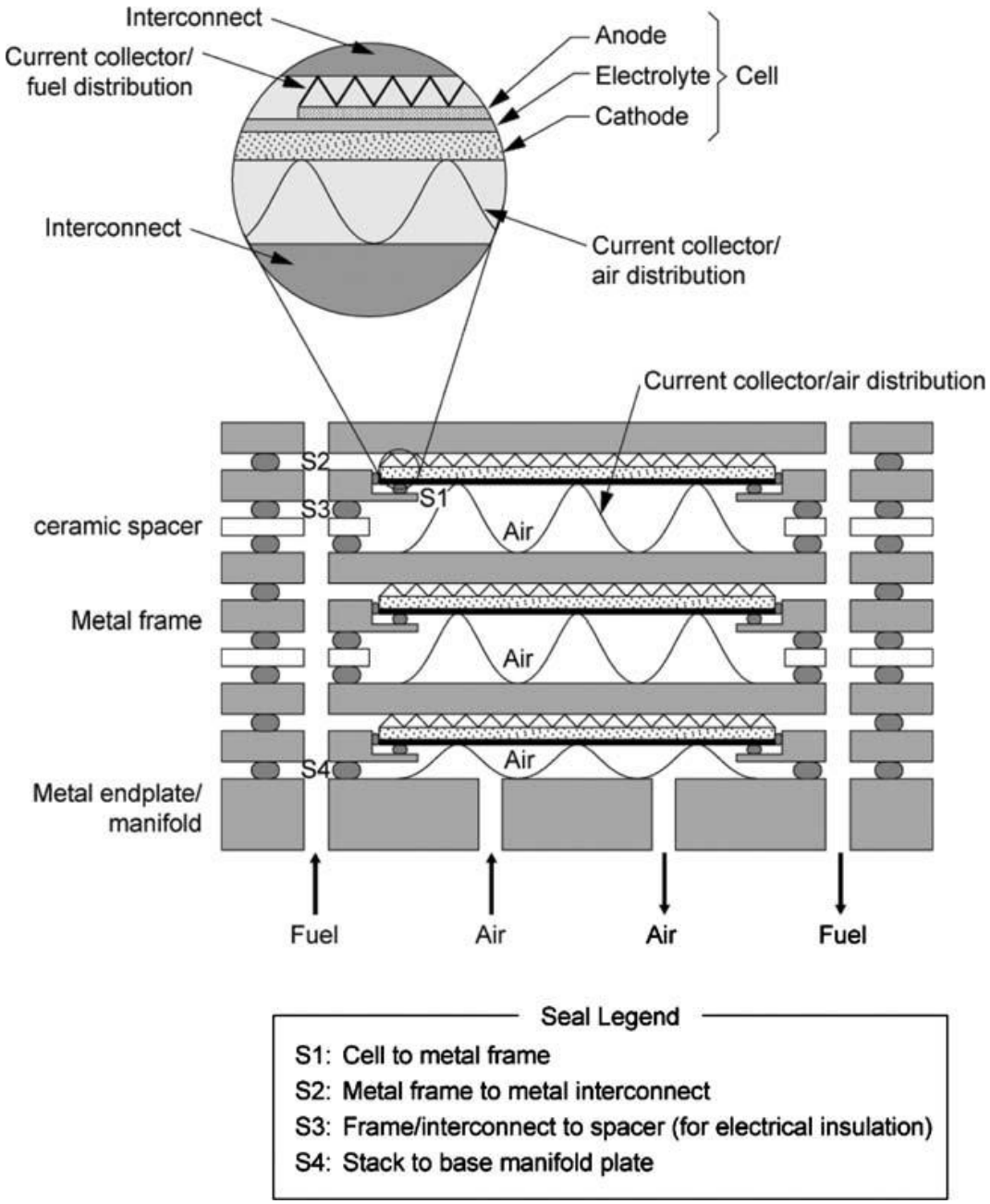

Fig. 2 Structural design of a planar SOFC stack. [3]

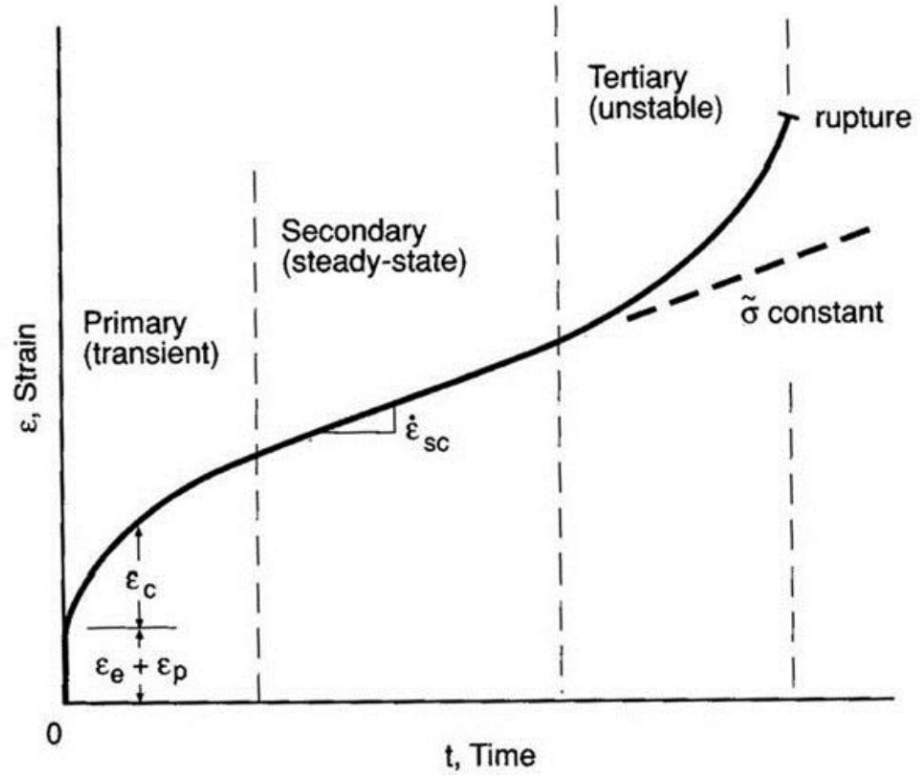

Fig. 3 A typical strain-time relationship during creep under constant load.

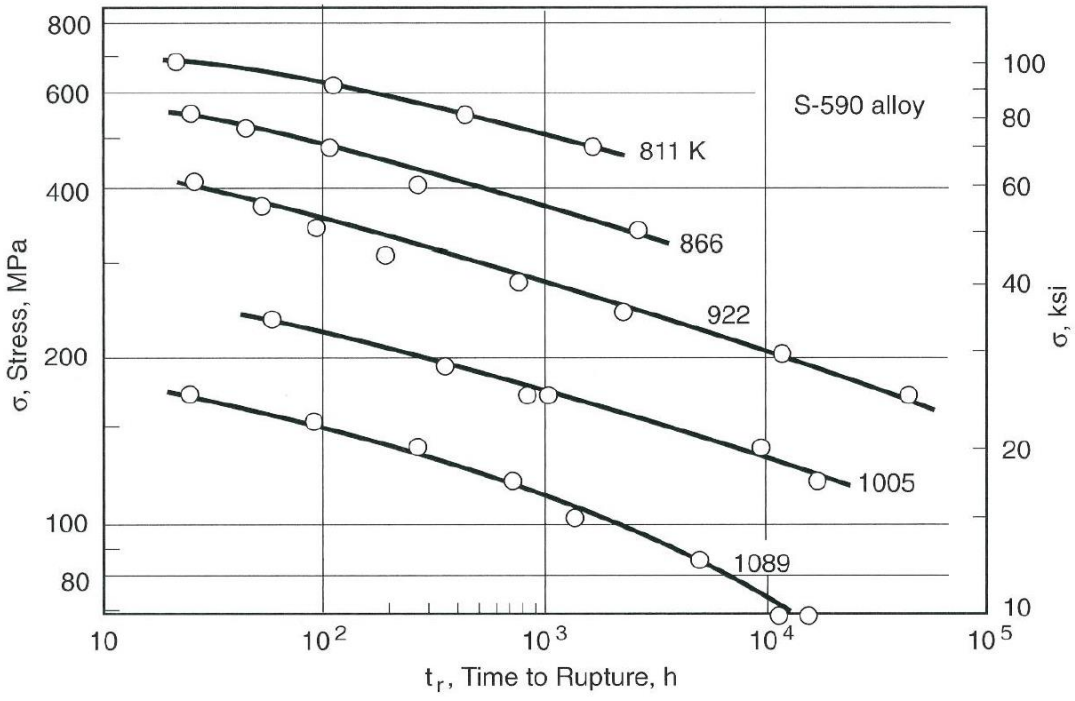

[44]

Fig. 4 Stress versus rupture life curves for S-590, an iron-based, heat-resisting alloy. [44]

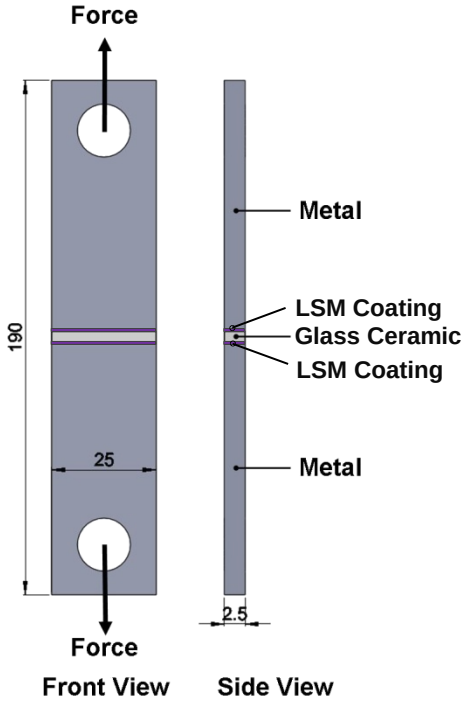

(a)

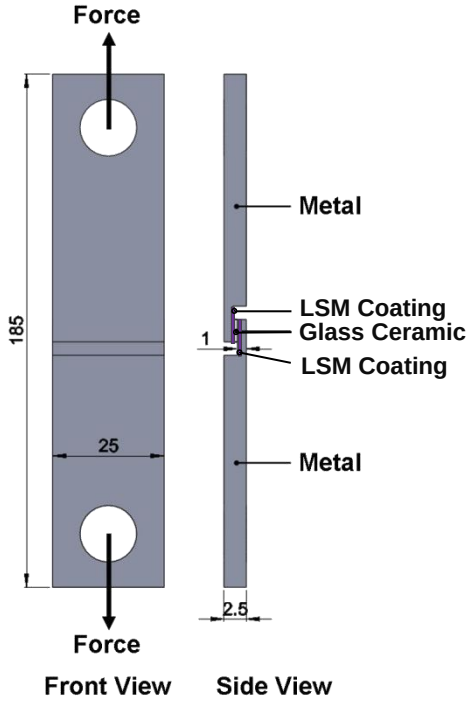

(b)

Fig. 5 Scheme of two types of joint specimens: (a) tensile specimen; (b) shear specimen. (Dimensions: mm)

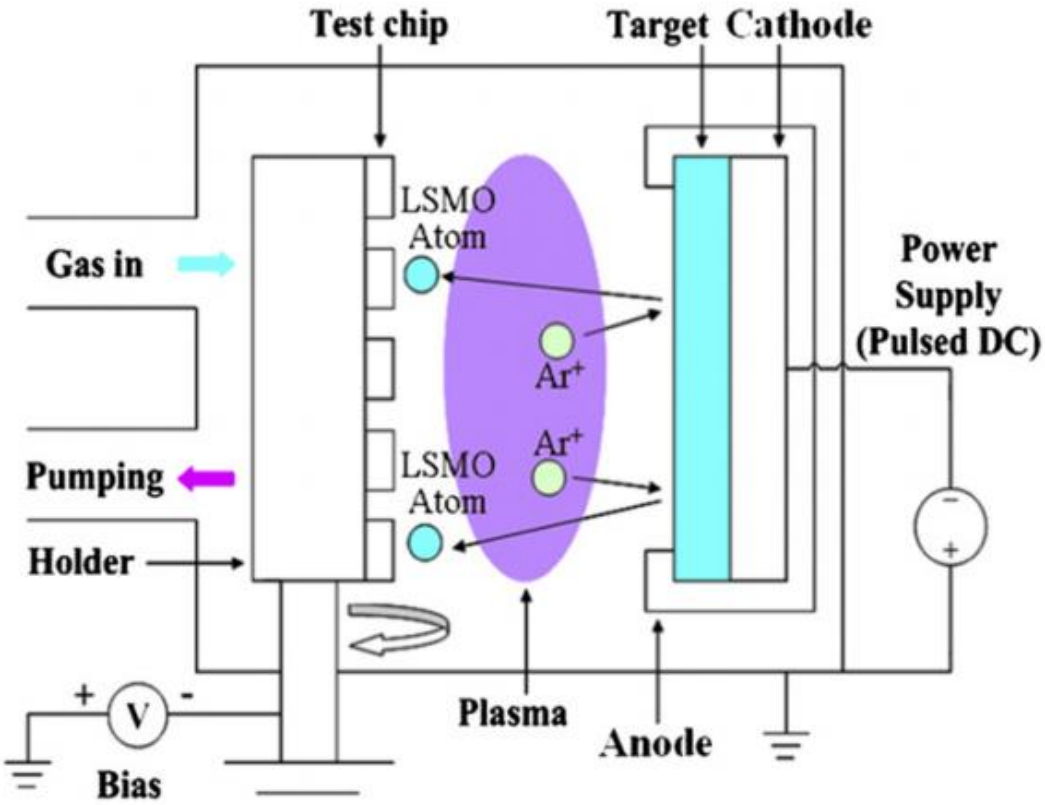

Fig. 6 Schematic diagram of a pulsed DC magnetron sputtering system. [58]

Fig. 7 Photograph of the box furnace for thermal aging treatment.

Fig. 8 Photograph of experimental setup for mechanical test.

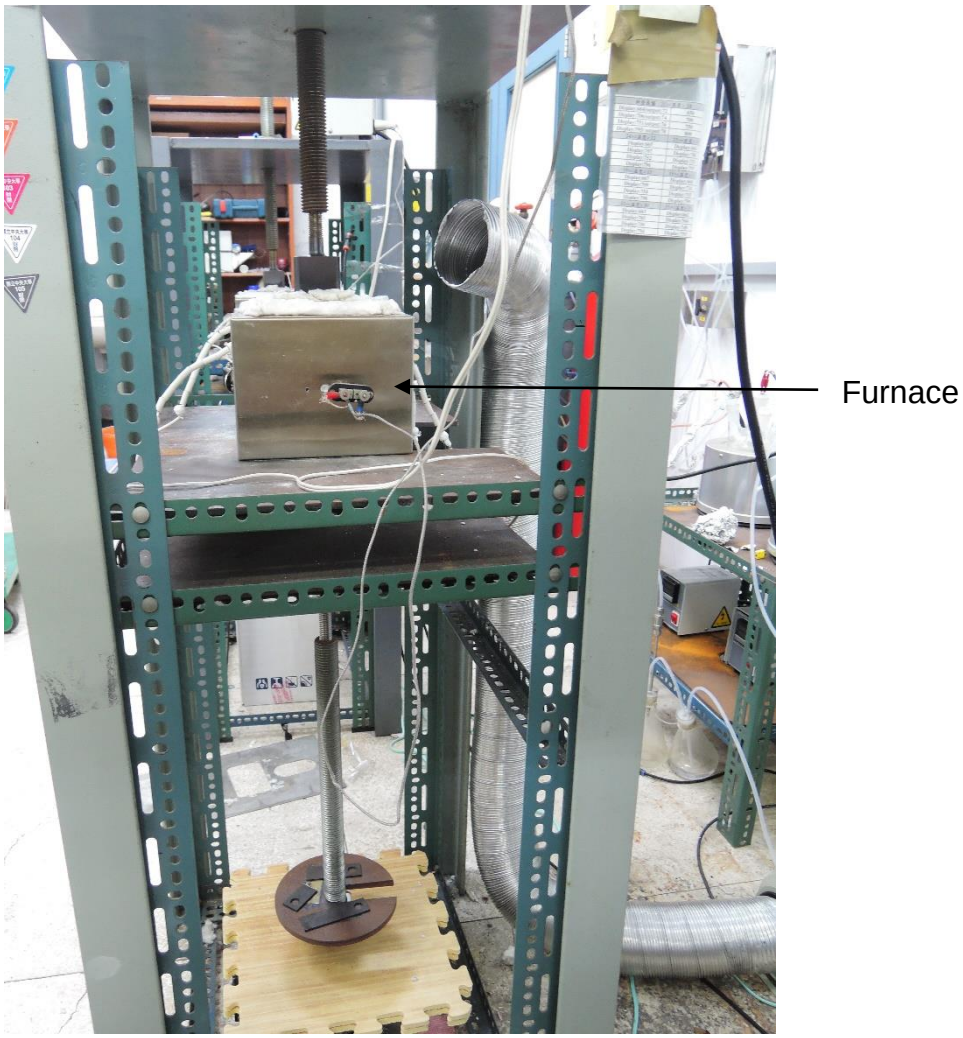

Fig. 9 Photograph of experimental setup for high-temperature creep test.

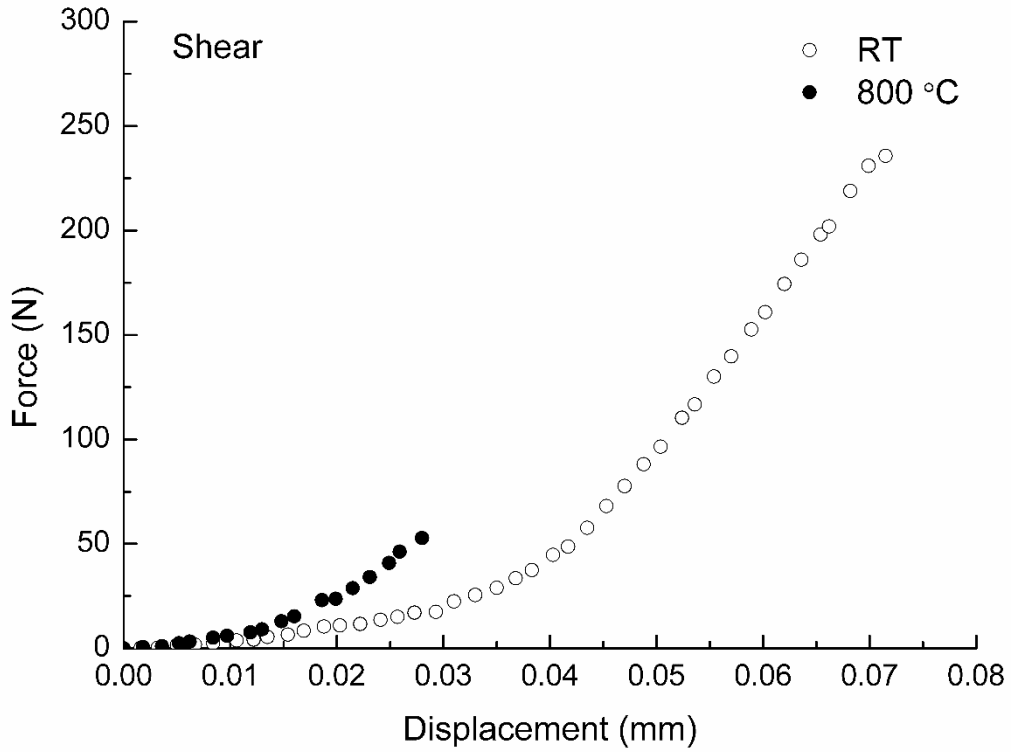

Fig. 10 Typical force-displacement curves of the non-aged joint specimens tested under shear loading in air at RT and 800 ℃.

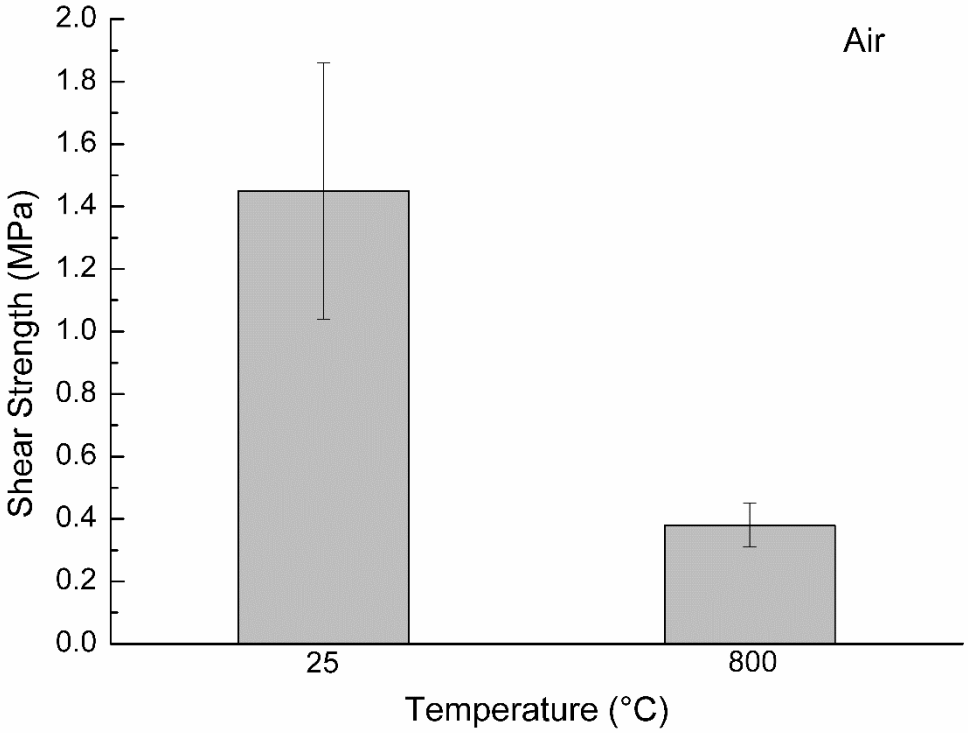

Fig. 11 Shear strength of non-aged joint specimens tested in air at RT and 800 ℃.

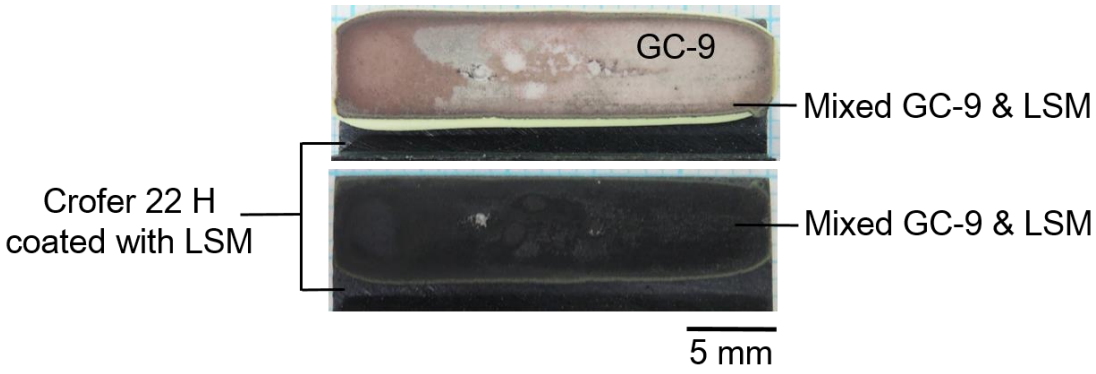

(a)

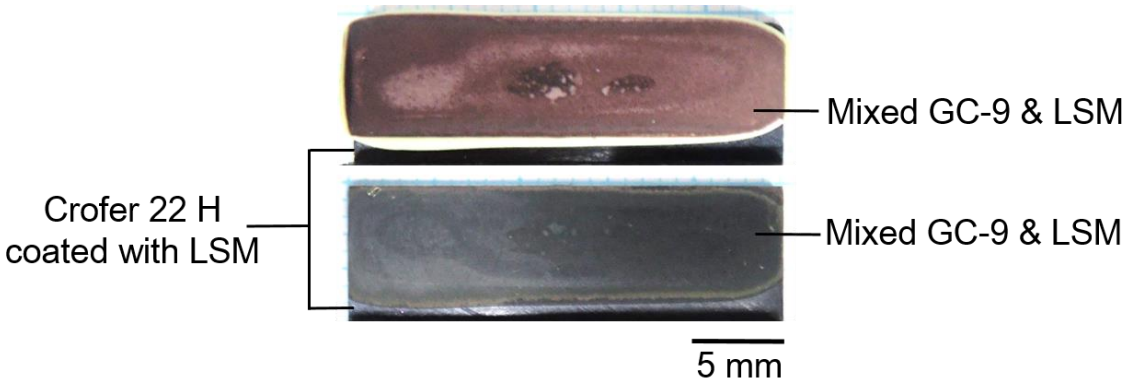

(b)

Fig. 12 Failure patterns of non-aged shear specimens tested in air at (a) RT and (b) 800 ℃.

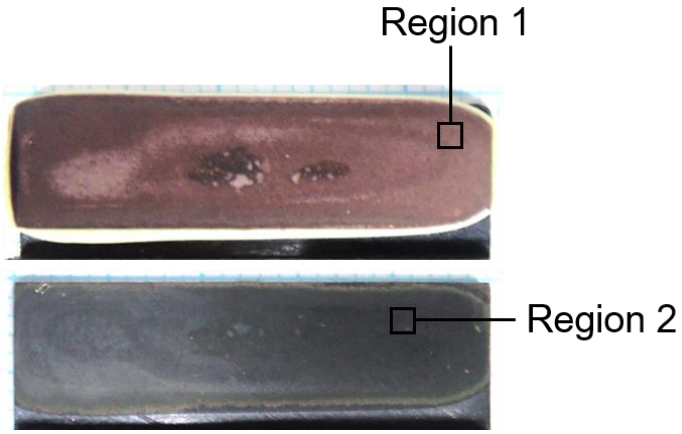

(a)

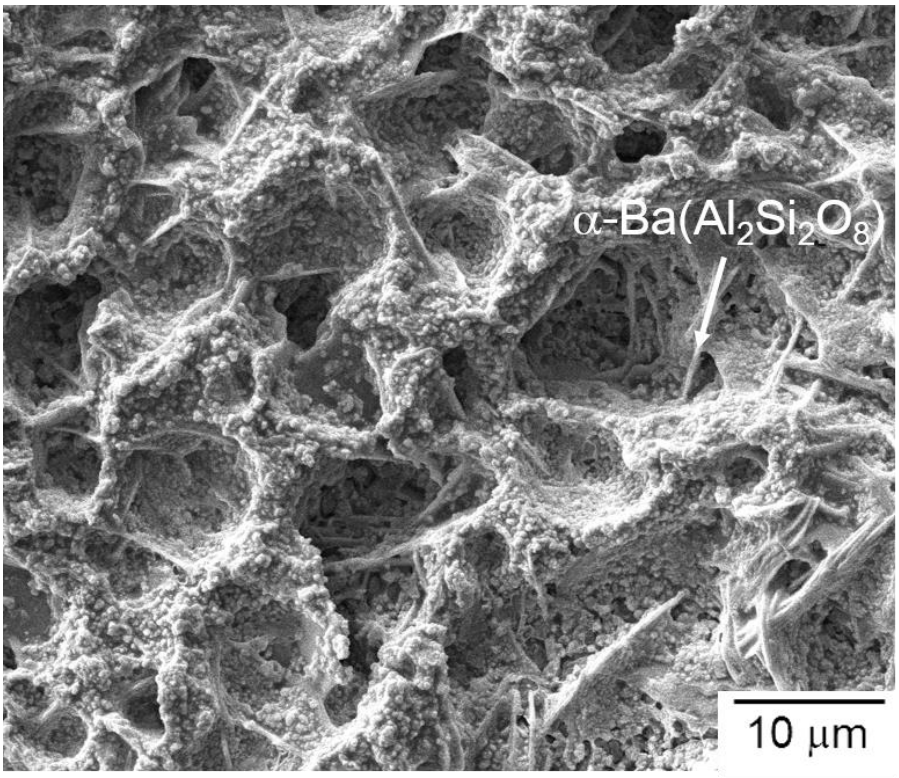

(b)

Fig. 13 Fracture surface of the non-aged shear specimen shown in Fig. 12(b): (a) optical micrographs showing the observed regions of SEM; (b) SEM micrograph of Region 1 (GC-9 side); (c) SEM micrograph of Region 2 (metal side).

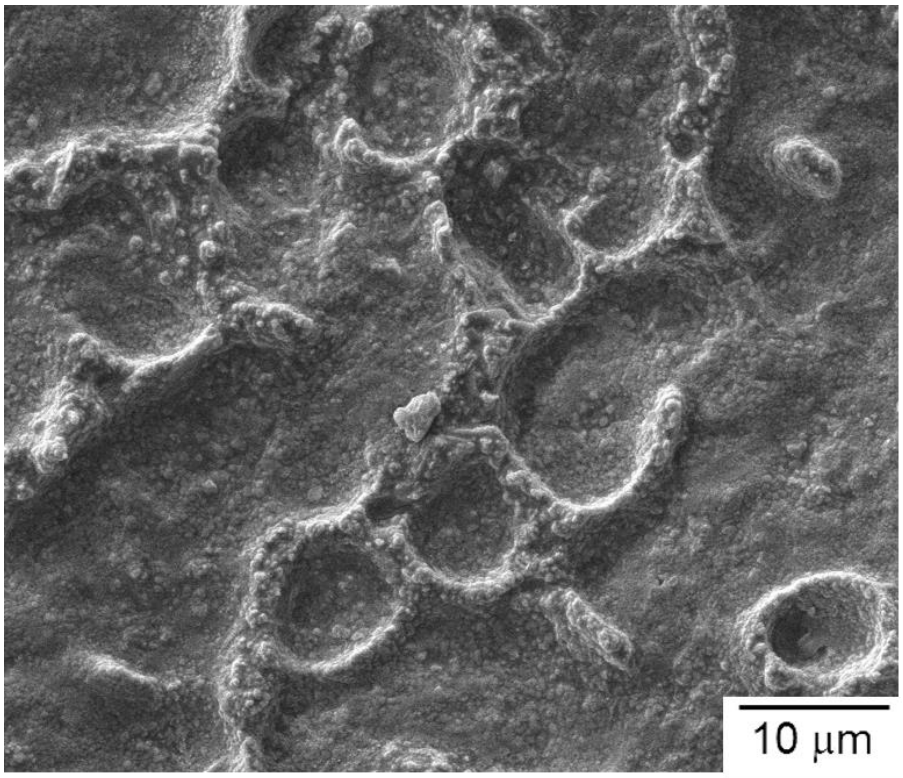

(c)

Fig. 13 (continued)

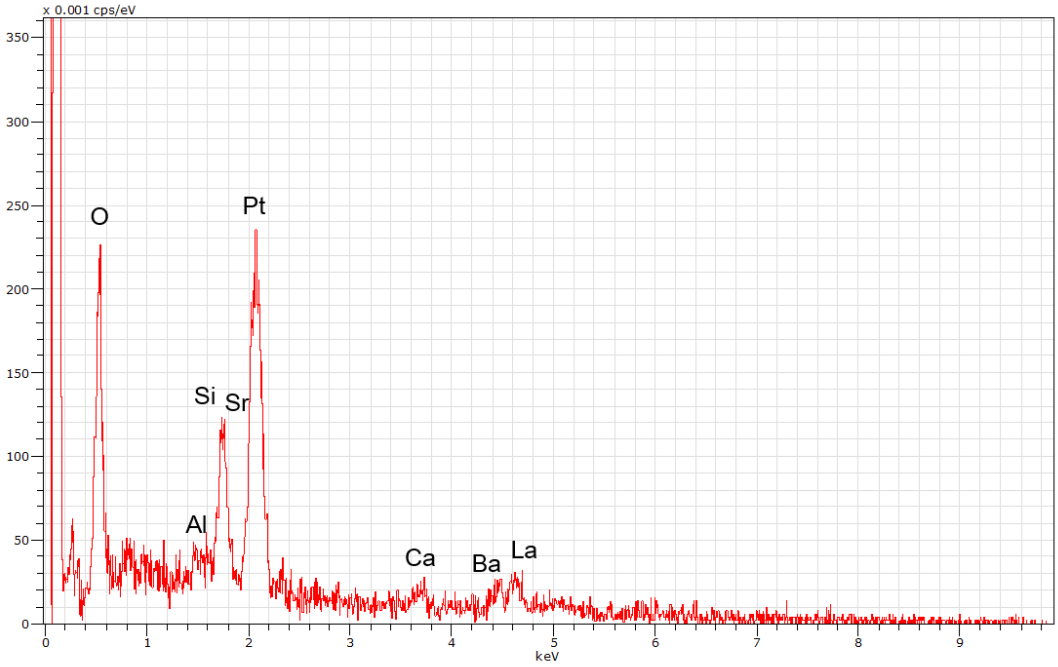

(a)

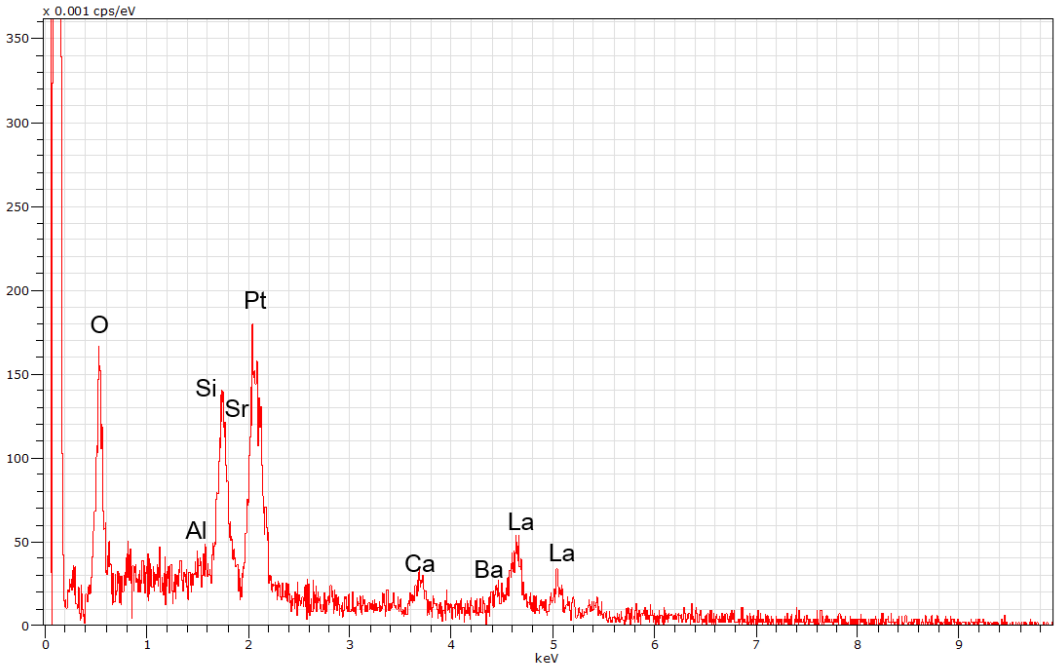

(b)

Fig. 14 EDS analysis results of the fracture surface of a non-aged shear joint specimens: (a) Region 1 (in Fig. 13(b)); (b) Region 2 (in Fig. 13(c)).

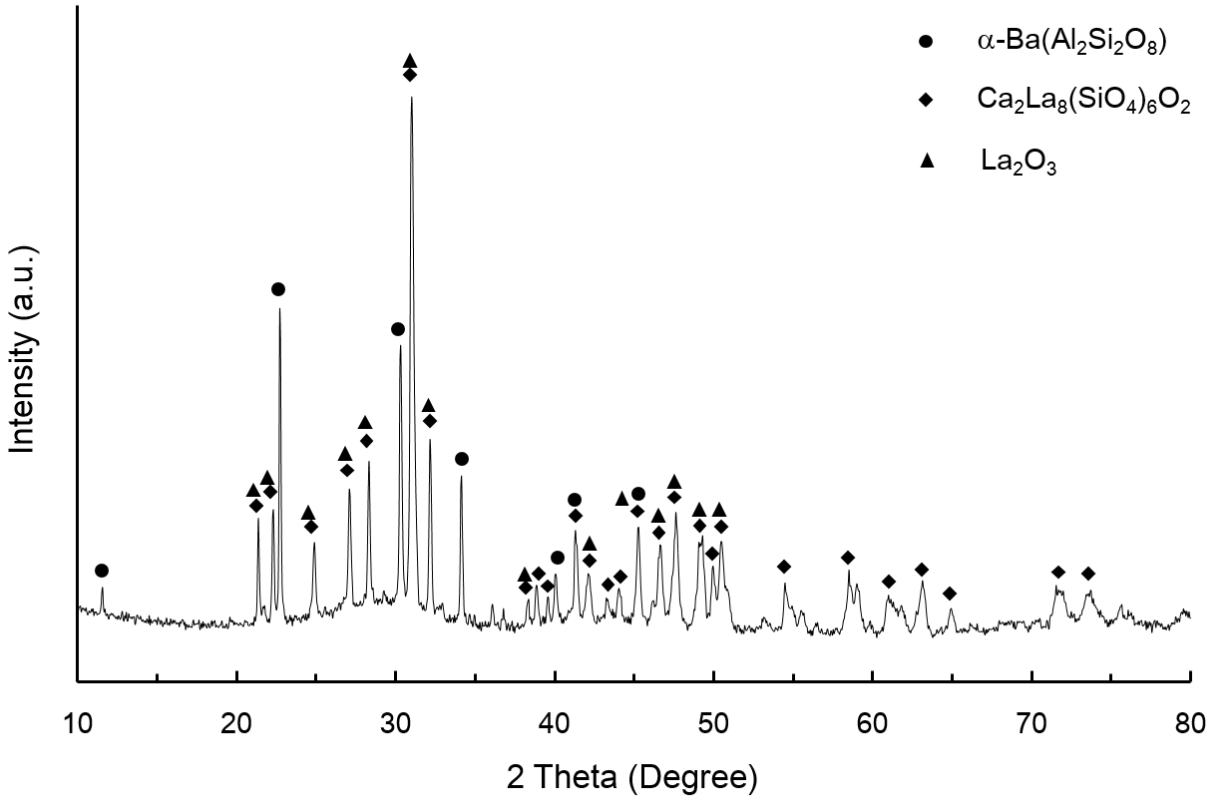

Fig. 15 XRD pattern of the fracture surface of non-aged shear joint specimen (in Fig. 12(b)).

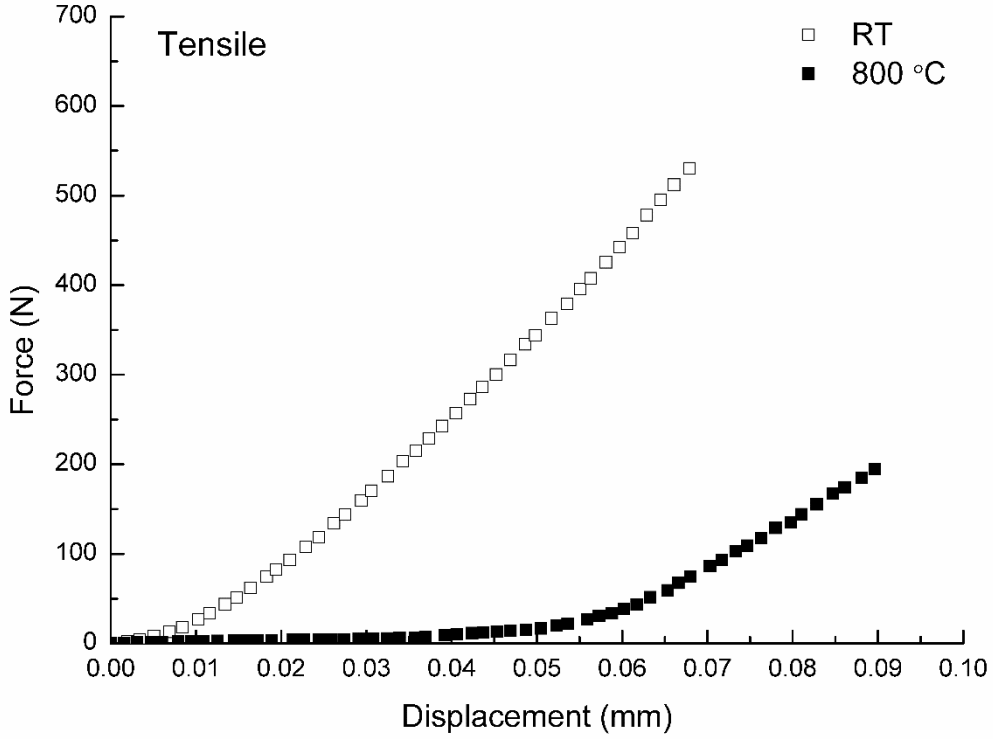

Fig. 16 Typical force-displacement curves of the non-aged joint specimens tested under tensile loading in air at RT and 800 ℃.

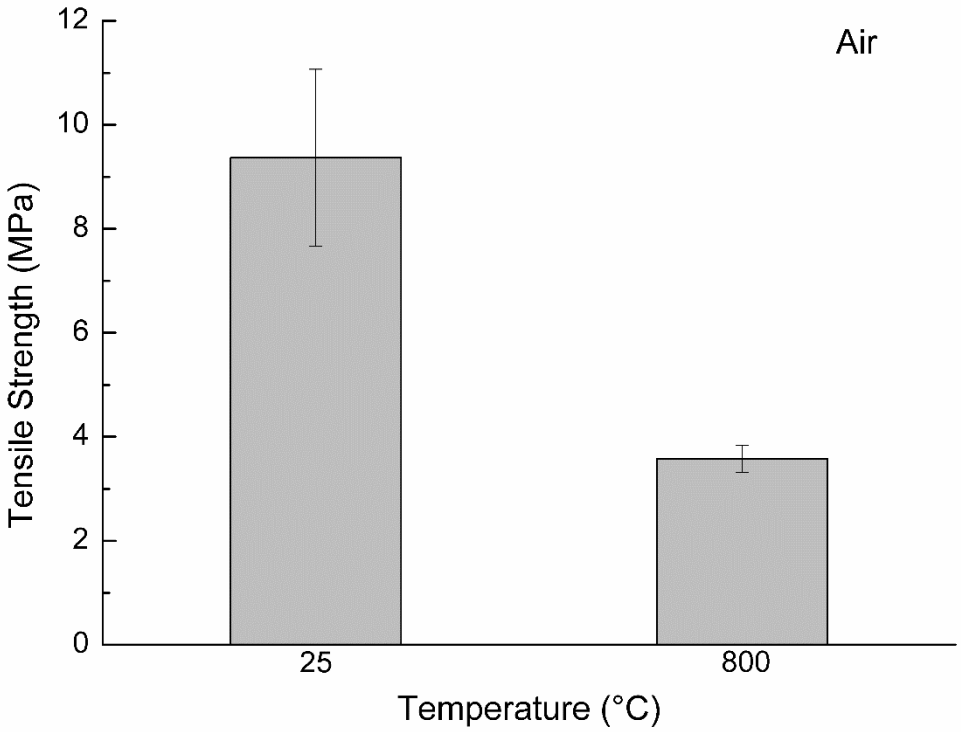

Fig. 17 Tensile strength of non-aged joint specimens tested in air at RT and 800 ℃.

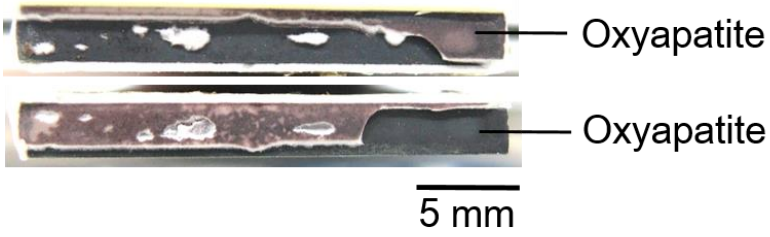

(a)

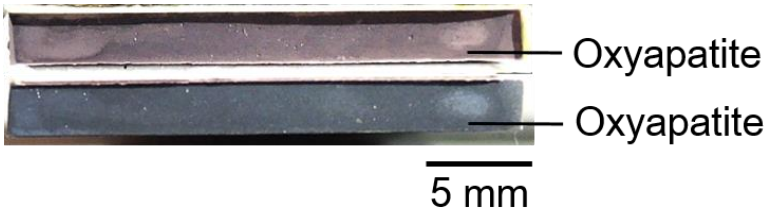

(b)

Fig. 18 Failure patterns of non-aged tensile specimens tested in air at (a) RT and (b) 800 ℃.

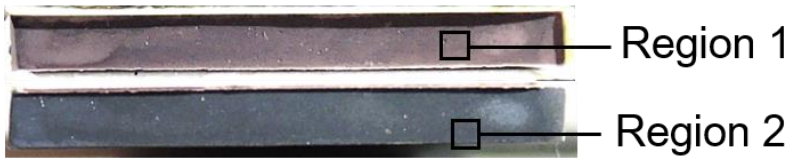

(a)

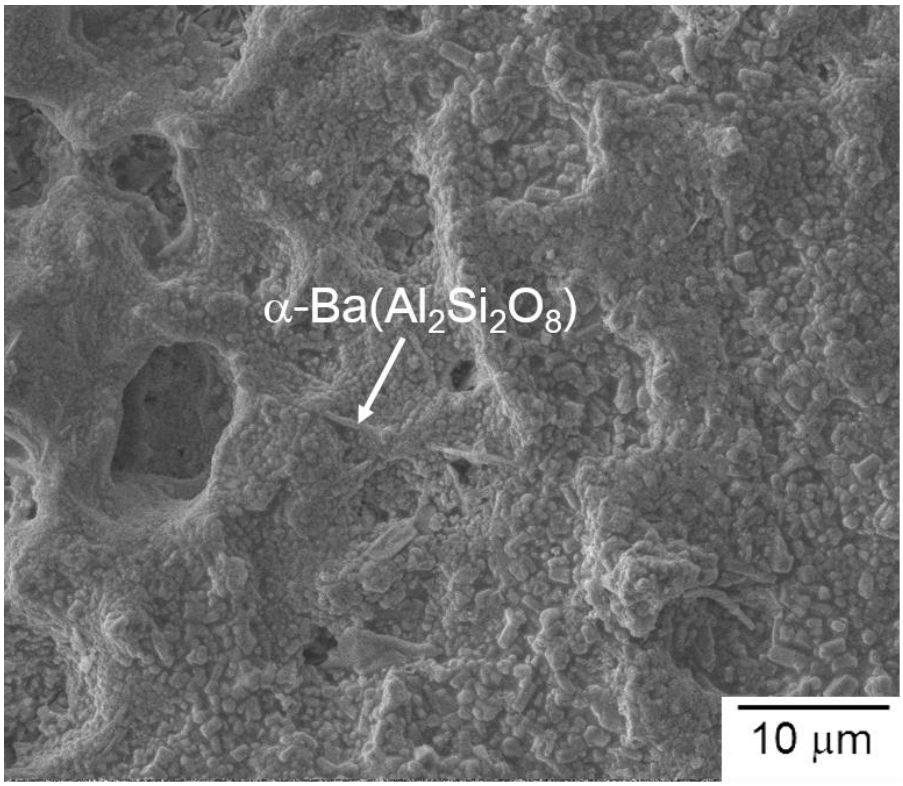

(b)

Fig. 19 Fracture surface of the non-aged tensile specimen shown in Fig. 18(b): (a) optical micrographs showing the observed regions of SEM; (b) SEM micrograph of Region 1 (GC-9 side); (c) SEM micrograph of Region 2 (metal side); (d) High magnification view of spinel layer in Region 2.

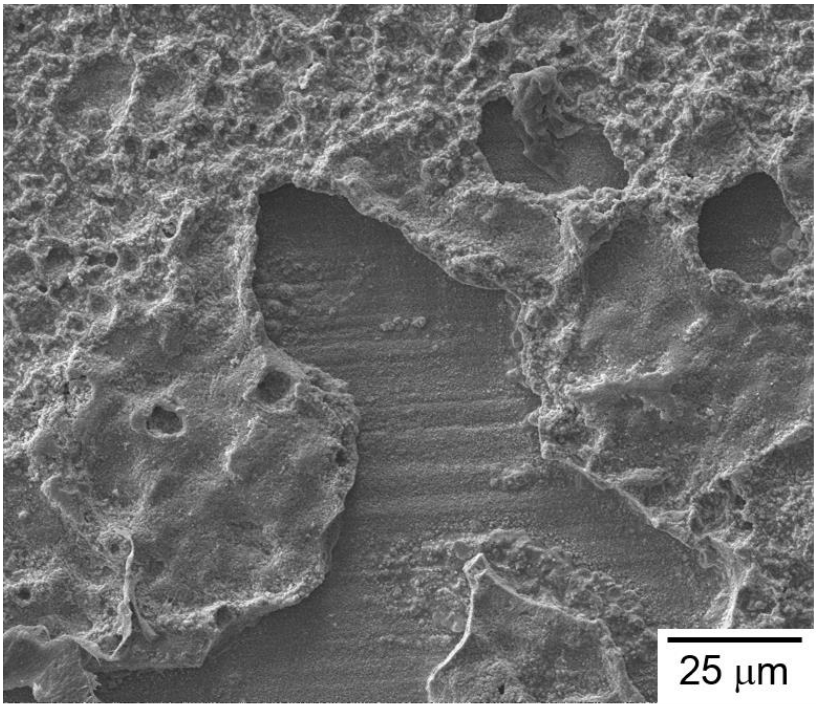

(c)

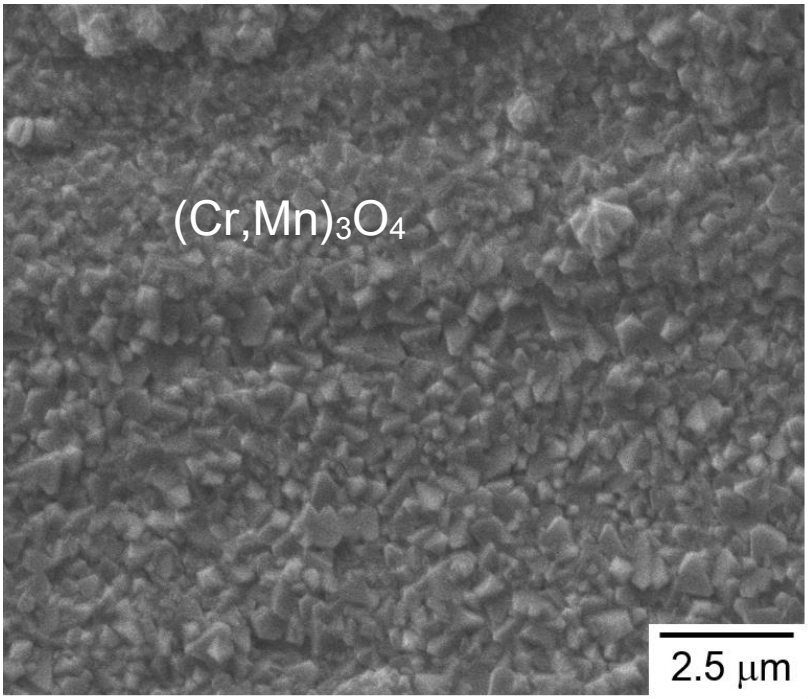

(d)

Fig. 19 (continued)

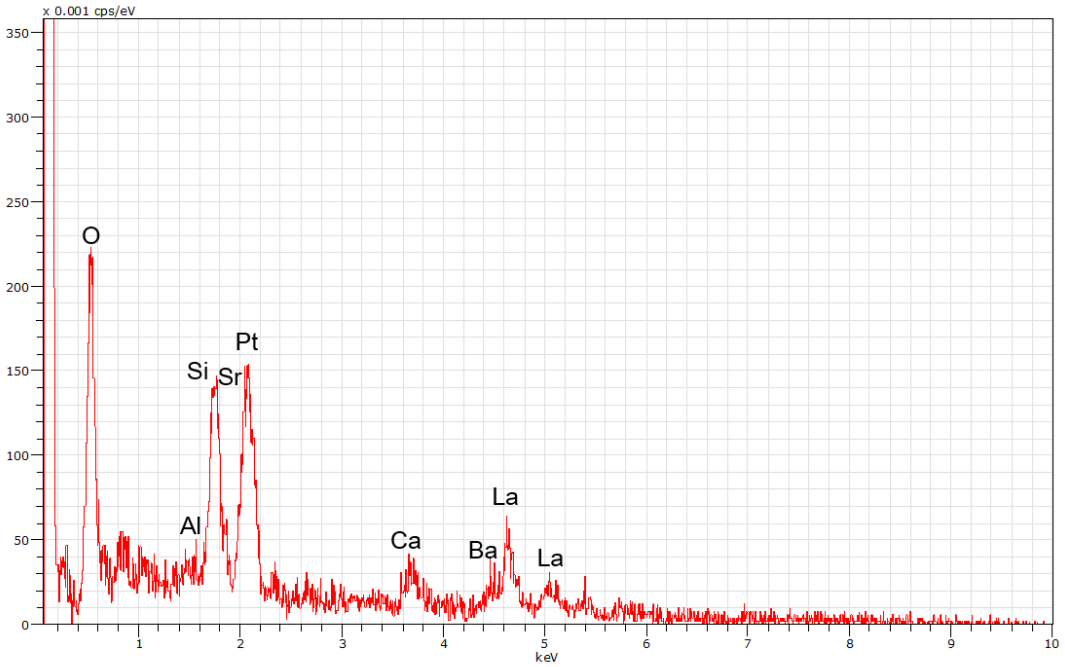

(a)

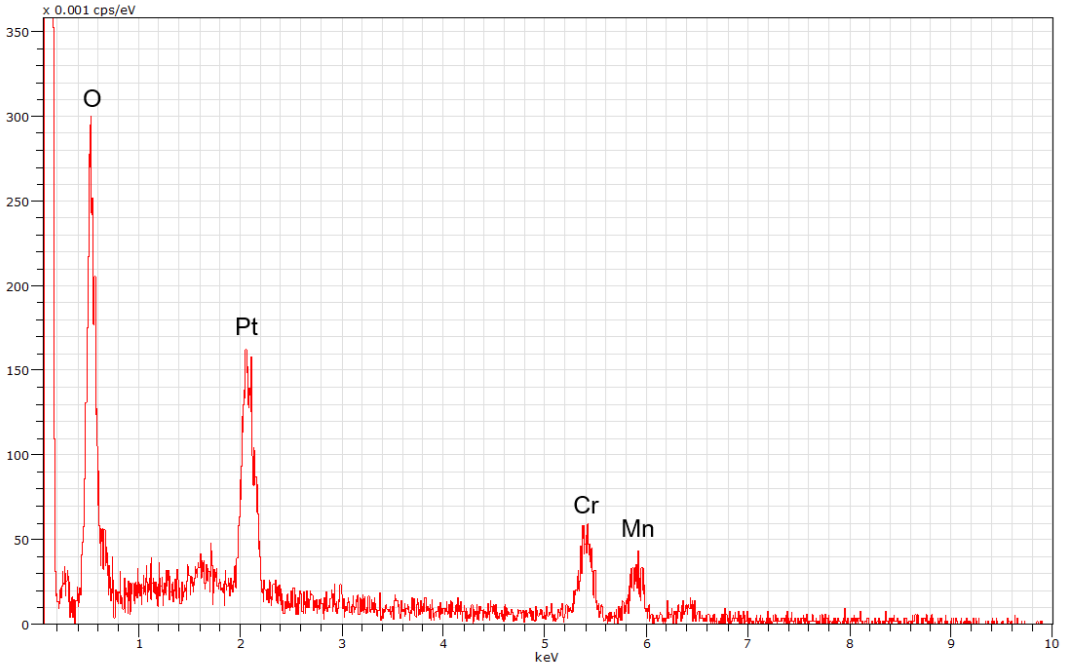

(b)

Fig. 20 EDS analysis results of the fracture surface of a non-aged tensile joint specimens: (a) Region 1 (in Fig. 19(b)); (b) Region 2 (in Fig. 19(d)).

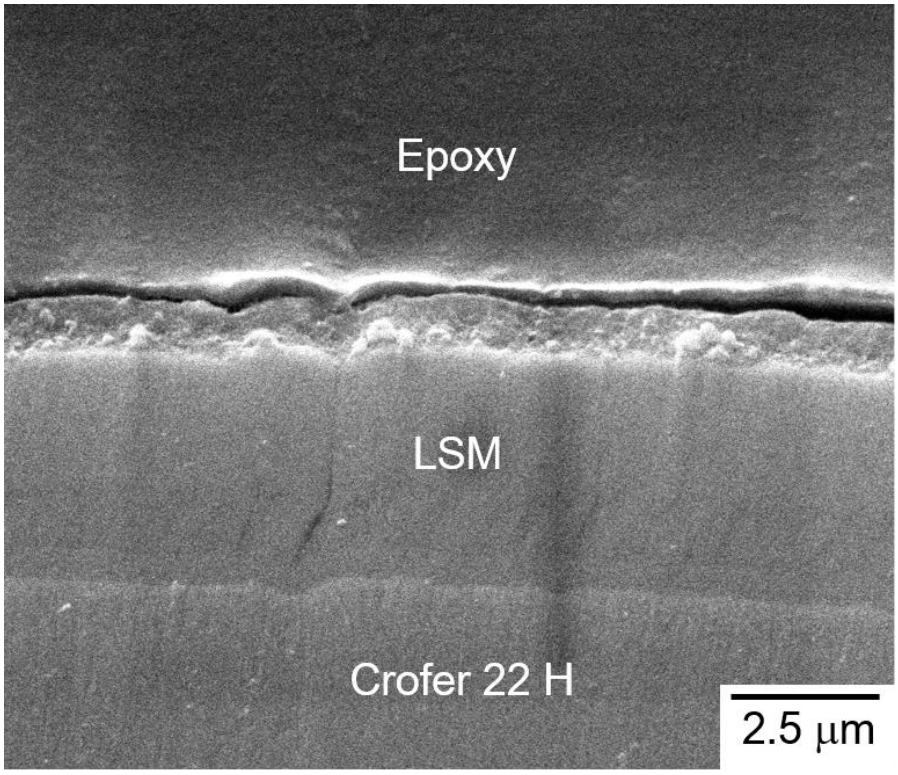

Fig. 21 Cross-sectional SEM micrograph of a non-aged tensile specimen before joining process.

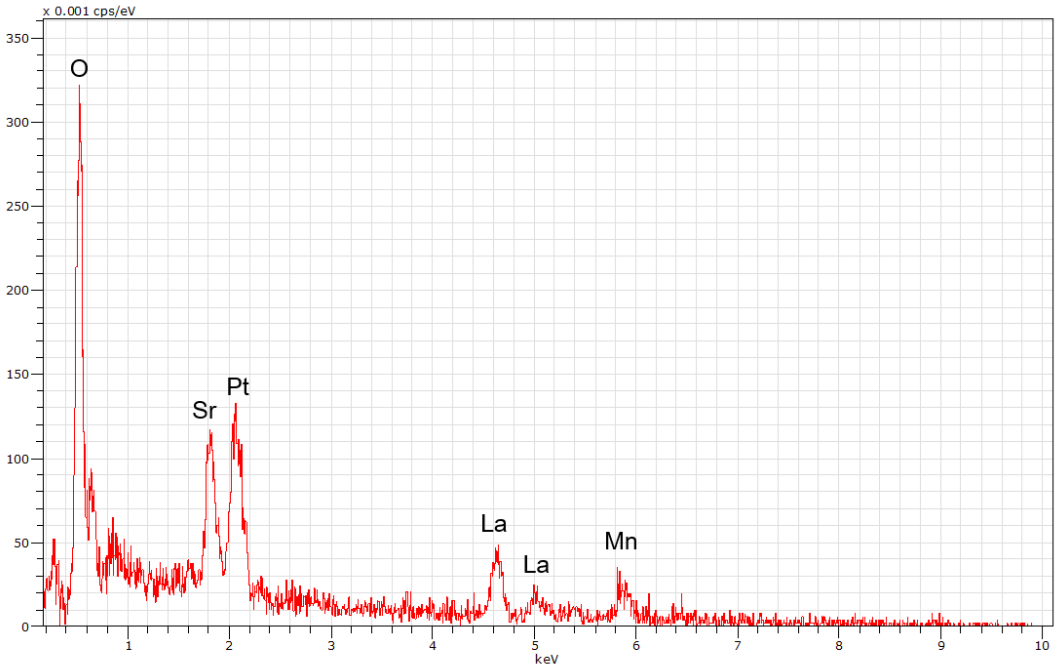

Fig. 22 EDS analysis result of the LSM coating observed in Fig. 21.

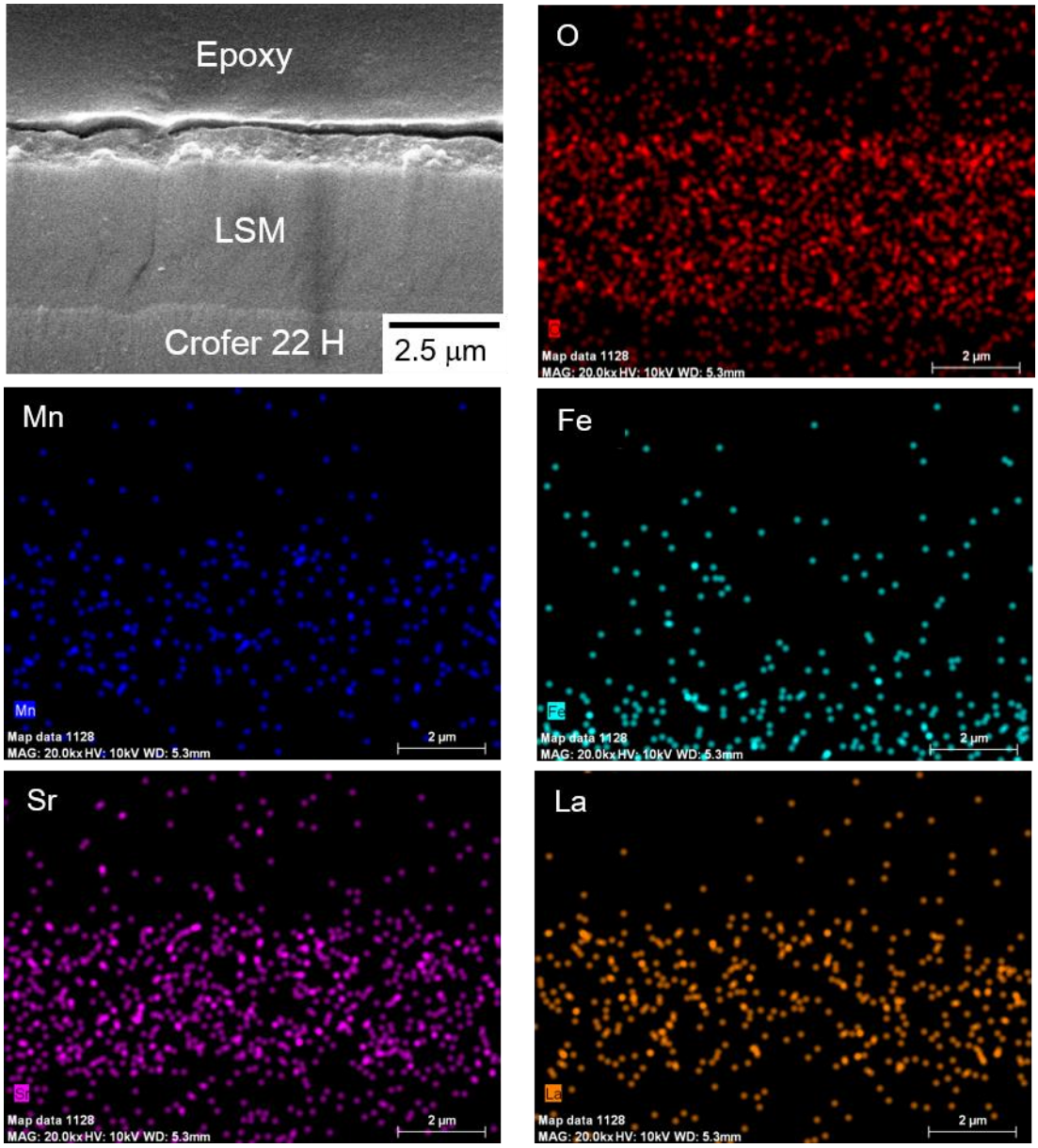

Fig. 23 EDS mapping of elements of Crofer 22 H and LSM in Fig. 21.

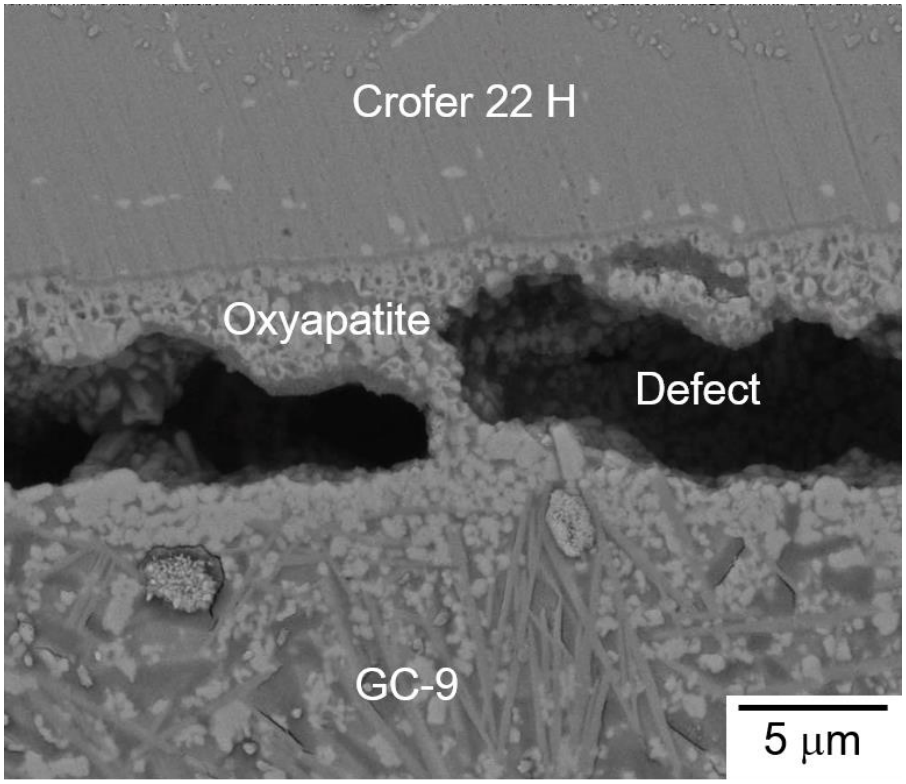

Fig. 24 Cross-sectional SEM micrograph (BSE mode) of an interface between the GC-9 and Crofer 22 H in a non-aged tensile specimen after joining process.

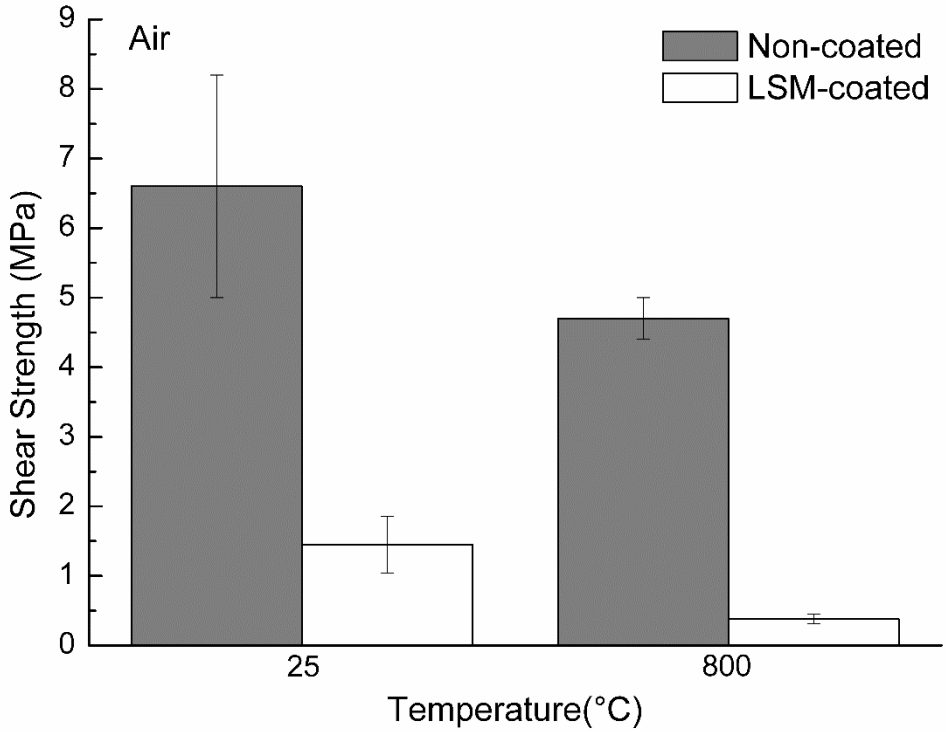

Fig. 25 Shear strength of non-coated and LSM-coated joint specimens tested in air at RT and 800 ℃.

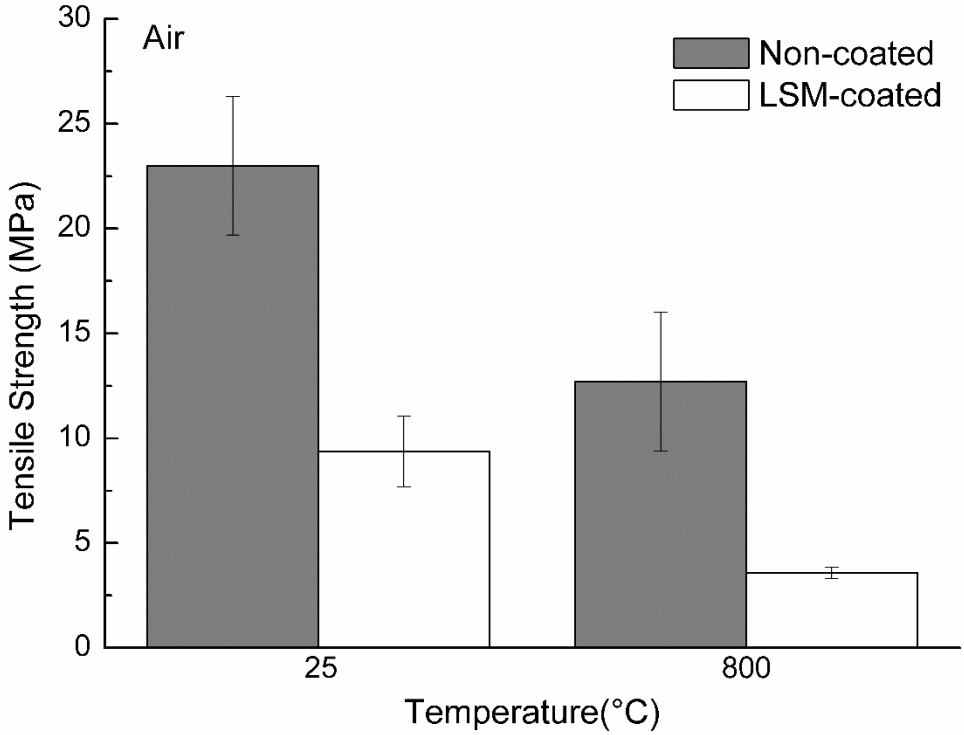

Fig. 26 Tensile strength of non-coated and LSM-coated joint specimens tested in air at RT and 800 ℃.

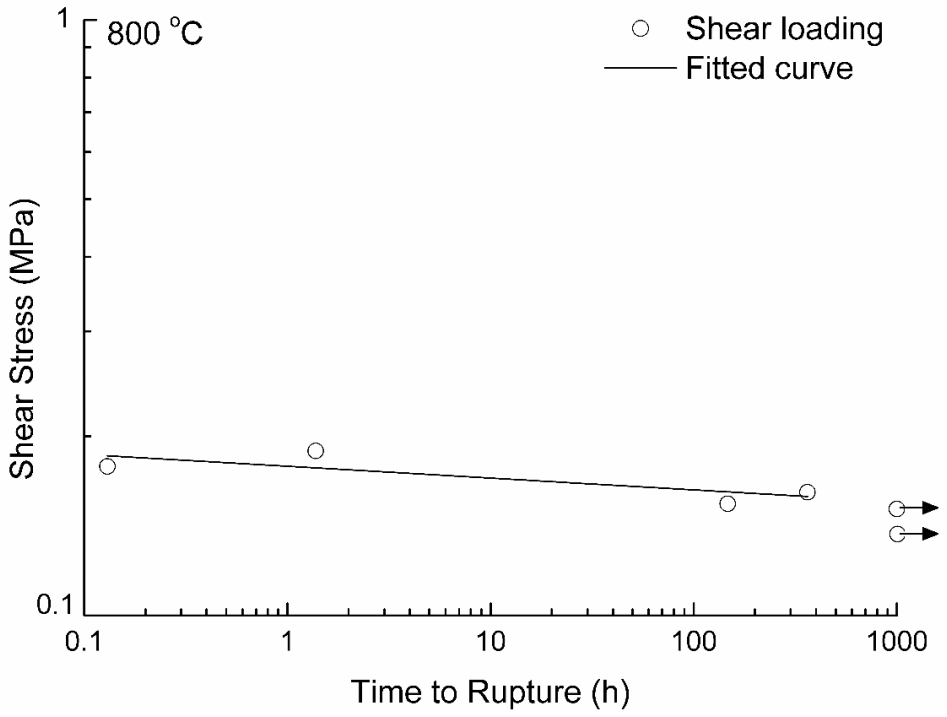

(a)

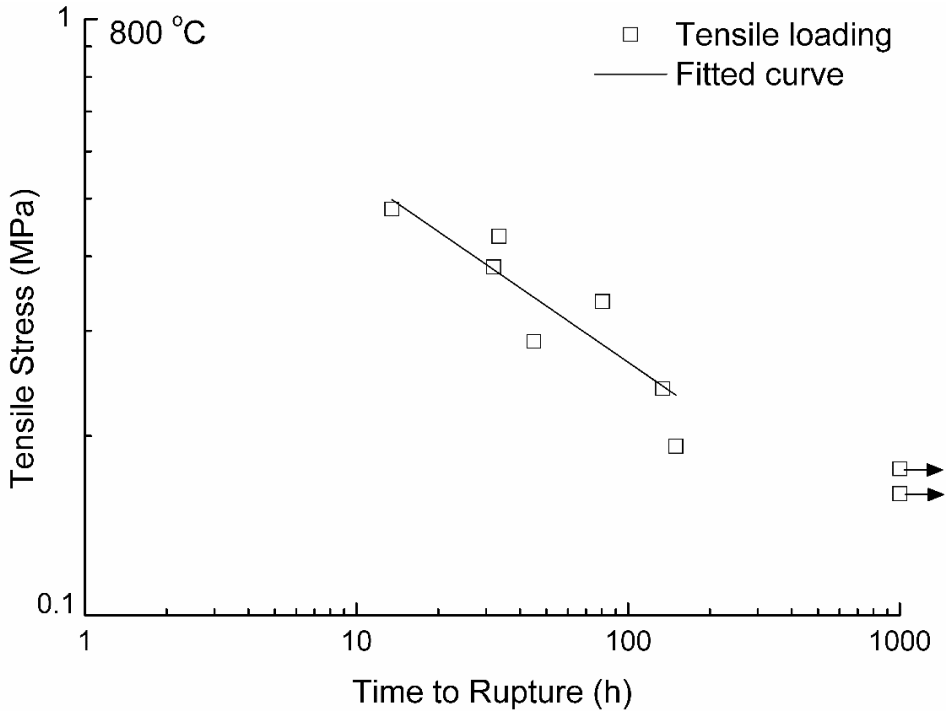

(b)

Fig. 27 Applied stress versus rupture time for non-aged joint specimens subjected to constant (a) shear and (b) tensile loading. (Arrow indicates the specimen was not ruptured when the test was terminated.)

(a)

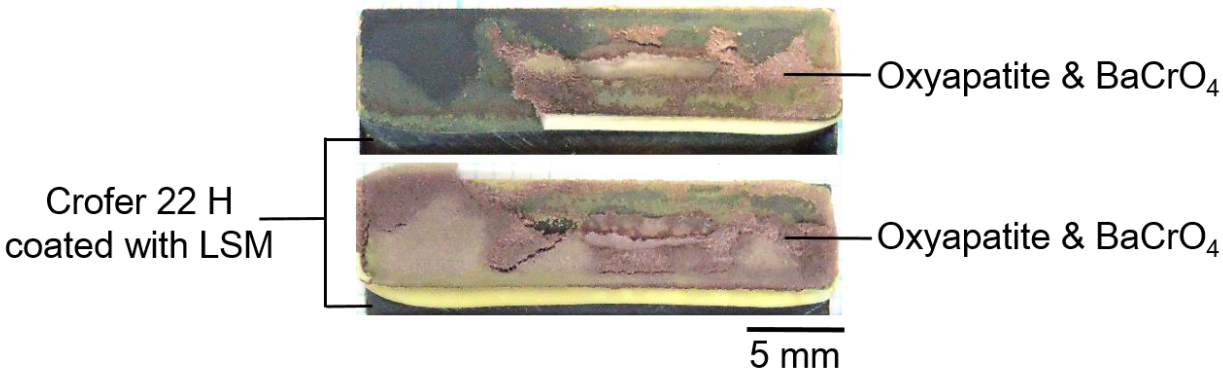

(b)

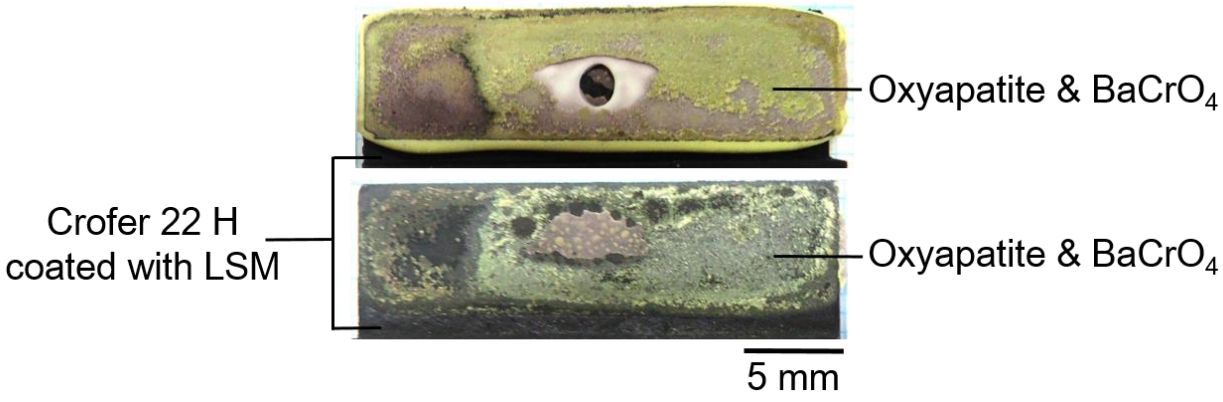

(c)

Fig. 28 Failure patterns in the non-aged shear specimens tested at 800 ℃ with various creep rupture times: (a) short creep rupture time; (b) medium-term creep rupture time; (c) long-term creep rupture time.

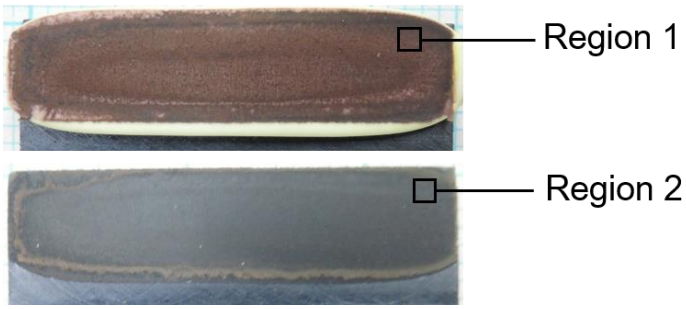

(a)

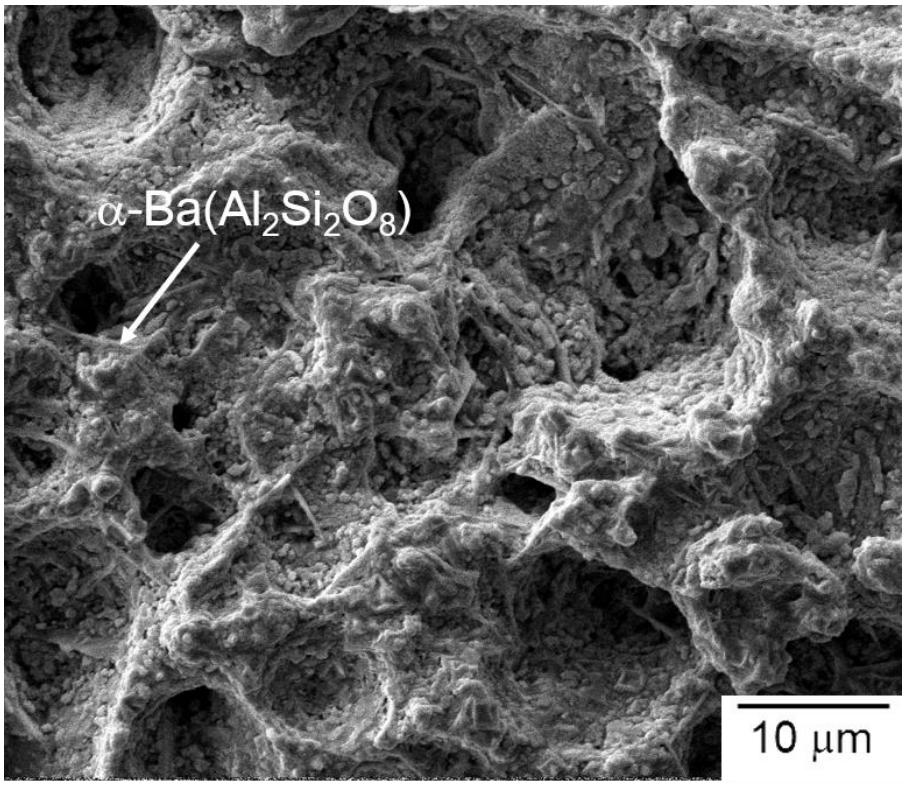

(b)

Fig. 29 Fracture surface of the non-aged shear specimen shown in Fig. 28(a): (a) optical micrograph showing the observed regions of SEM; (b) SEM micrograph of Region 1 (GC-9 side); (c) SEM micrograph of Region 2 (metal side).

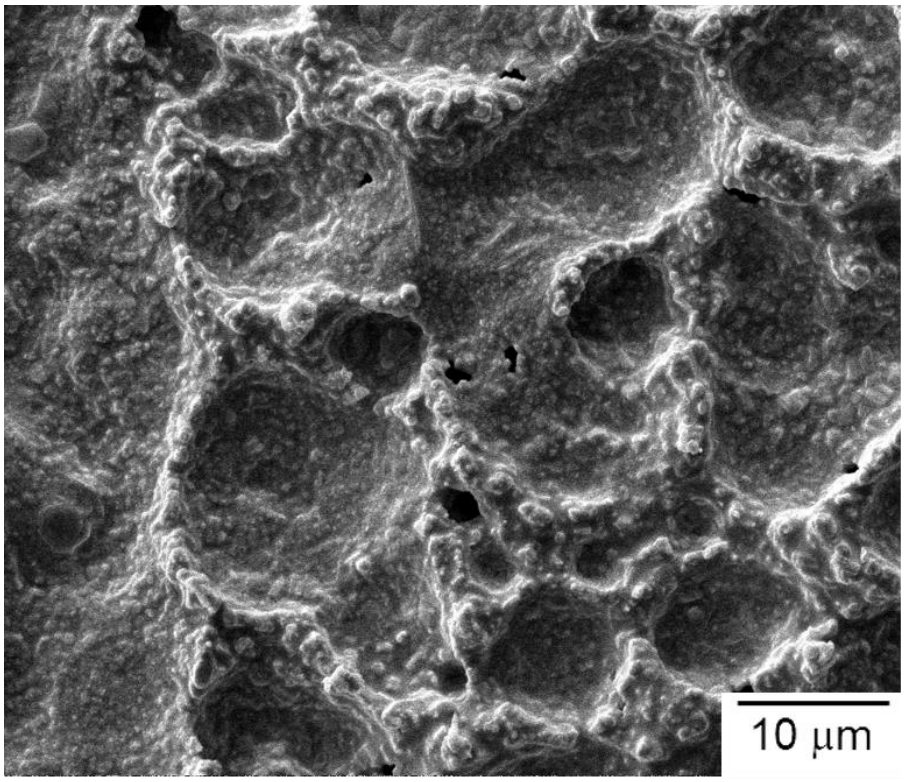

(c)

Fig. 29 (continued)

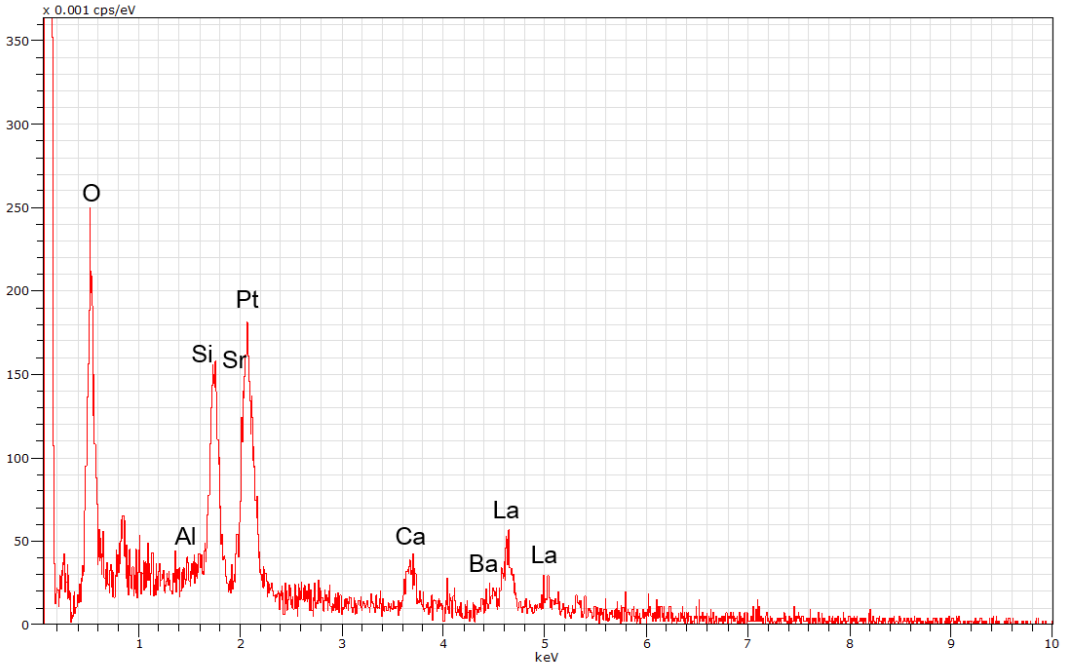

(a)

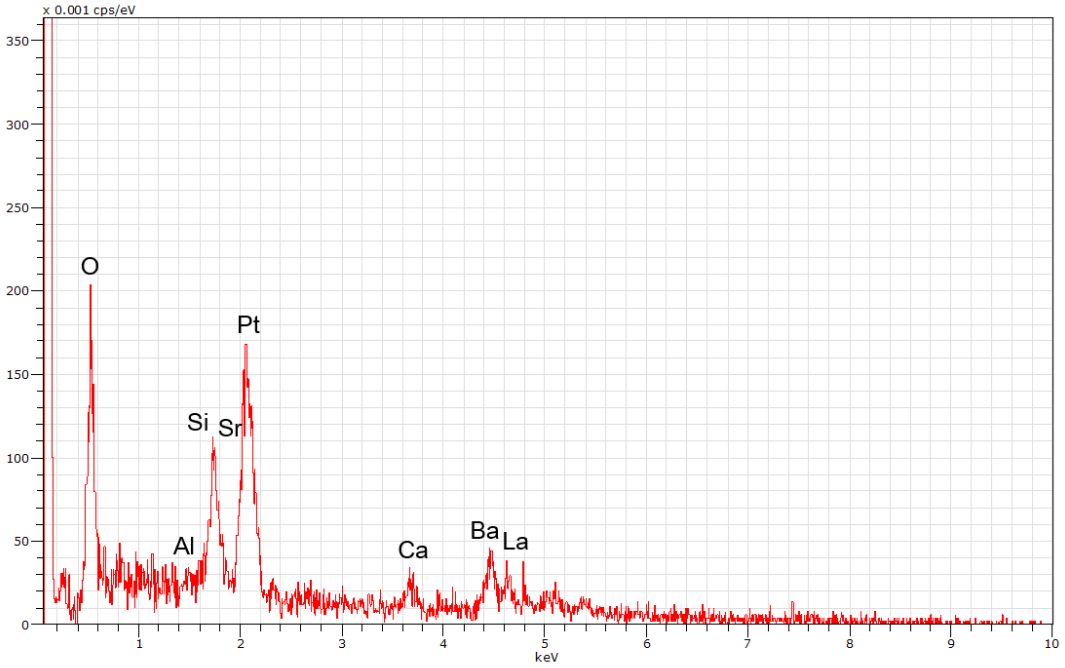

(b)

Fig. 30 EDS analysis results of the fracture surface of a non-aged shear joint specimen: (a) Region 1 (in Fig. 29(b)); (b) Region 2 (in Fig. 29(c)).

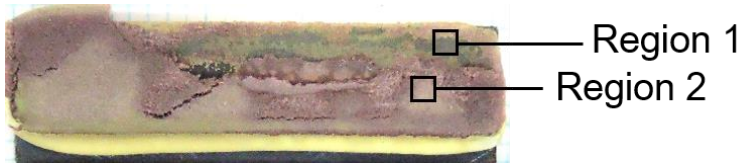

(a)

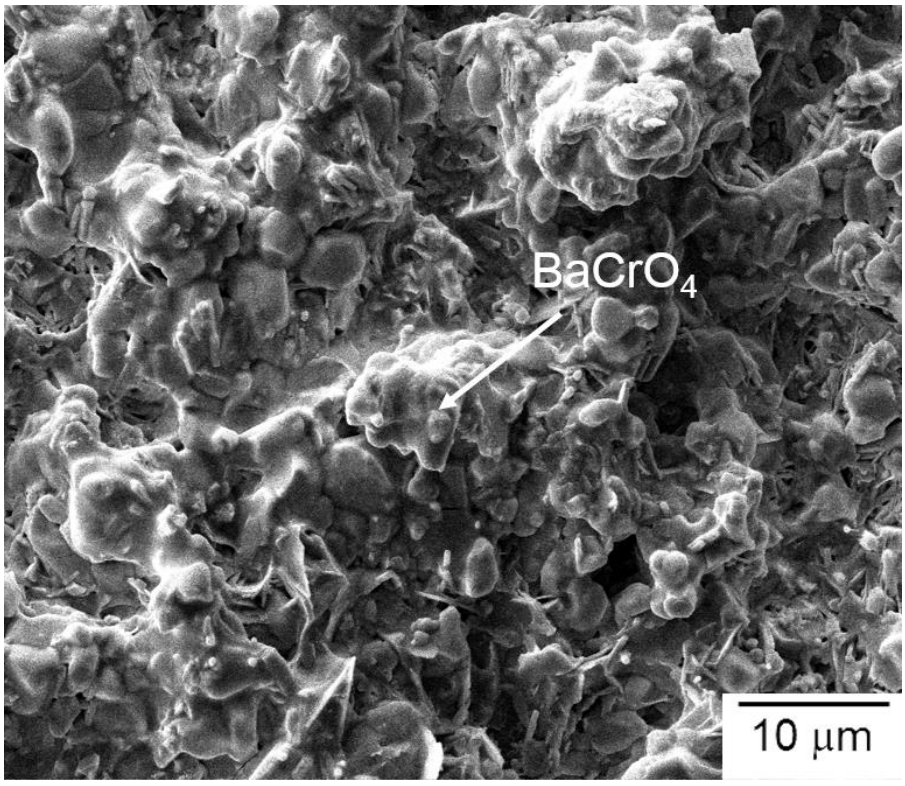

(b)

Fig. 31 Fracture surface of the non-aged shear specimen shown in the lower part of Fig. 28(b): (a) optical micrograph showing the observed regions of SEM; (b) SEM micrograph of Region 1 (GC-9 side); (c) SEM micrograph of Region 2 (metal side).

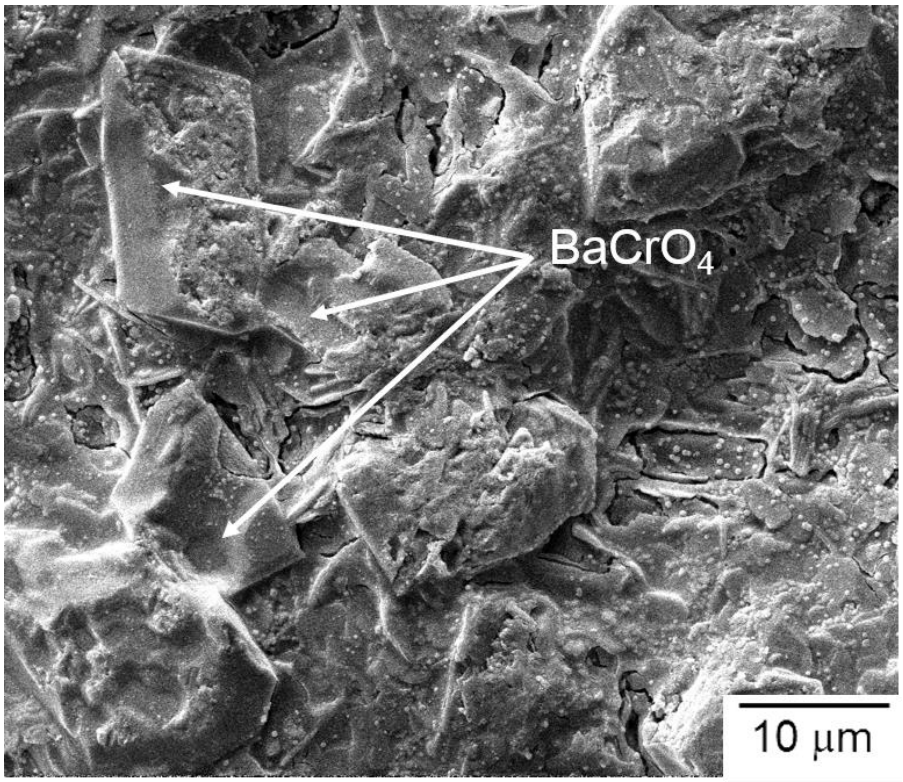

(c)

Fig. 31 (continued)

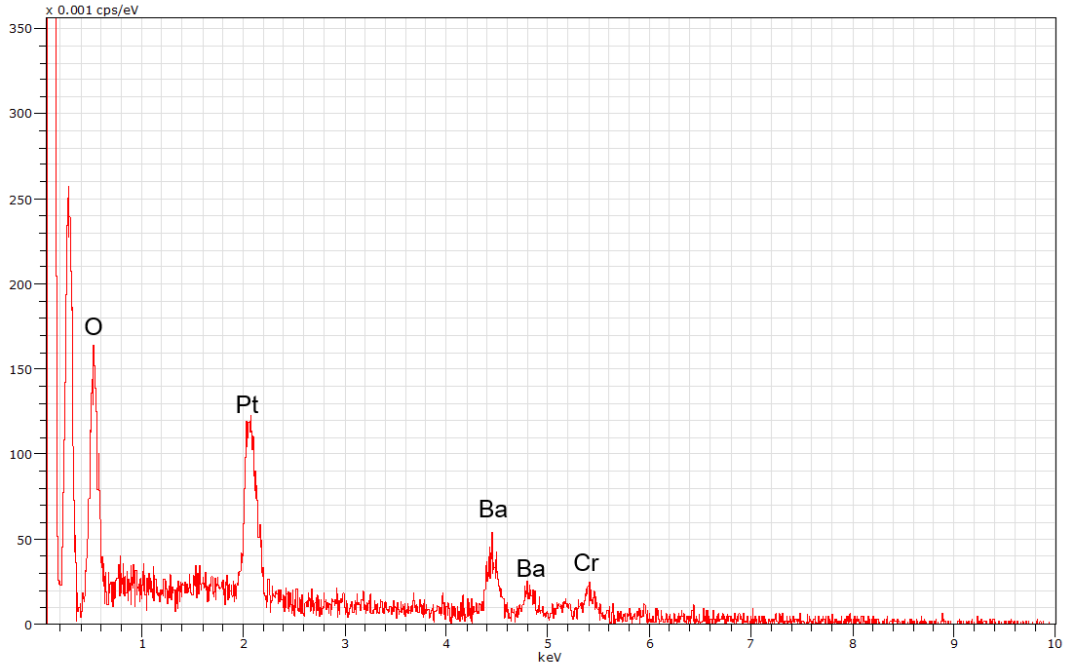

(a)

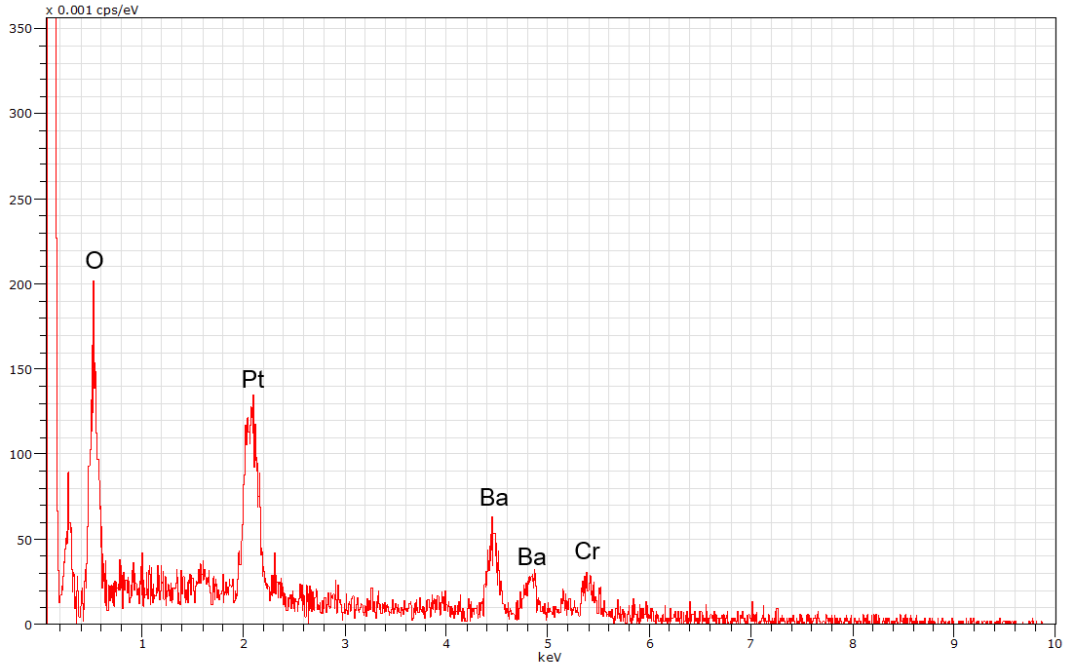

(b)

Fig. 32 EDS analysis results of the fracture surface of a non-aged shear joint specimen: (a) $BaCrO_4$ chromate in Region 1 (in Fig. 31(b)); (b) $BaCrO_4$ chromate in Region 2 (in Fig. 31(c)).

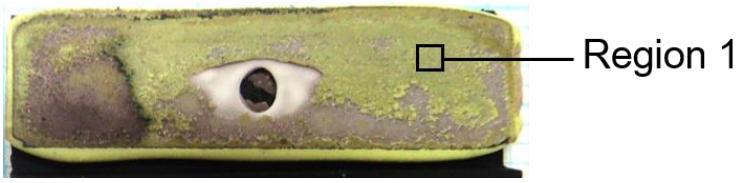

(a)

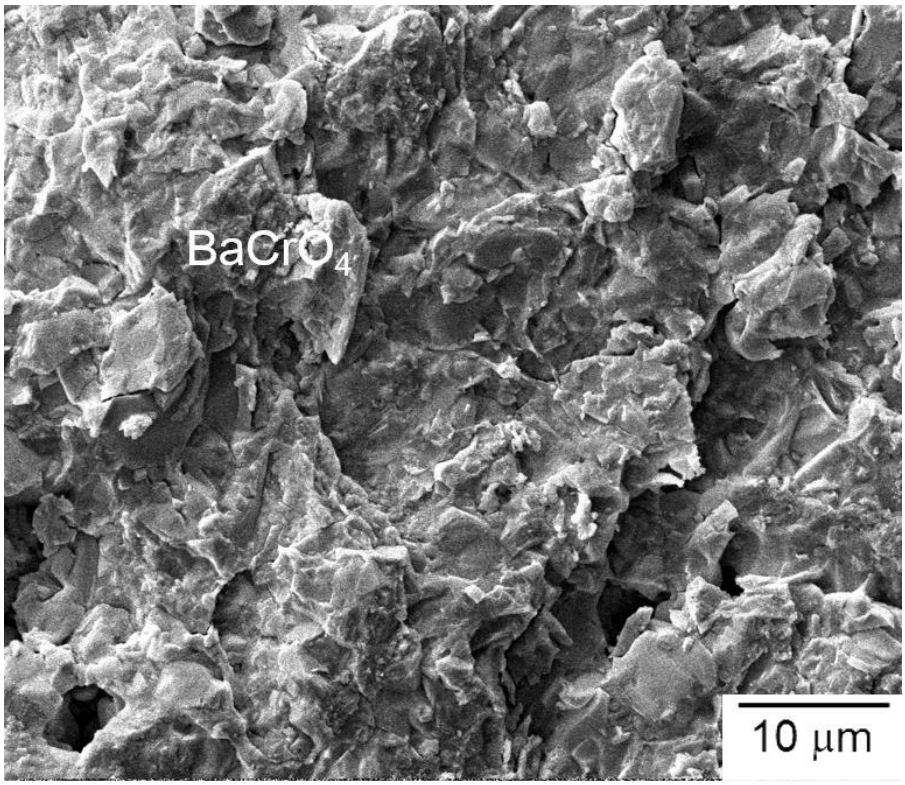

(b)

Fig. 33 Fracture surface of the non-aged shear specimen shown in the upper part of Fig. 28(c): (a) optical micrograph showing the observed region of SEM; (b) SEM micrograph of Region 1 (GC-9 side).

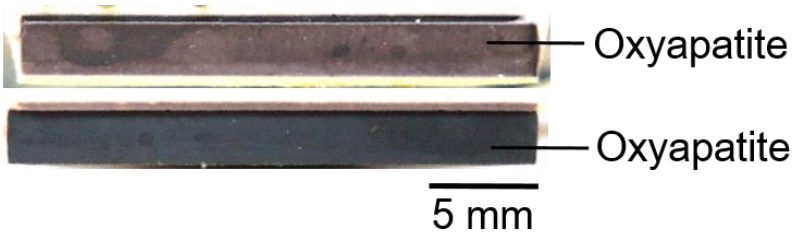

(a)

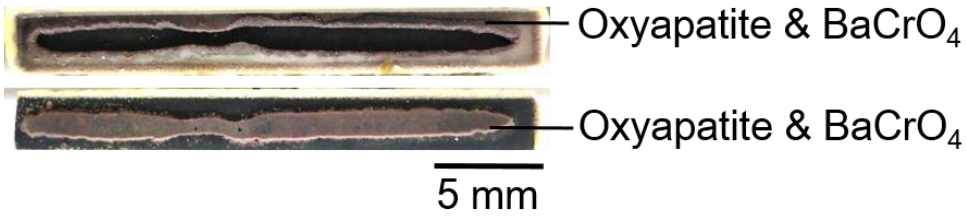

(b)

Fig. 34 Failure patterns in the non-aged tensile specimens tested at 800 ℃ with various creep rupture times: (a) short creep rupture time; (b) medium-term creep rupture time.

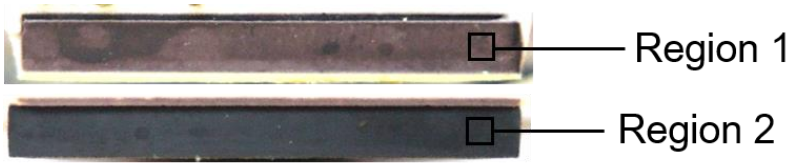

(a)

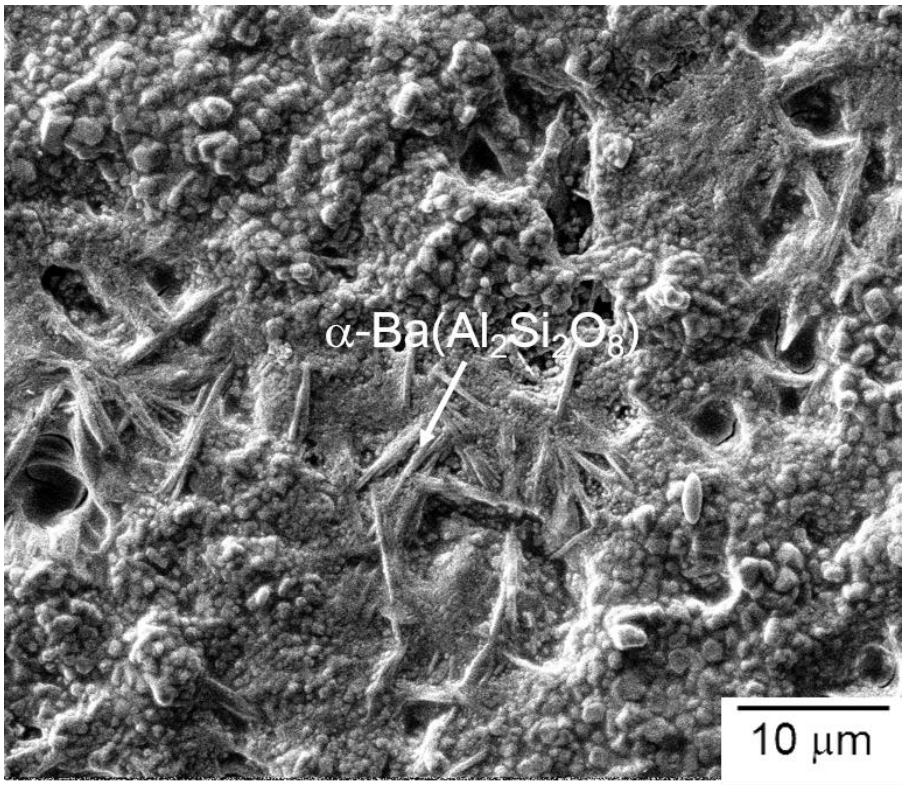

(b)

Fig. 35 Fracture surface of the non-aged tensile specimen shown in Fig. 34(a): (a) optical micrograph showing the observed regions of SEM; (b) SEM micrograph of Region 1 (GC-9 side); (c) SEM micrograph of Region 2 (metal side); (d) high-magnification view of spinel layer in Region 2.

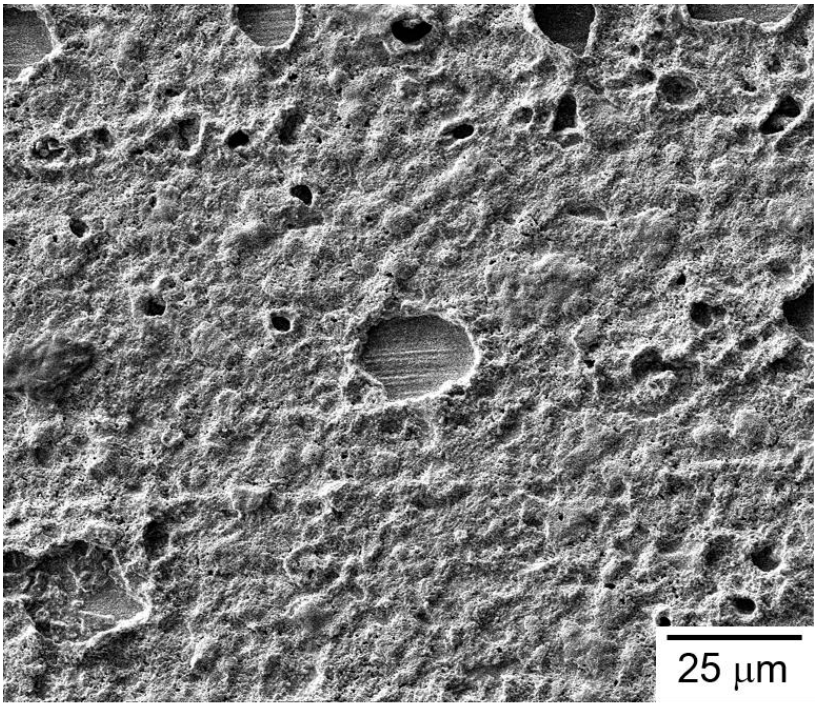

(c)

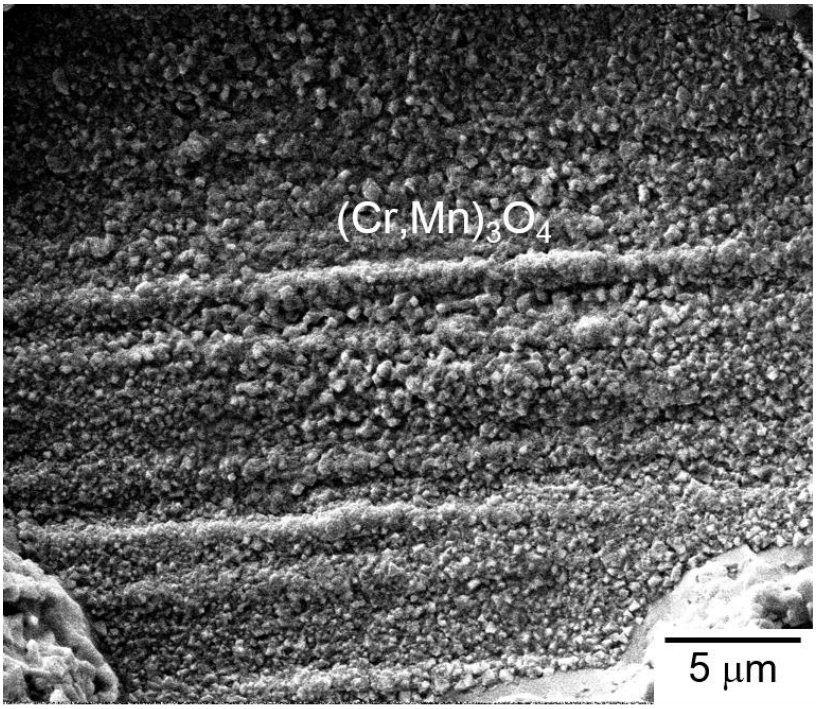

(d)

Fig. 35 (continued)

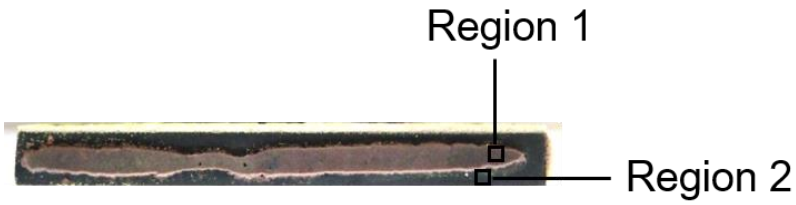

(a)

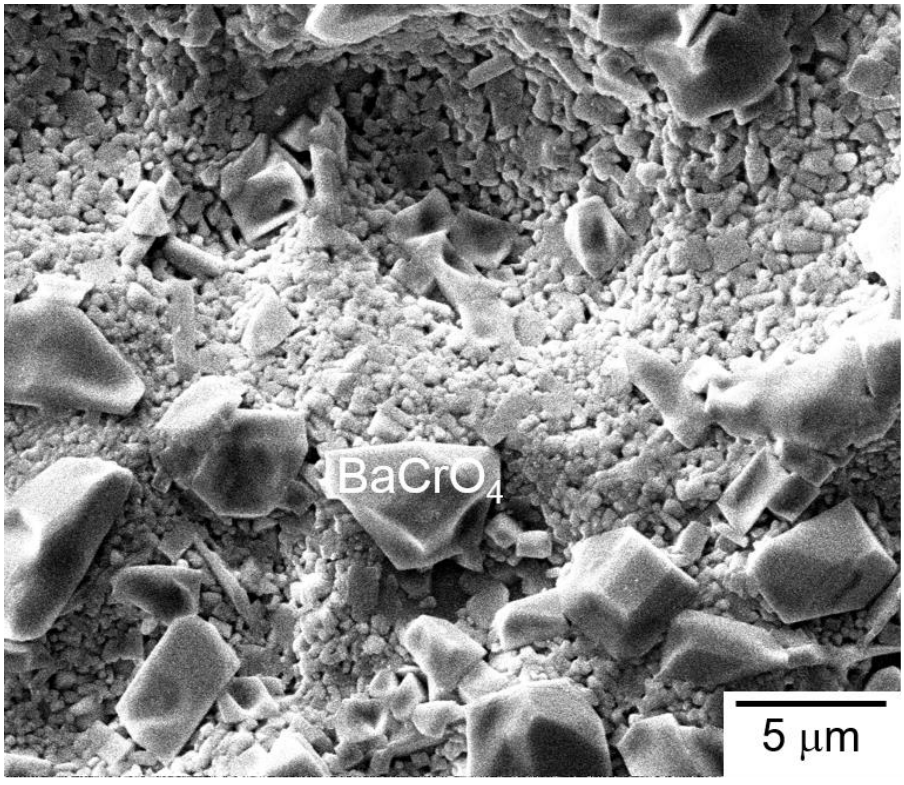

(b)

Fig. 36 Fracture surface of the non-aged tensile specimen shown in the lower part of Fig. 34(b): (a) optical micrograph showing the observed regions of SEM; (b) SEM micrograph of Region 1 (GC-9 side); (c) SEM micrograph of Region 2 (metal side).

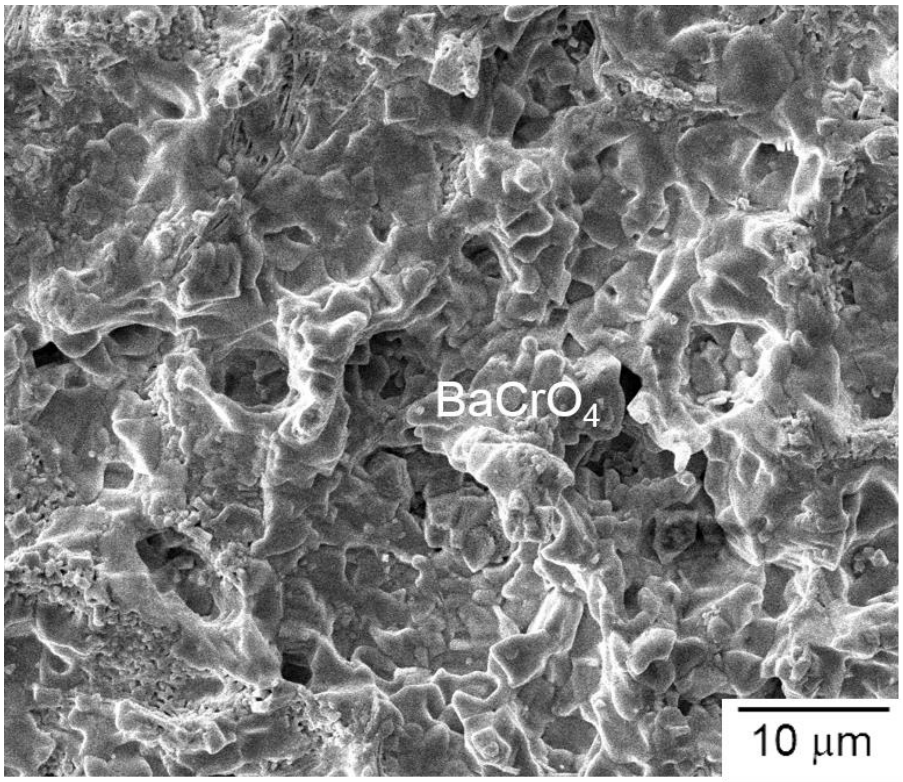

(c)

Fig. 36 (continued)

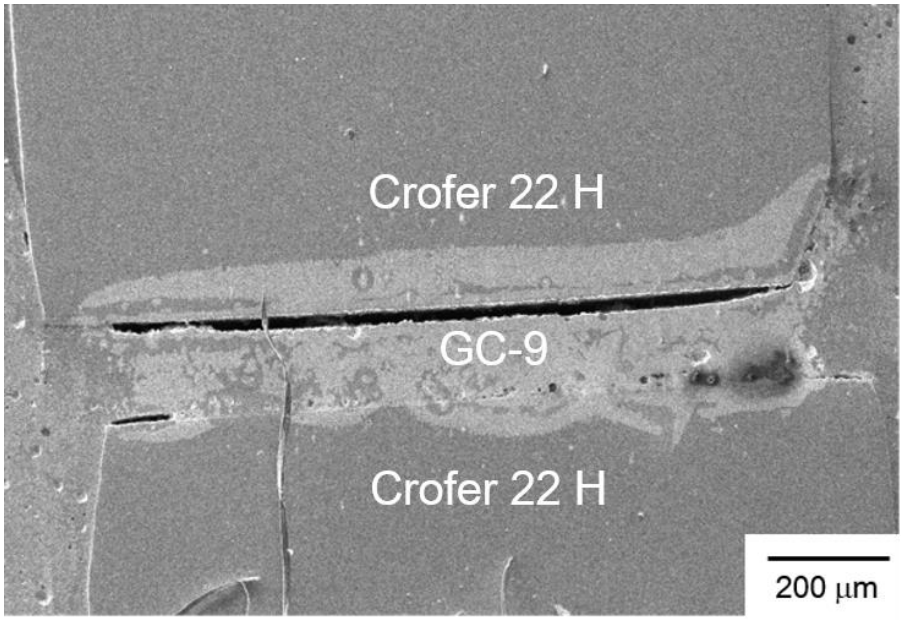

(a)

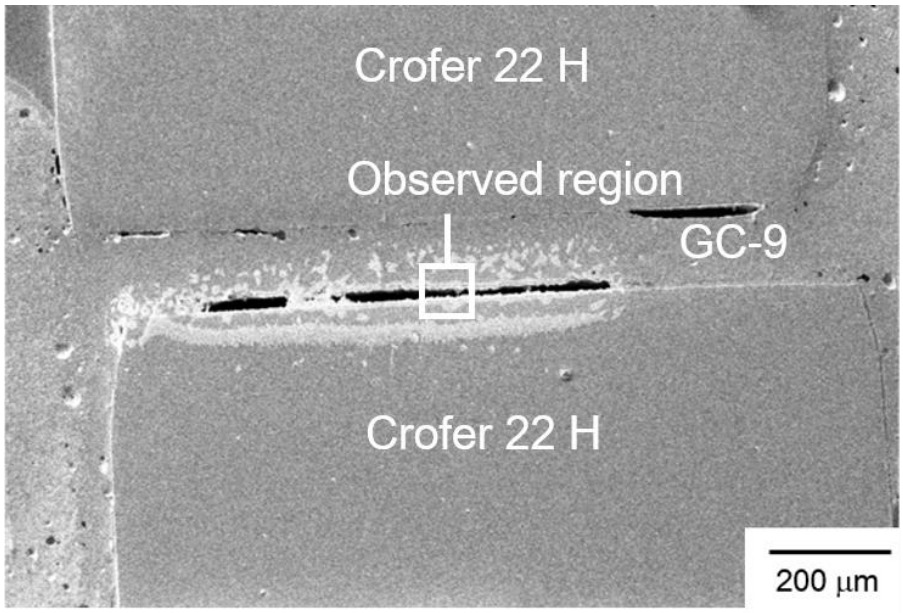

(b)

Fig. 37 Cross-sectional SEM micrographs of the interface between the GC-9 and Crofer 22 H in a non-ruptured, runout tensile specimen with a creep rupture time over 1000 h: (a) low magnification view; (b) another low-magnification view; (c) high- magnification (BSE mode) of the outlined region in (b); (d) higher magnification (BSE mode) of the outlined region in (c).

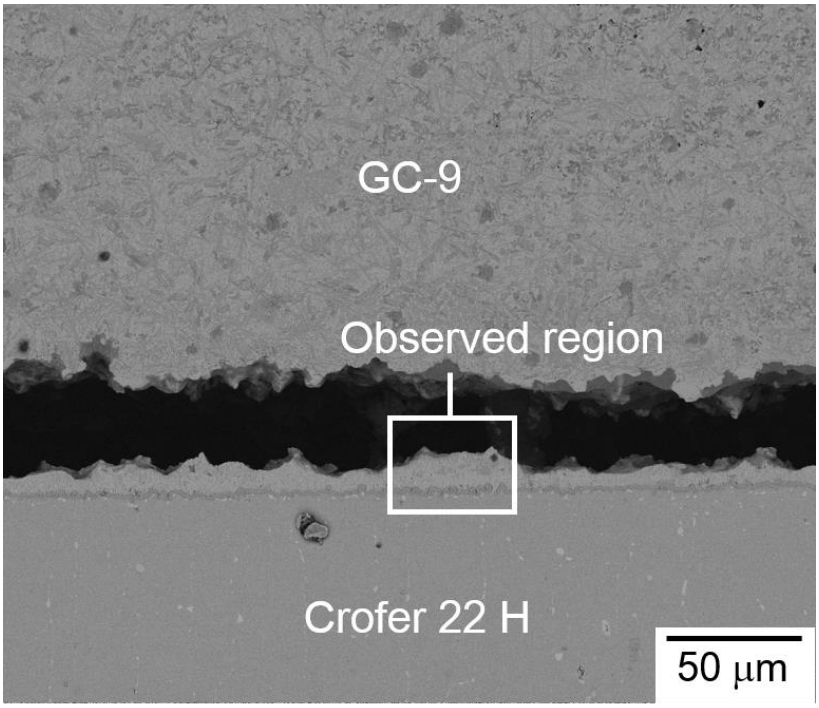

(c)

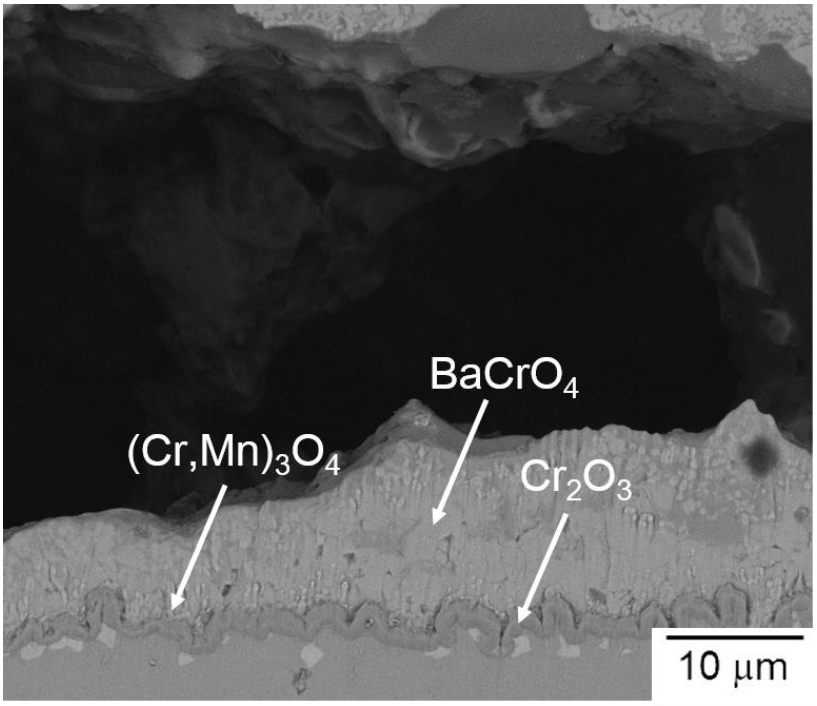

(d)

Fig. 37 (continued)

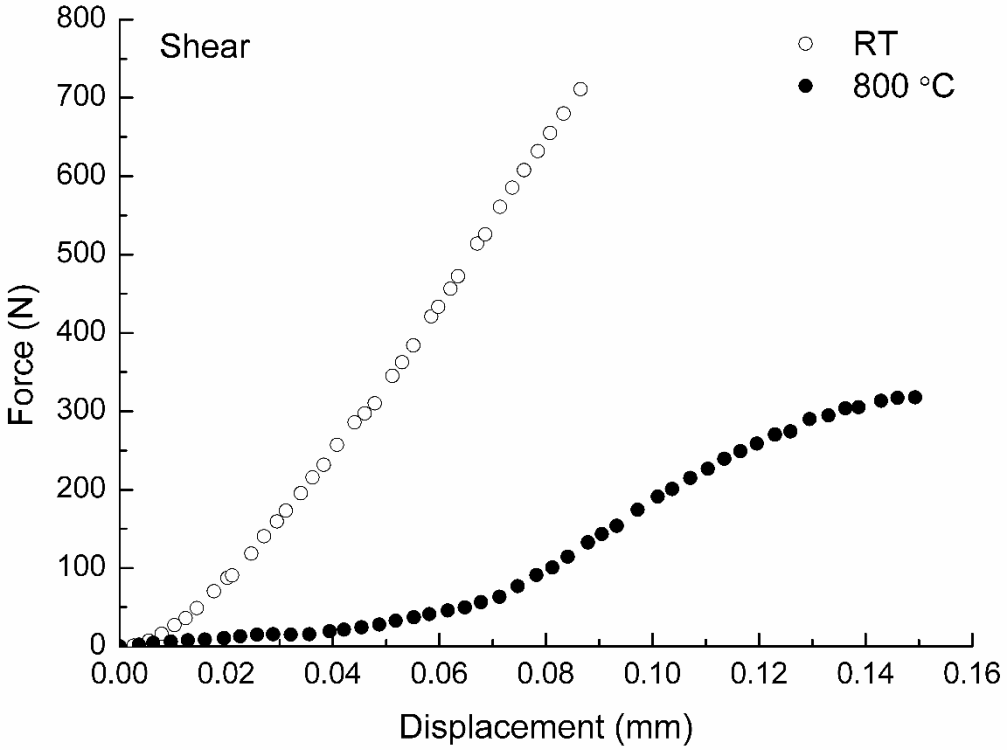

Fig. 38 Typical force-displacement curves of the 1000 h-aged joint specimens tested under shear loading in air at RT and 800 ℃.

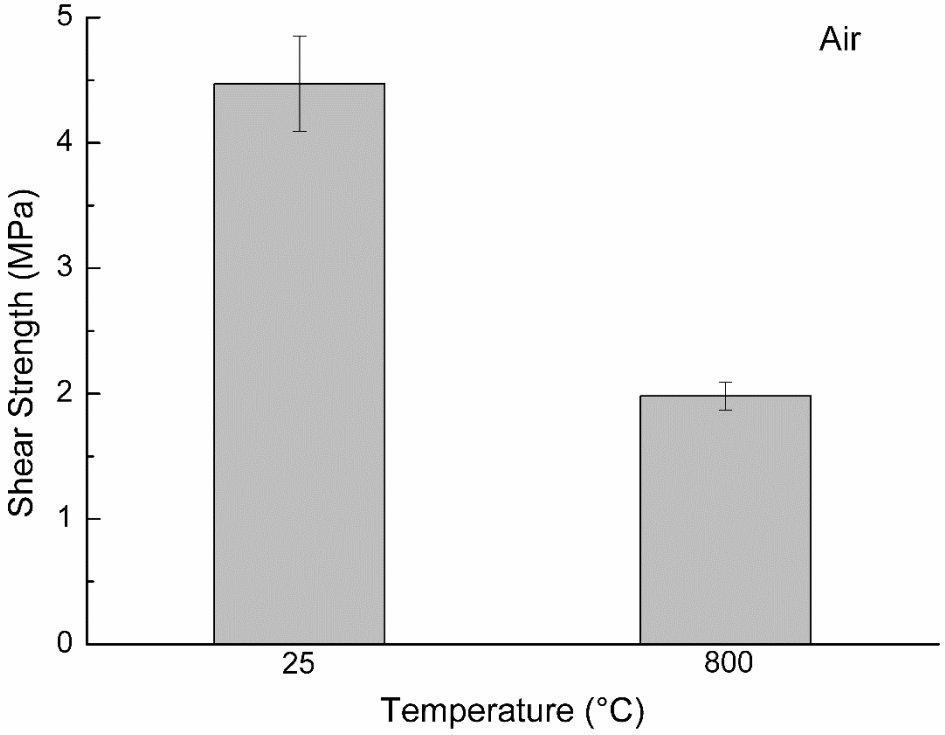

Fig. 39 Shear strength of 1000 h-aged joint specimens tested in air at RT and 800 ℃.

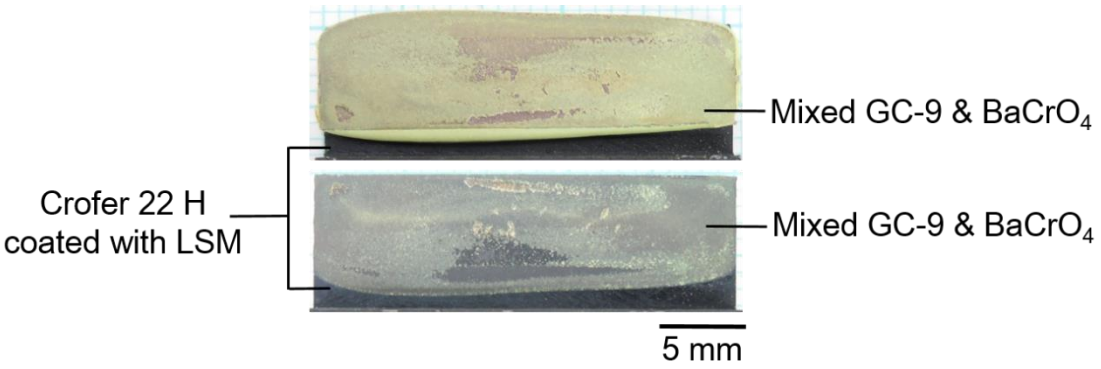

(a)

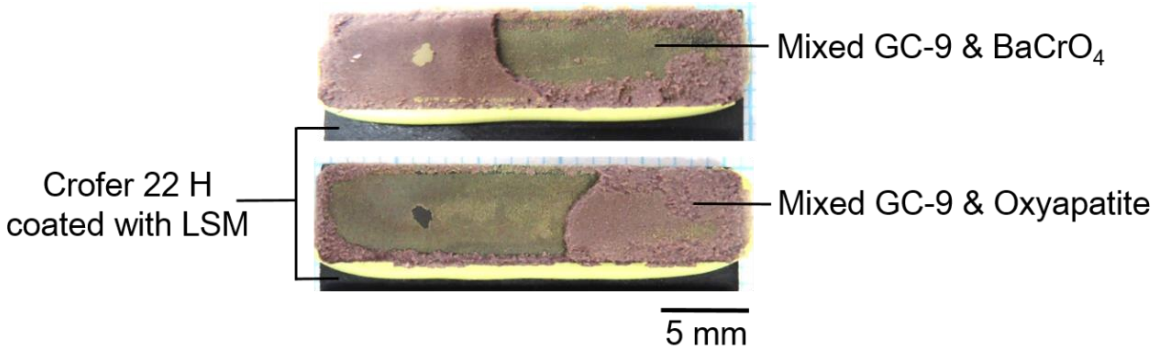

(b)

Fig. 40 Failure patterns of 1000 h-aged shear specimens tested in air at (a) RT and (b) 800 ℃.

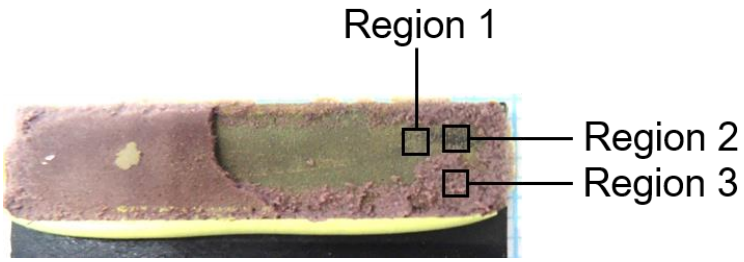

(a)

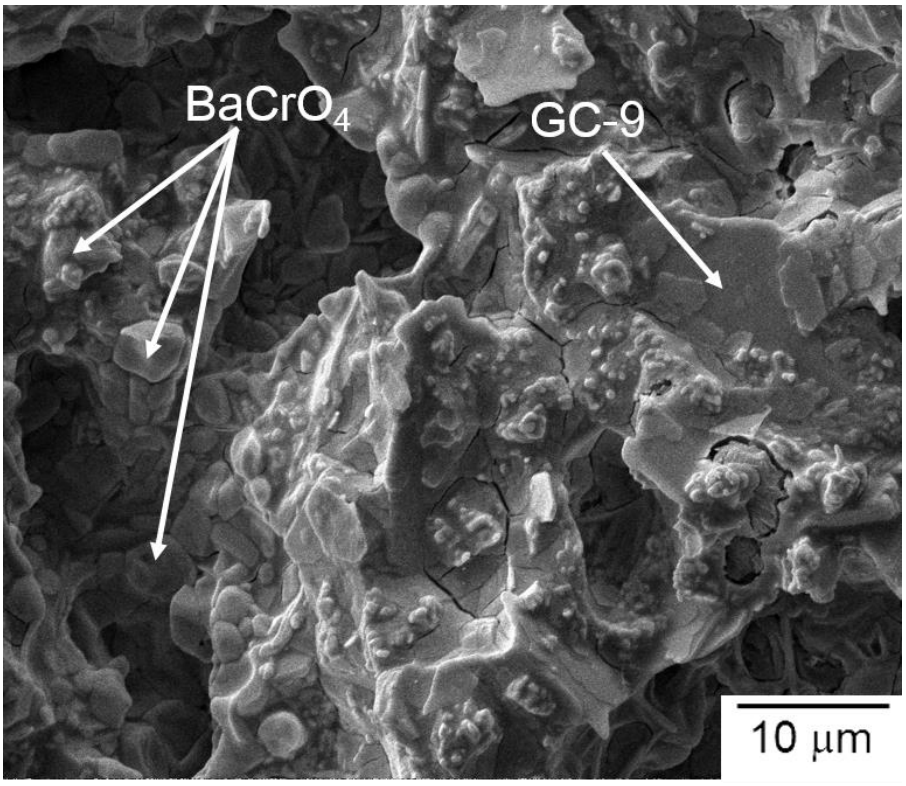

(b)

Fig. 41 Fracture surface of the 1000 h-aged shear specimen shown in Fig. 40(b): (a) optical micrograph showing the observed regions of SEM; (b) SEM micrograph of Region 1; (c) SEM micrograph of Region 2; (d) SEM micrograph of Region 3.

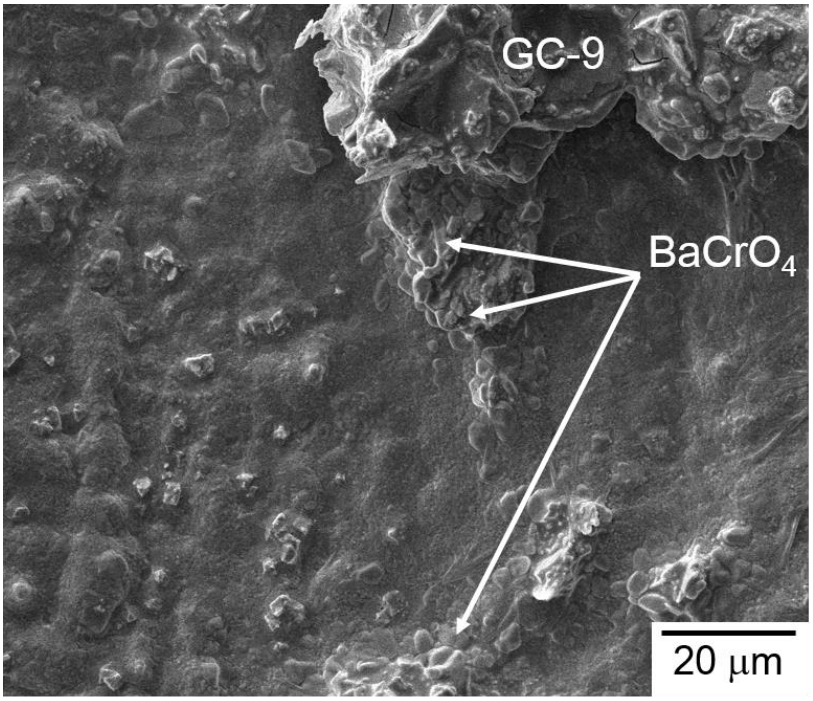

(c)

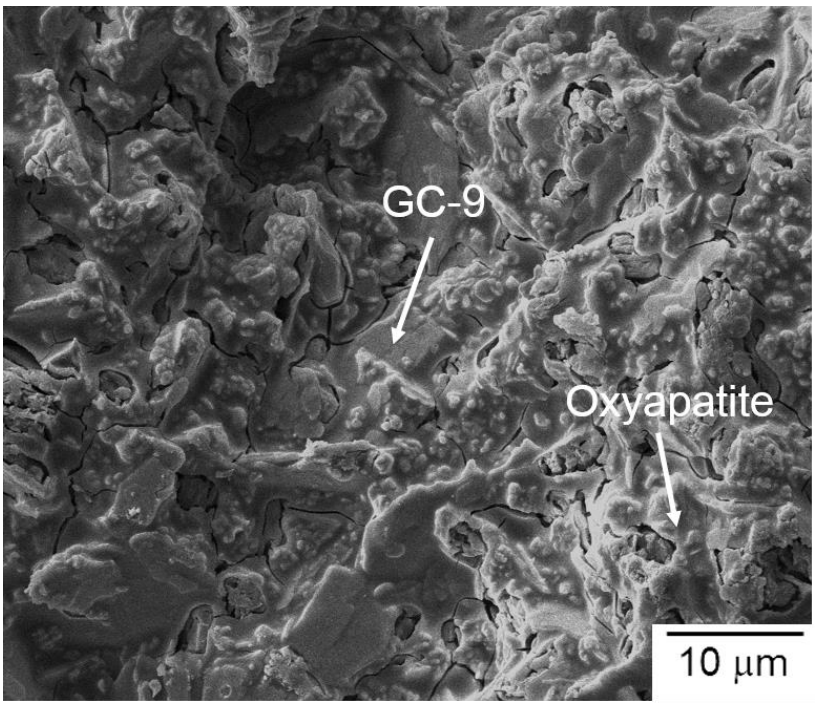

(d)

Fig. 41 (continued)

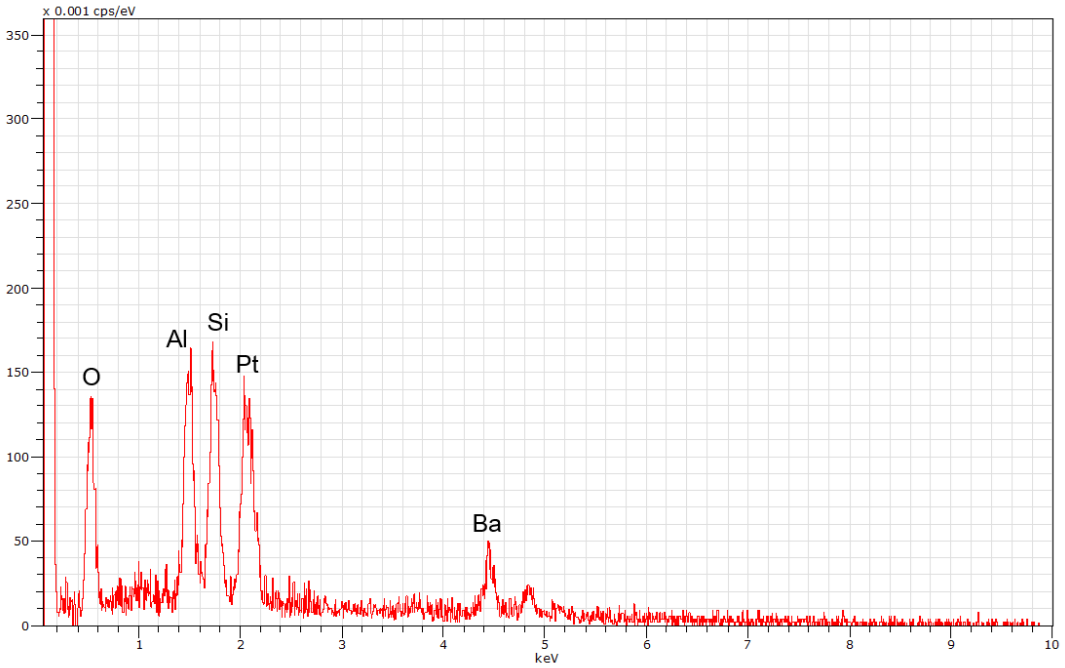

Fig. 42 EDS analysis results of the fracture surface of a 1000 h-aged shear joint specimen shown in Fig. 41(b).

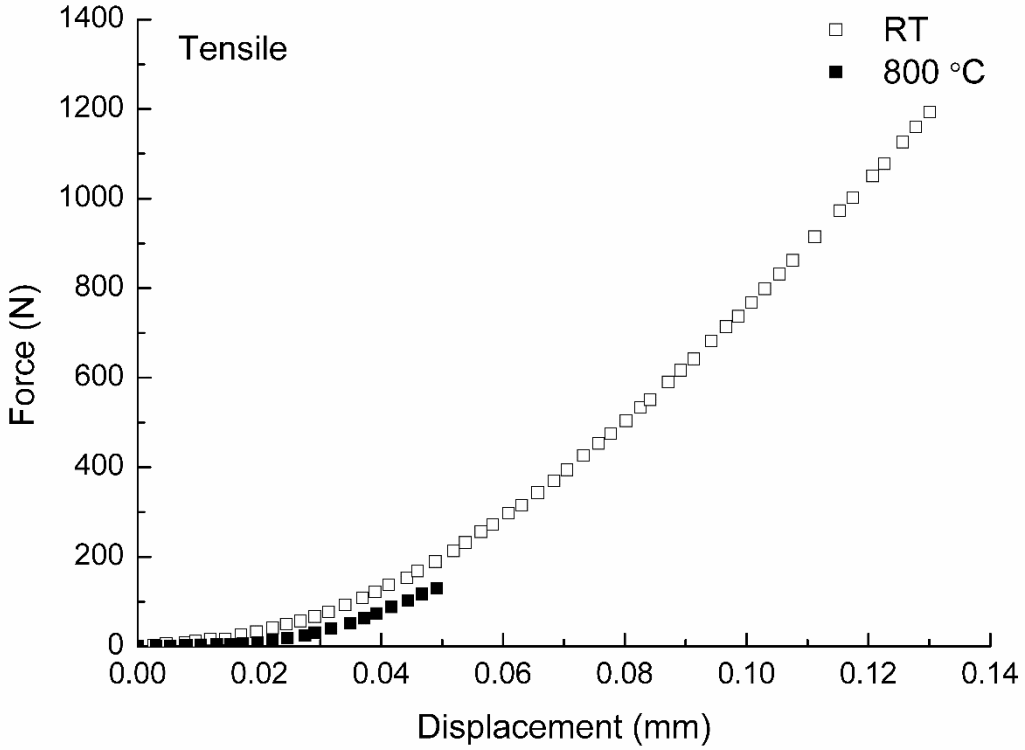

Fig. 43 Typical force-displacement curves of the 1000 h-aged joint specimens tested under tensile loading in air at RT and 800 ℃.

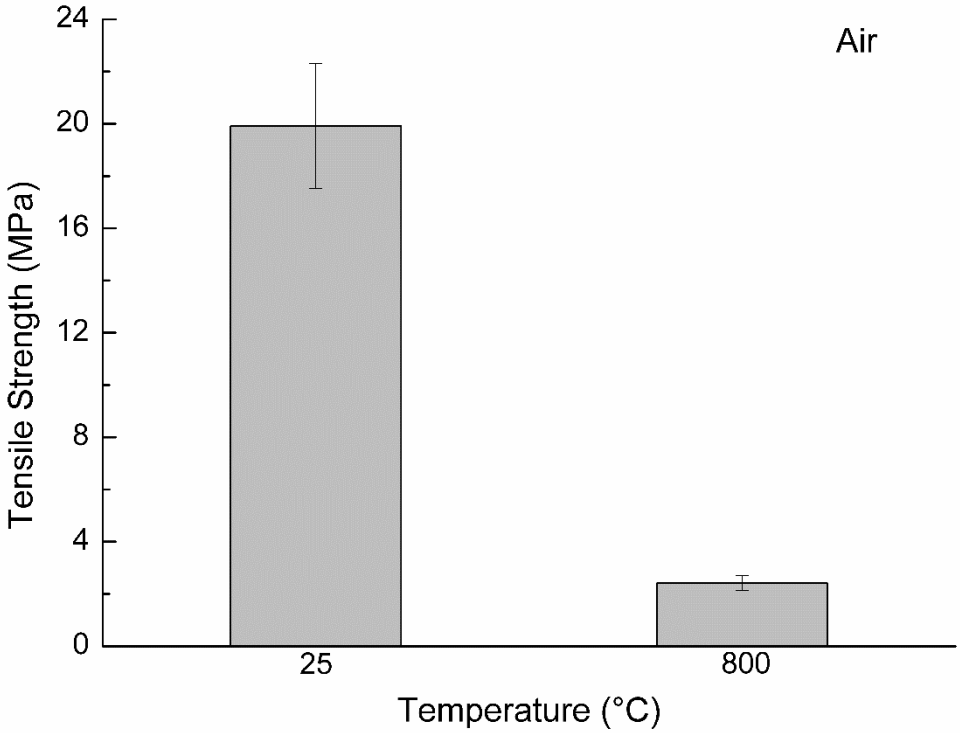

Fig. 44 Tensile strength of 1000 h-aged joint specimens tested in air at RT and 800 ℃.

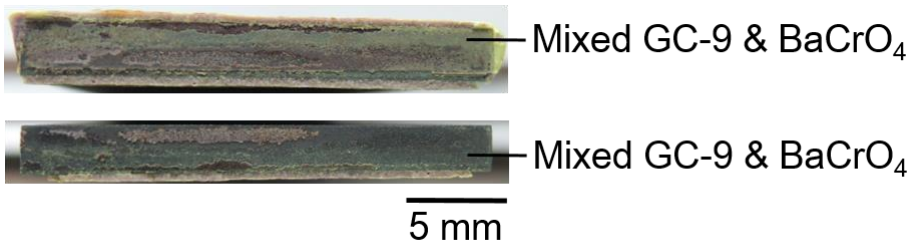

(a)

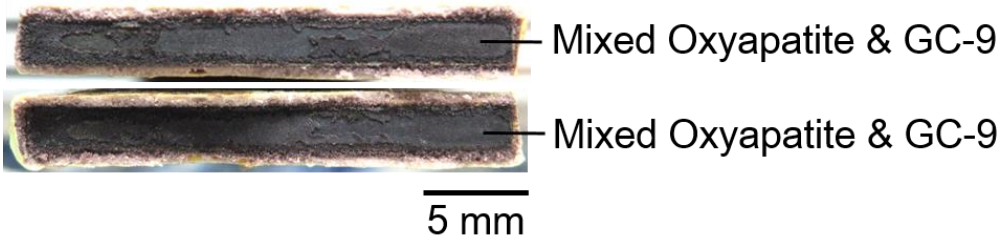

(b)

Fig. 45 Failure patterns of 1000 h-aged tensile specimens tested in air at (a) RT and (b) 800 ℃.

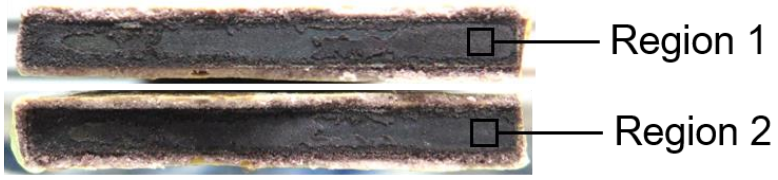

(a)

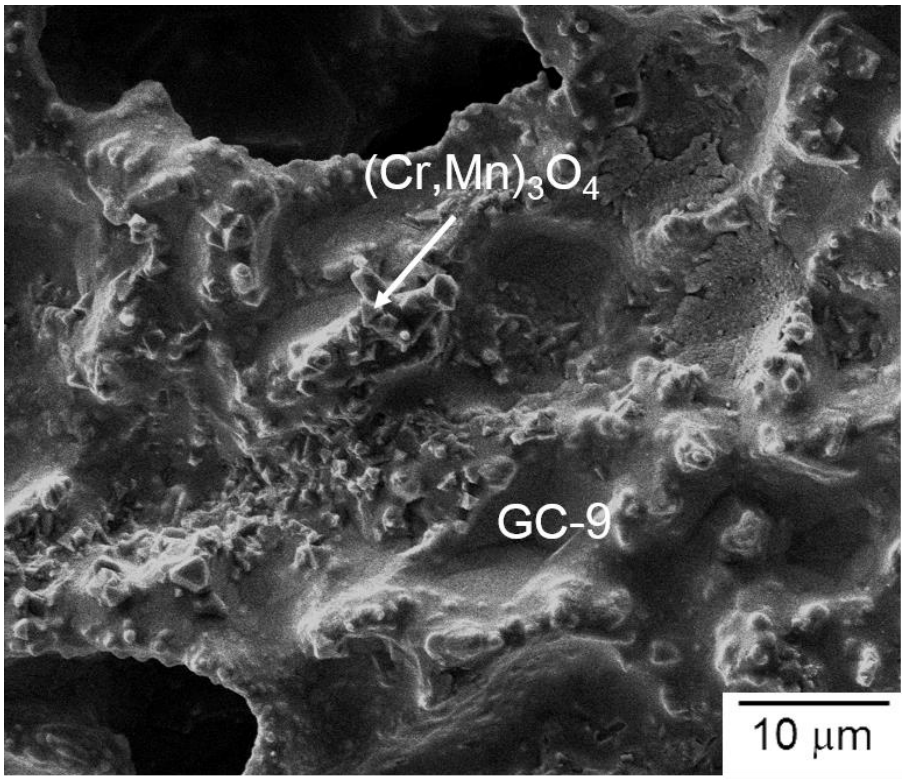

(b)

Fig. 46 Fracture surface of the 1000 h-aged tensile specimen shown in Fig. 45(b): (a) optical micrographs showing the observed regions of SEM; (b) SEM micrograph of Region 1; (c) SEM micrograph of Region 2.

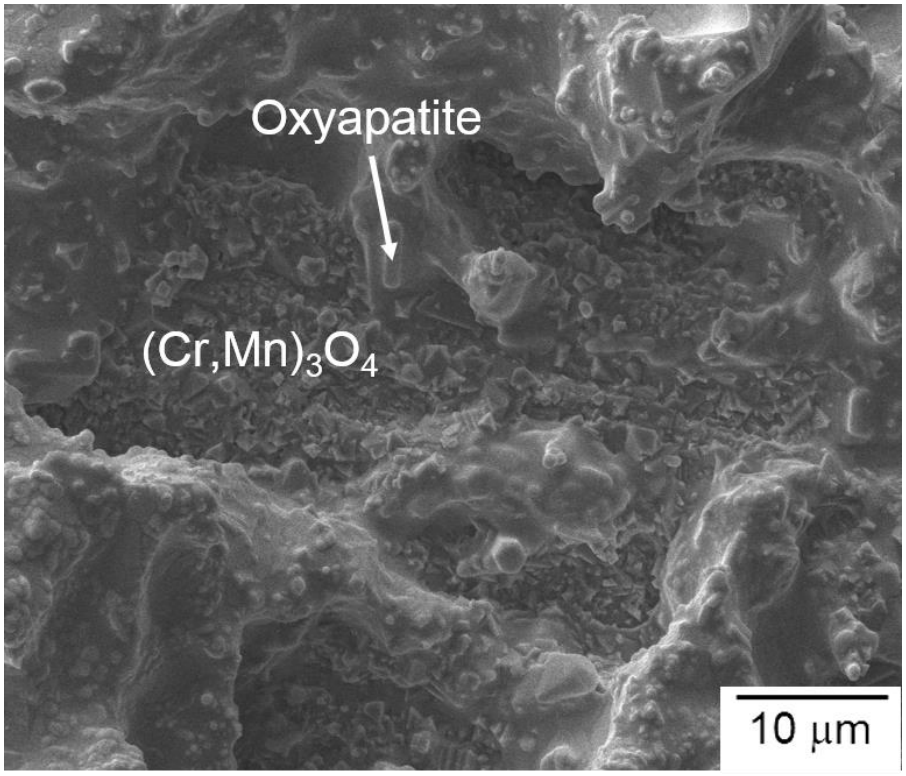

(c)

Fig. 46 (continued)

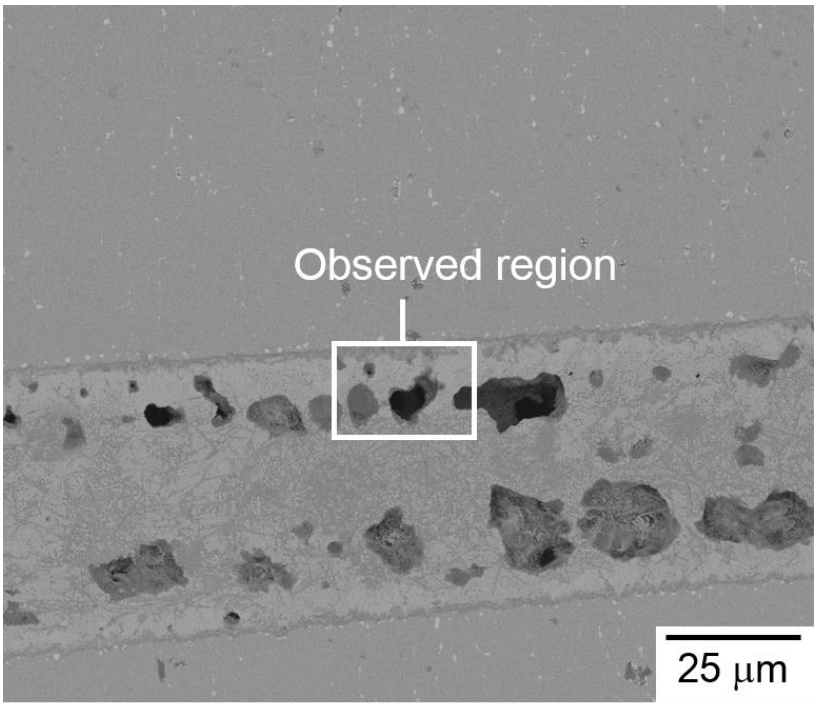

(a)

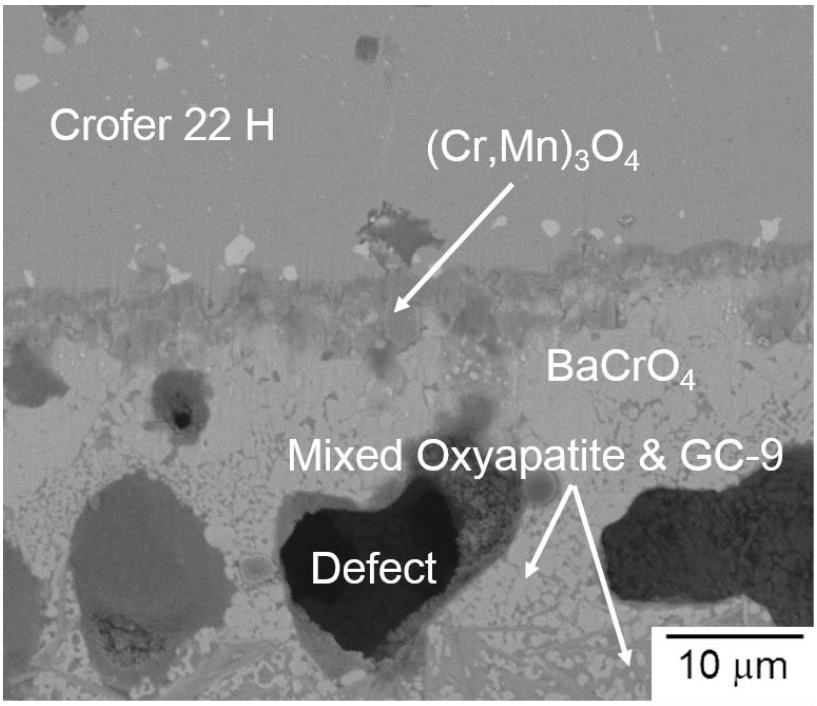

(b)

Fig. 47 Cross-sectional SEM micrographs (BSE mode) of the interface between GC-9 and Crofer 22 H in a 1000 h-aged tensile specimen: (a) low-magnification view; (b) high magnification of the outlined region in (a).

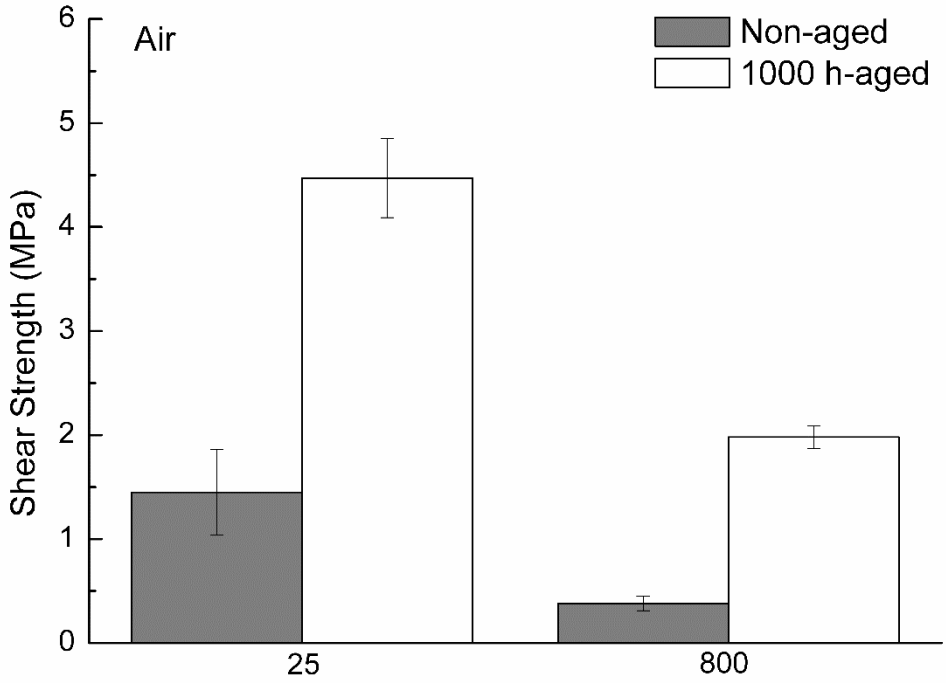

Fig. 48 Shear strength of non-aged and 1000 h-aged joint specimens tested in air at RT and 800 ℃.

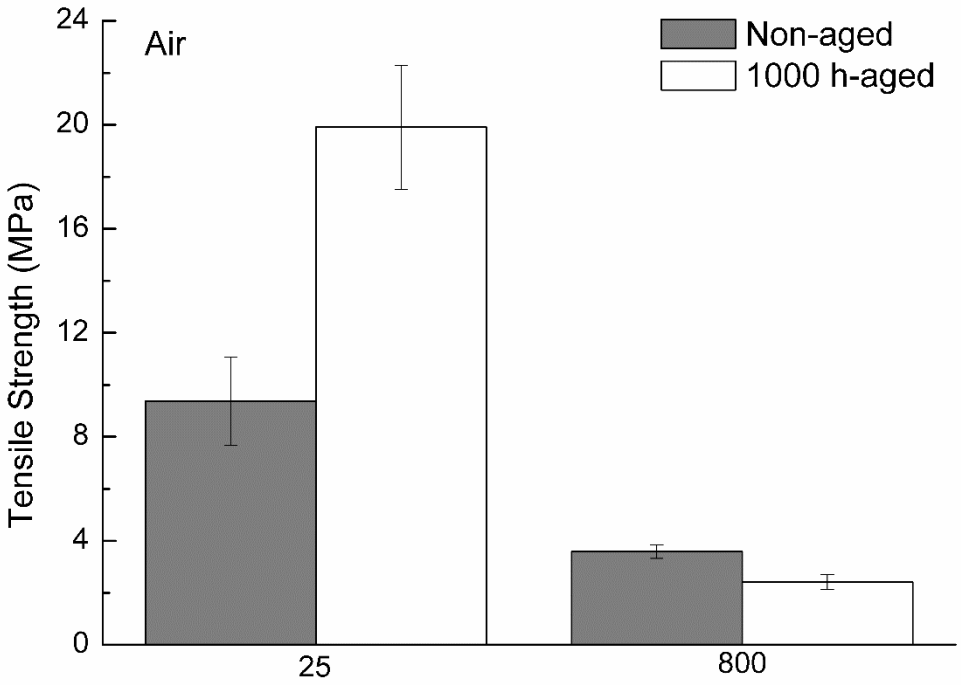

Fig. 49 Tensile strength of non-aged and 1000 h-aged joint specimens tested in air at RT and 800 ℃.

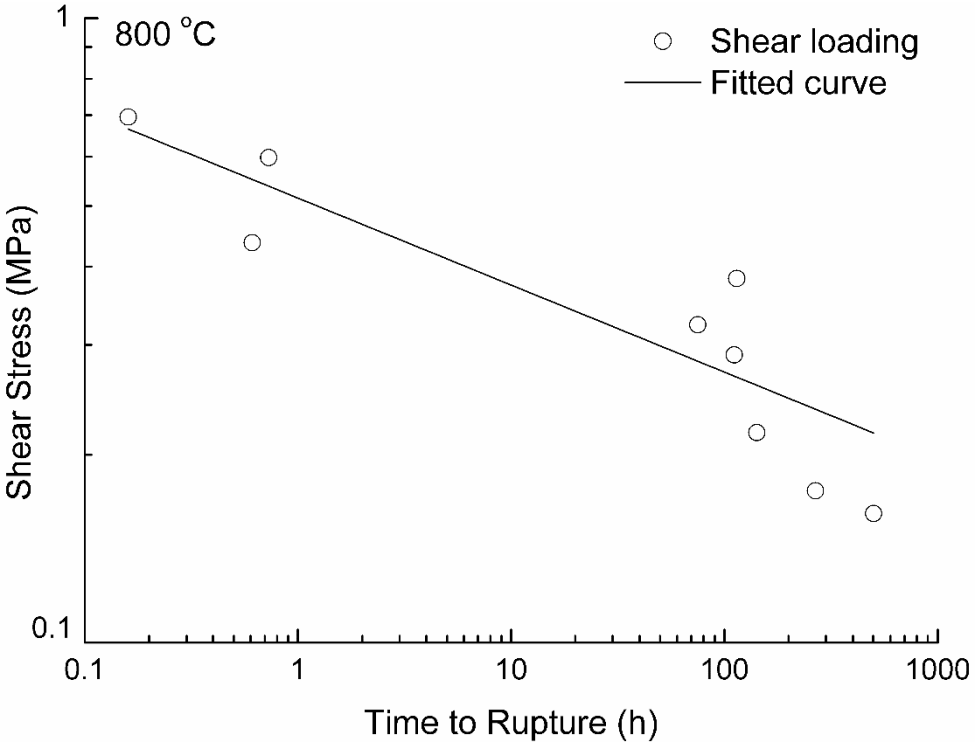

(a)

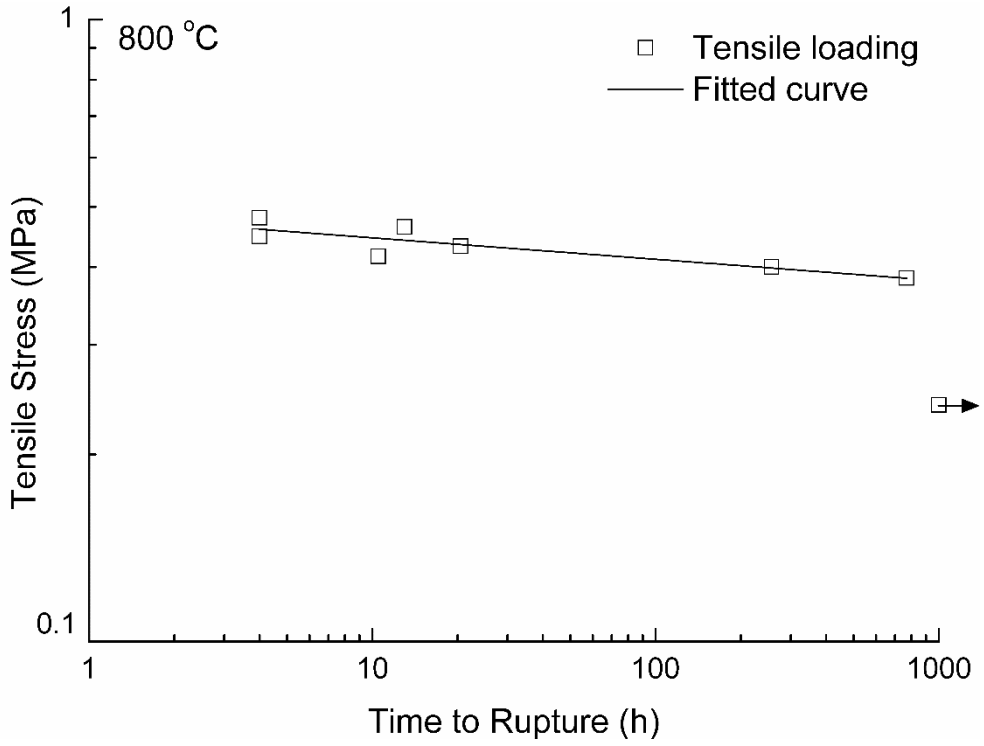

(b)

Fig. 50 Applied stress versus rupture time for 1000 h-aged joint specimens subjected to constant (a) shear and (b) tensile loading.

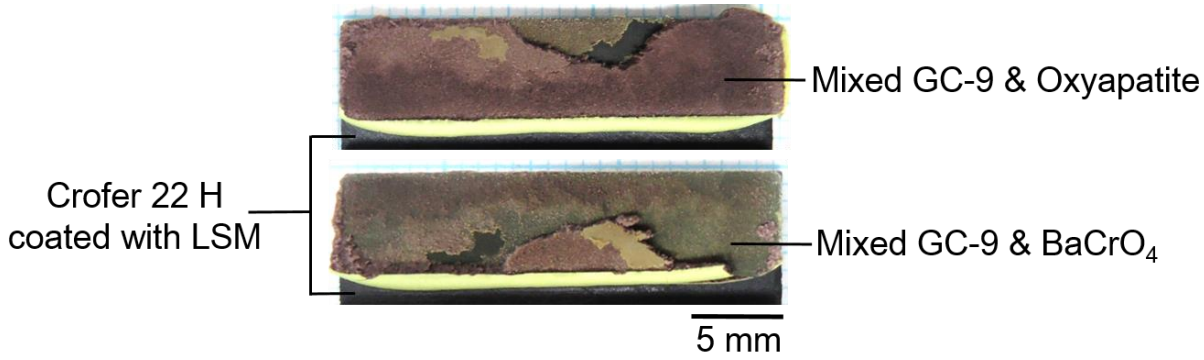

(a)

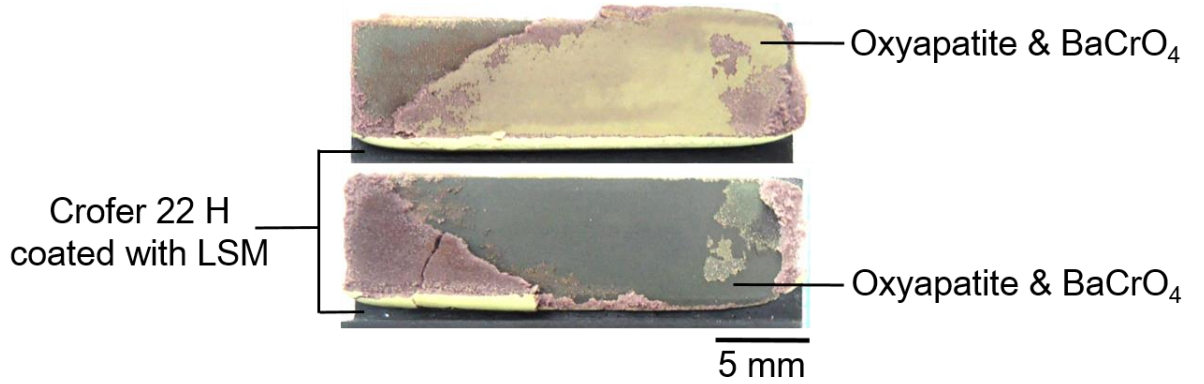

(b)

Fig. 51 Failure patterns in the 1000 h-aged shear specimens tested at 800 ℃ with various creep rupture times: (a) short creep rupture time; (b) medium-term creep rupture time.

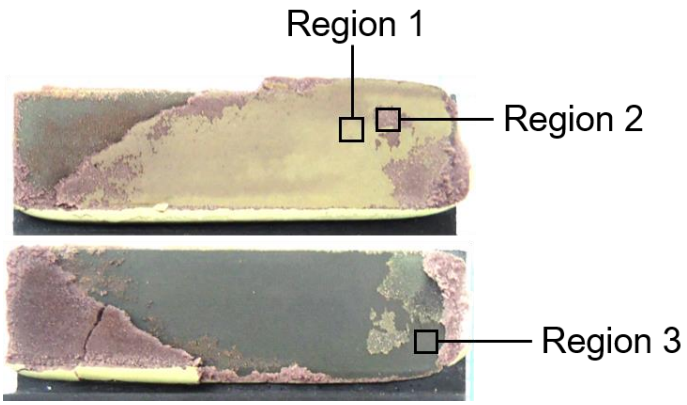

(a)

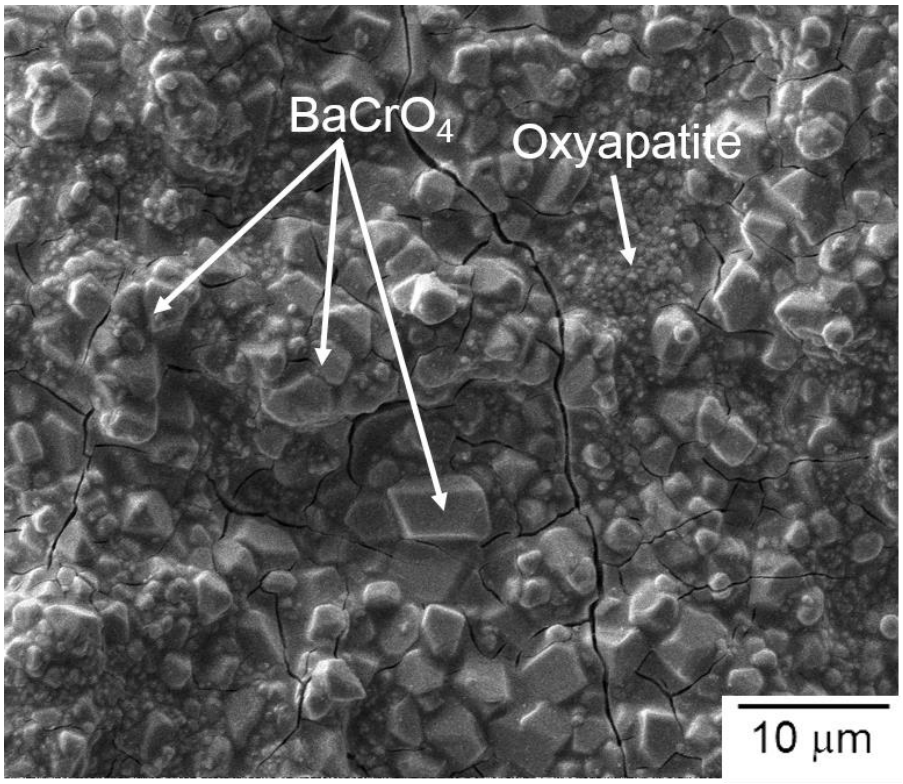

(b)

Fig. 52 Fracture surface of the 1000 h-aged shear specimen shown in Fig. 51(b): (a) optical micrograph showing the observed regions of SEM; (b) SEM micrograph of Region 1; (c) SEM micrograph of Region 2; (d) SEM micrograph of Region 3.

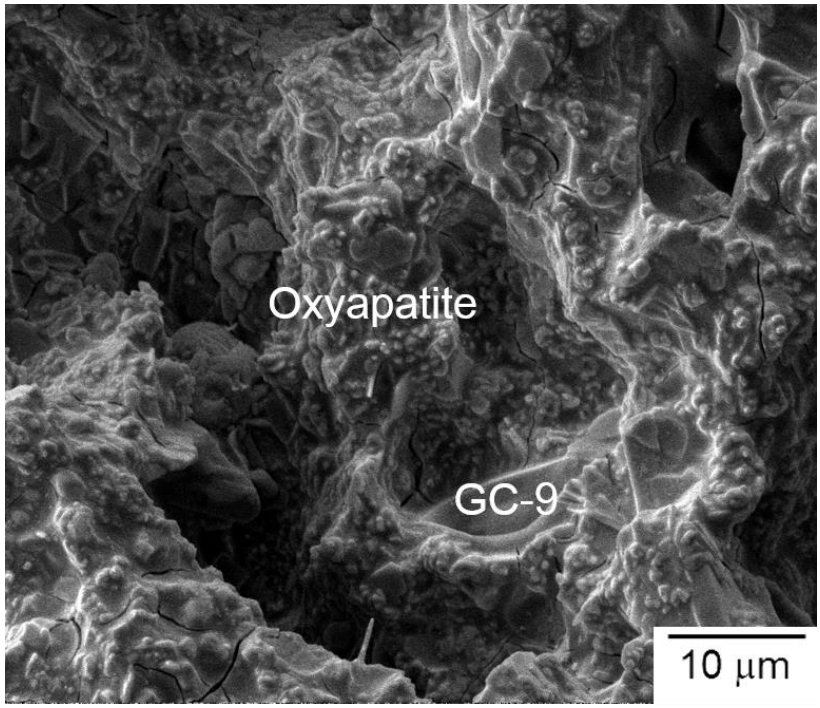

(c)

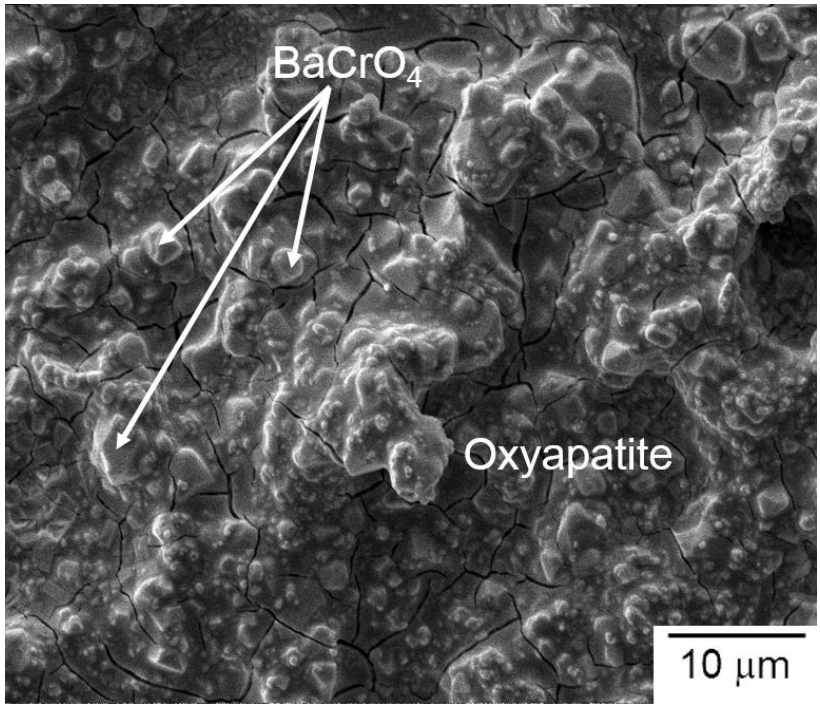

(d)

Fig. 52 (continued)

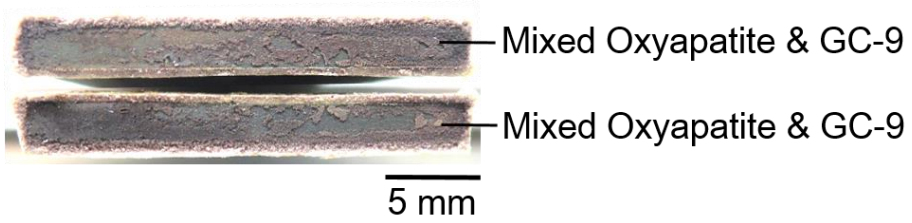

(a)

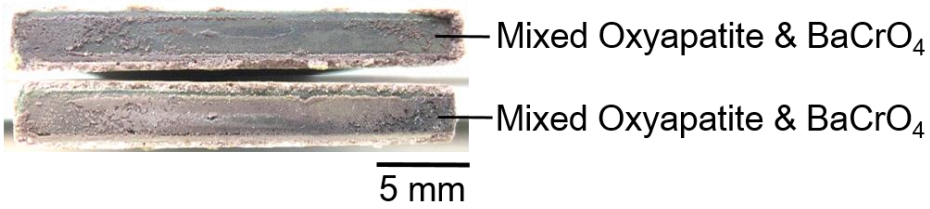

(b)

Fig. 53 Failure patterns in the 1000 h-aged tensile specimens tested at 800 ℃ with various creep rupture times: (a) short creep rupture time; (b) medium-term creep rupture time.

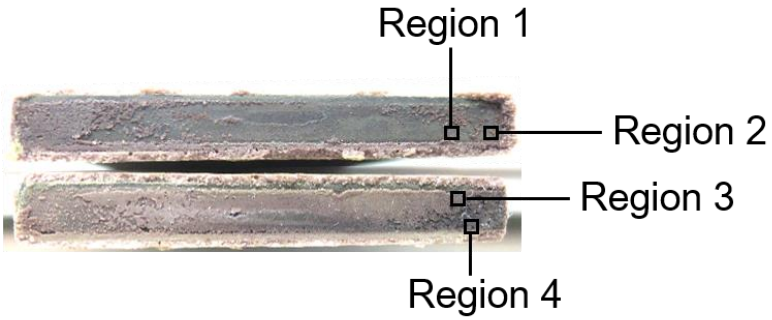

(a)

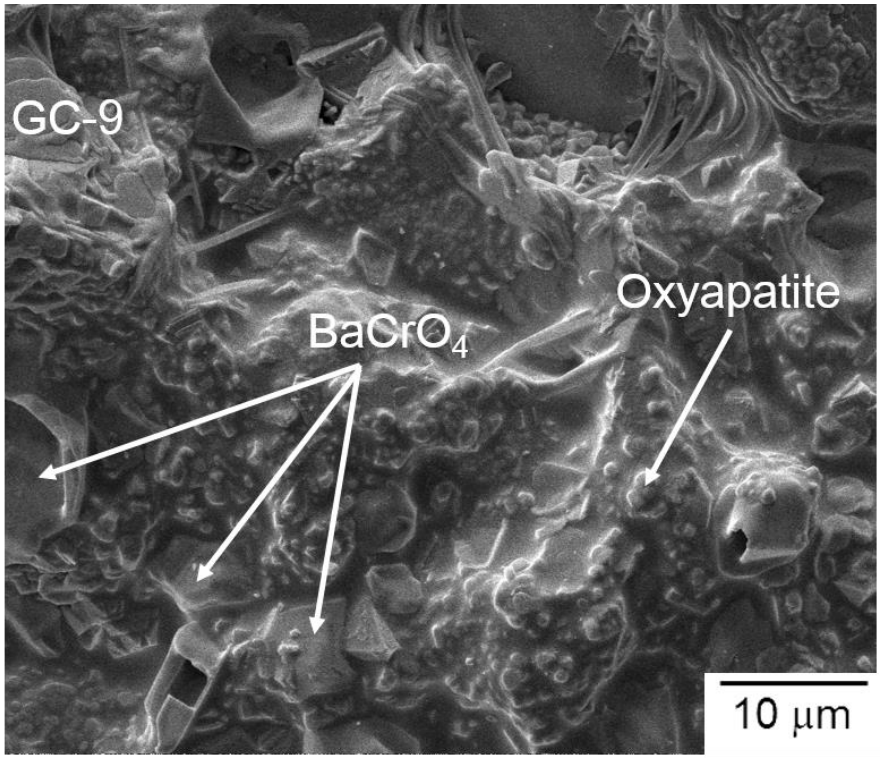

(b)

Fig. 54 Fracture surface of the 1000 h-aged tensile specimen shown in Fig. 53(b): (a) optical micrograph showing the observed regions of SEM; (b) SEM micrograph of Region 1; (c) SEM micrograph of Region 2; (d) SEM micrograph of Region 3; (e) SEM micrograph of Region 4.

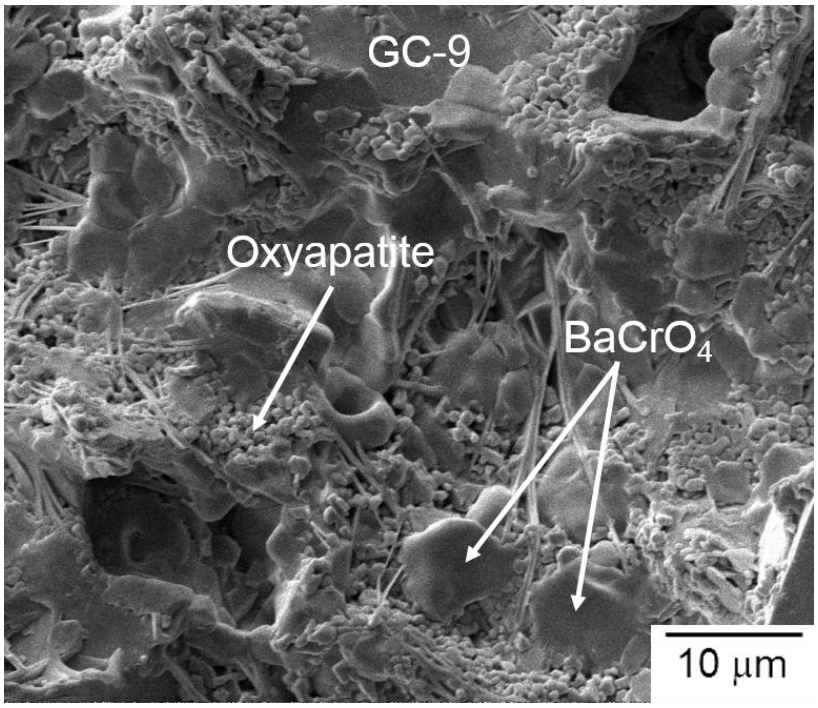

(c)

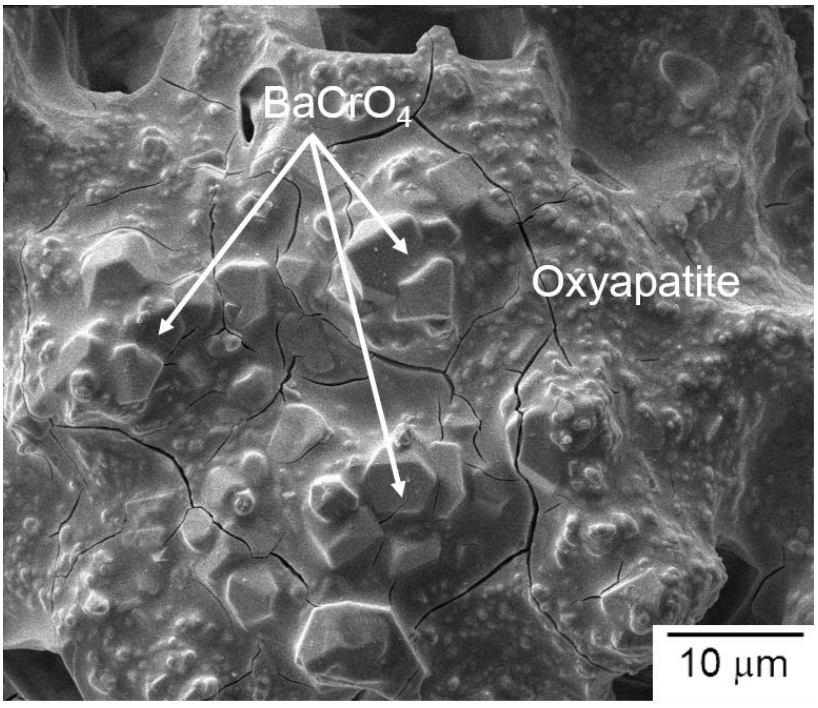

(d)

Fig. 54 (continued)

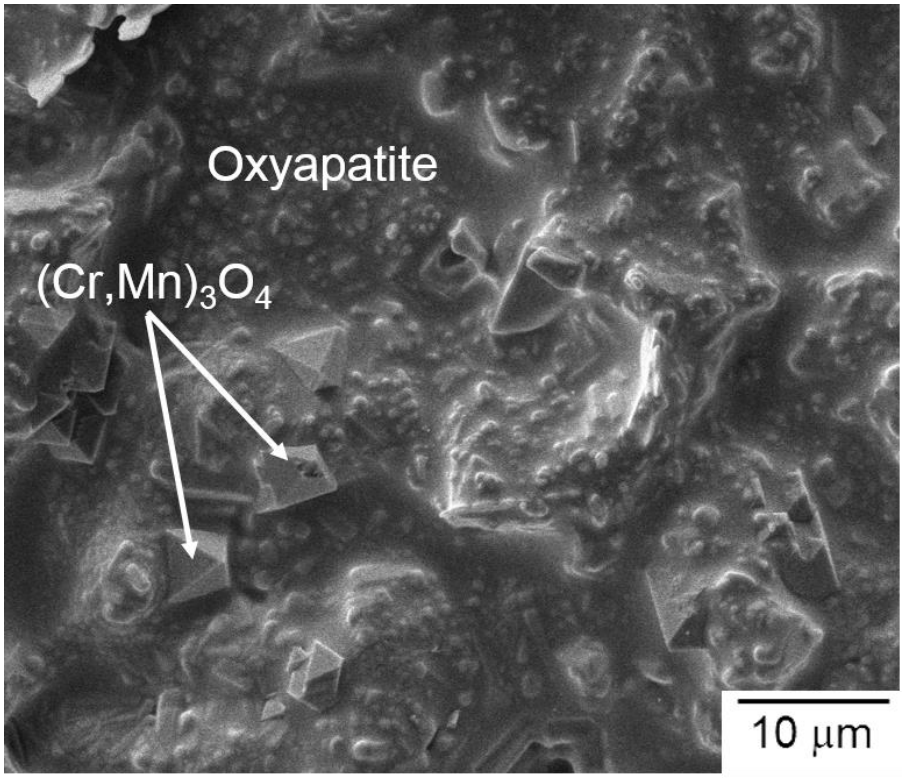

(e)

Fig. 54 (continued)

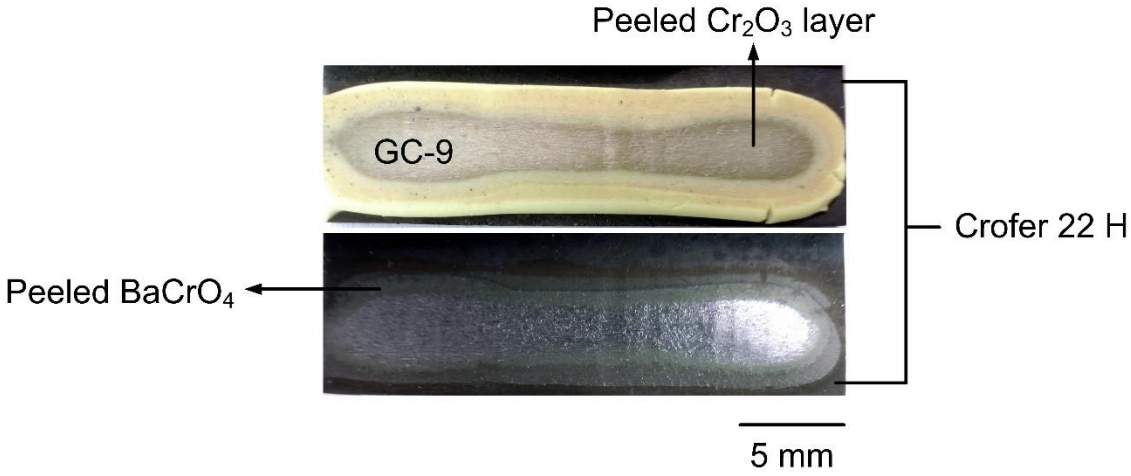

(a)

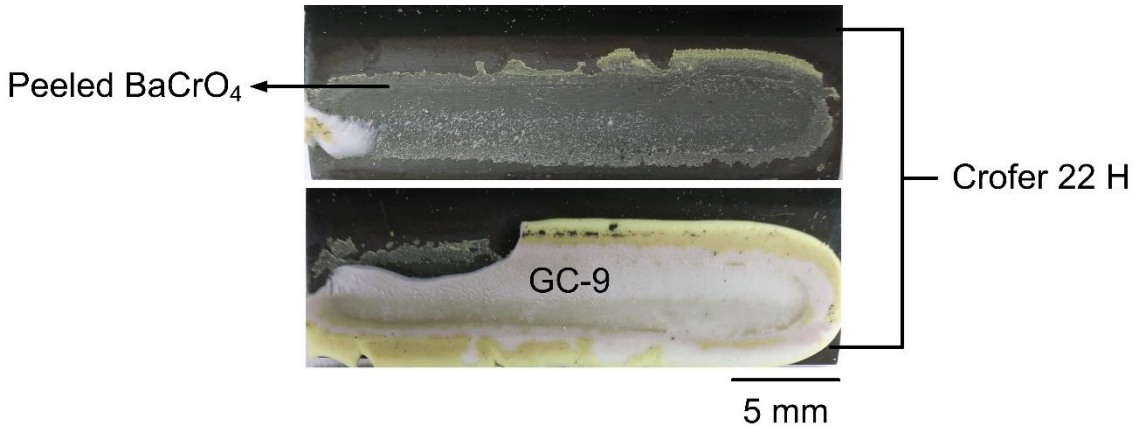

(b)

Fig. 55 Failure patterns of non-aged, non-coated shear specimens tested in air at (a) RT and (b) 800 °C. [56]

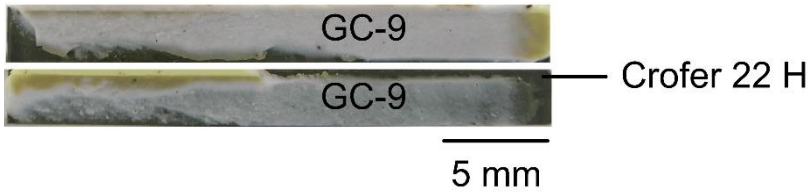

(a)

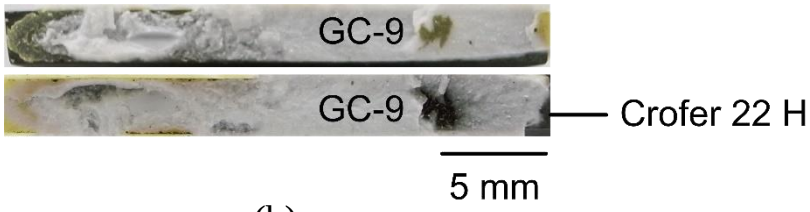

(b)

Fig. 56 Failure patterns of non-aged, non-coated tensile specimens tested in air at (a) RT and (b) 800 ℃. [56]

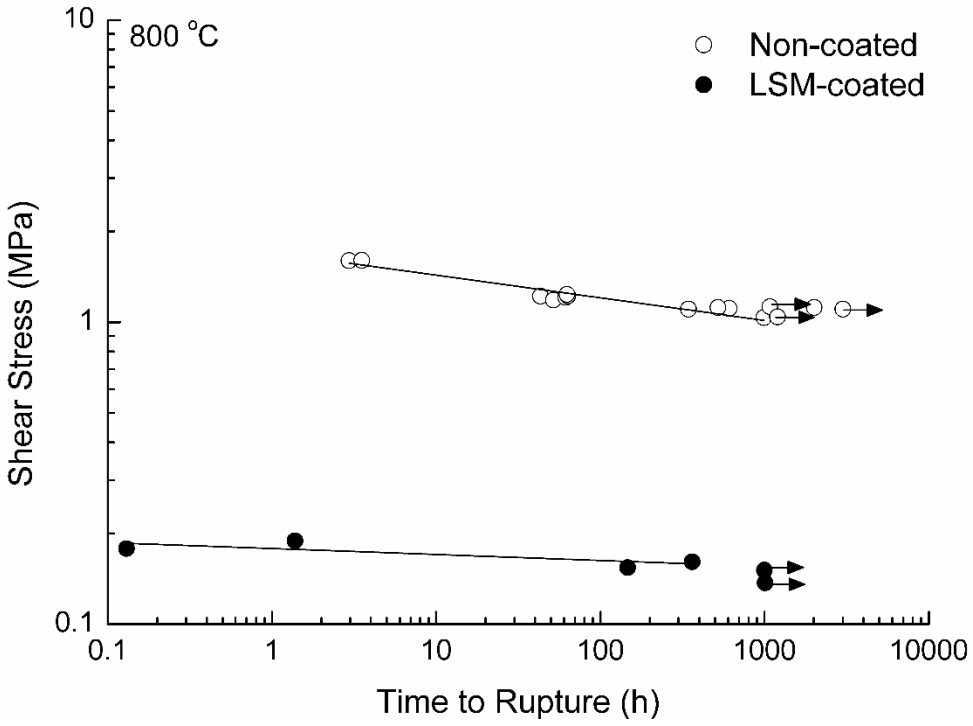

(a)

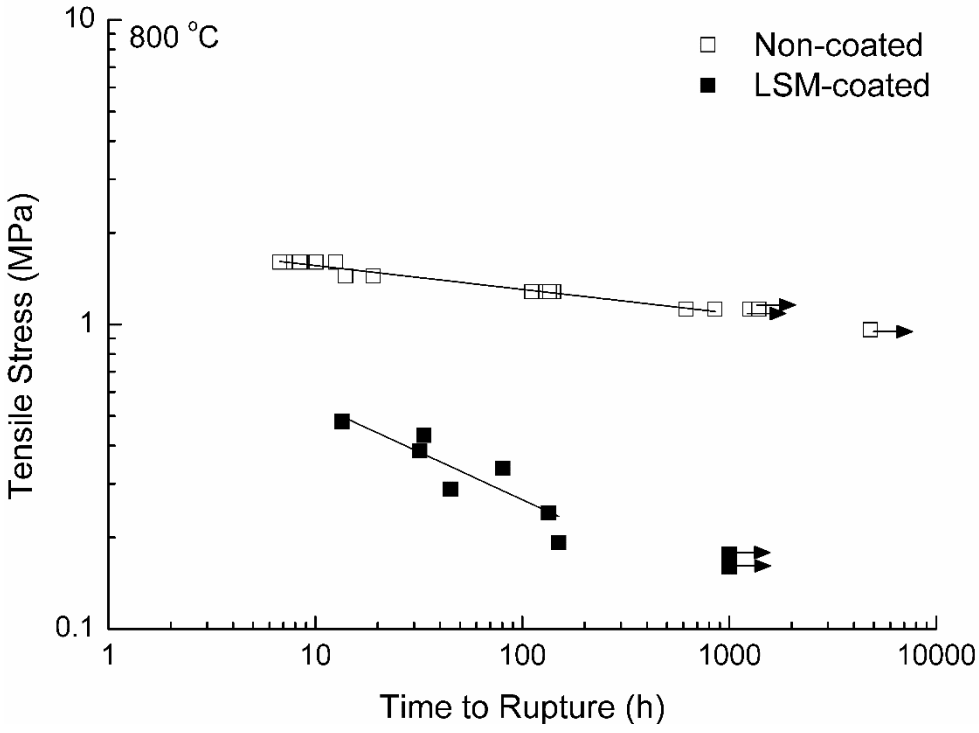

(b)

Fig. 57 Applied stress versus rupture time for non-coated and LSM-coated joint specimens under constant (a) shear and (b) tensile loading. (Arrow indicates the specimen was not ruptured when the test was terminated. The non-coated data are taken from Ref. [33].)

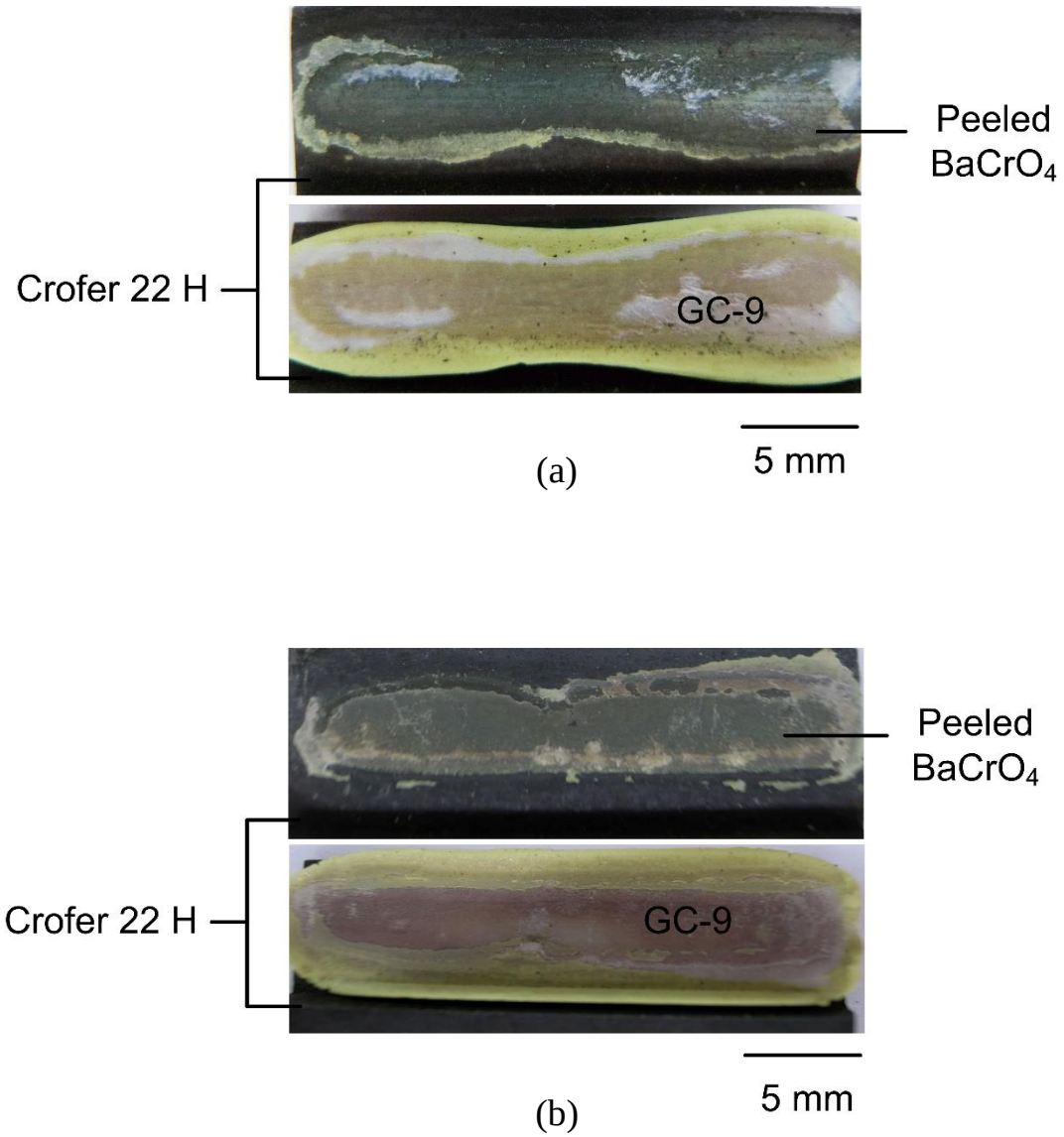

Fig. 58 Failure patterns in the non-aged, non-coated shear specimens tested at 800 °C with various creep rupture times: (a) short creep rupture time; (b) medium-term creep rupture time. [33]

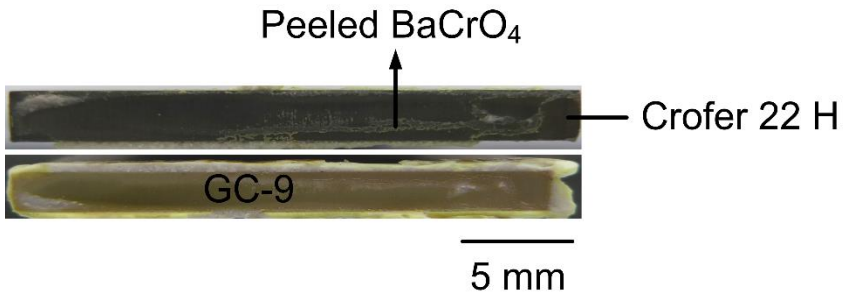

(a)

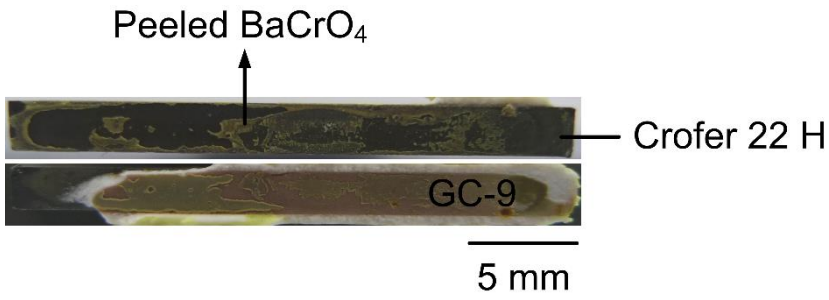

(b)

Fig. 59 Failure patterns in the non-aged, non-coated tensile specimens tested at 800 ℃ with various creep rupture times: (a) short creep rupture time; (b) medium-term creep rupture time. [33]

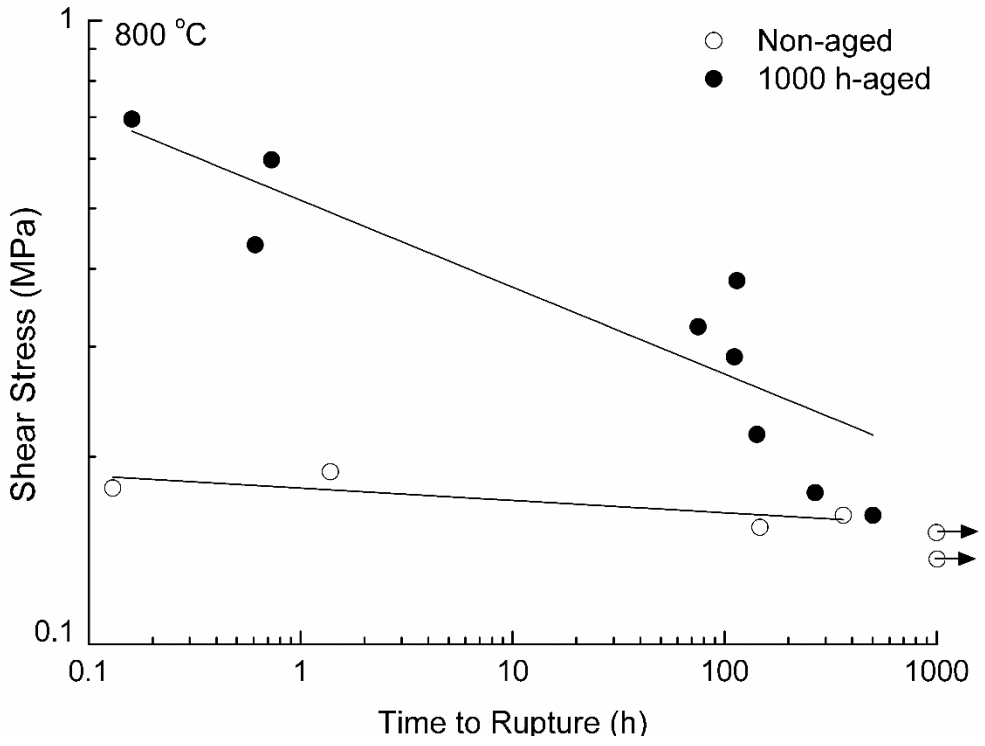

(a)

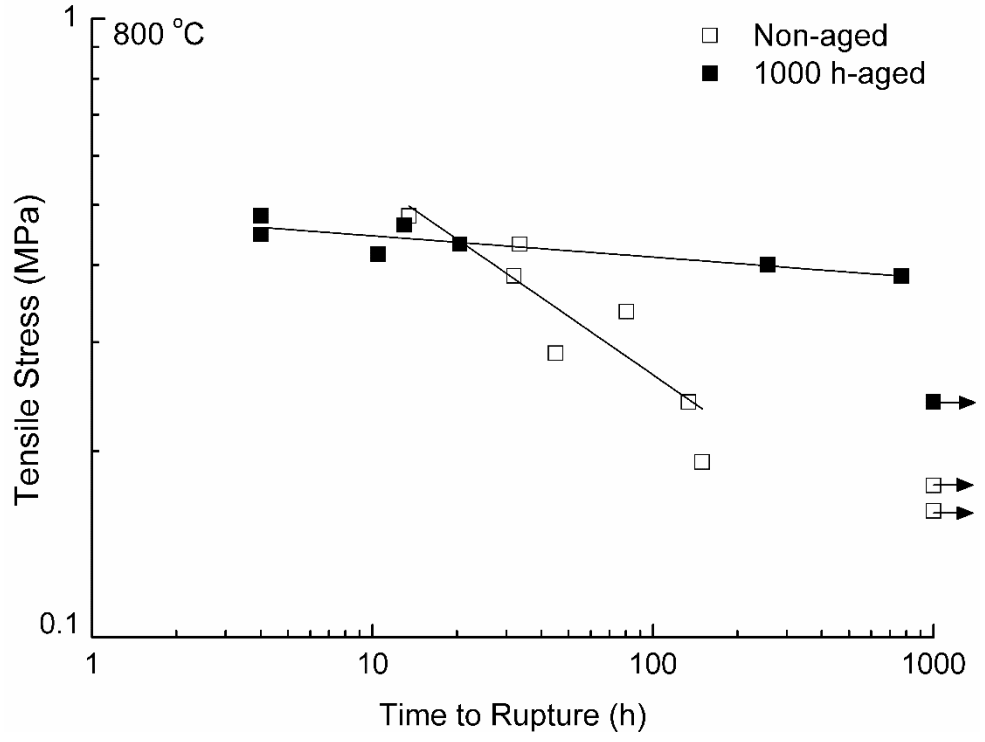

(b)

Fig. 60 Applied stress versus rupture time for non-aged and 1000 h-aged joint specimens under constant (a) shear and (b) tensile loading. (Arrow indicates the specimen was not ruptured when the test was terminated.)

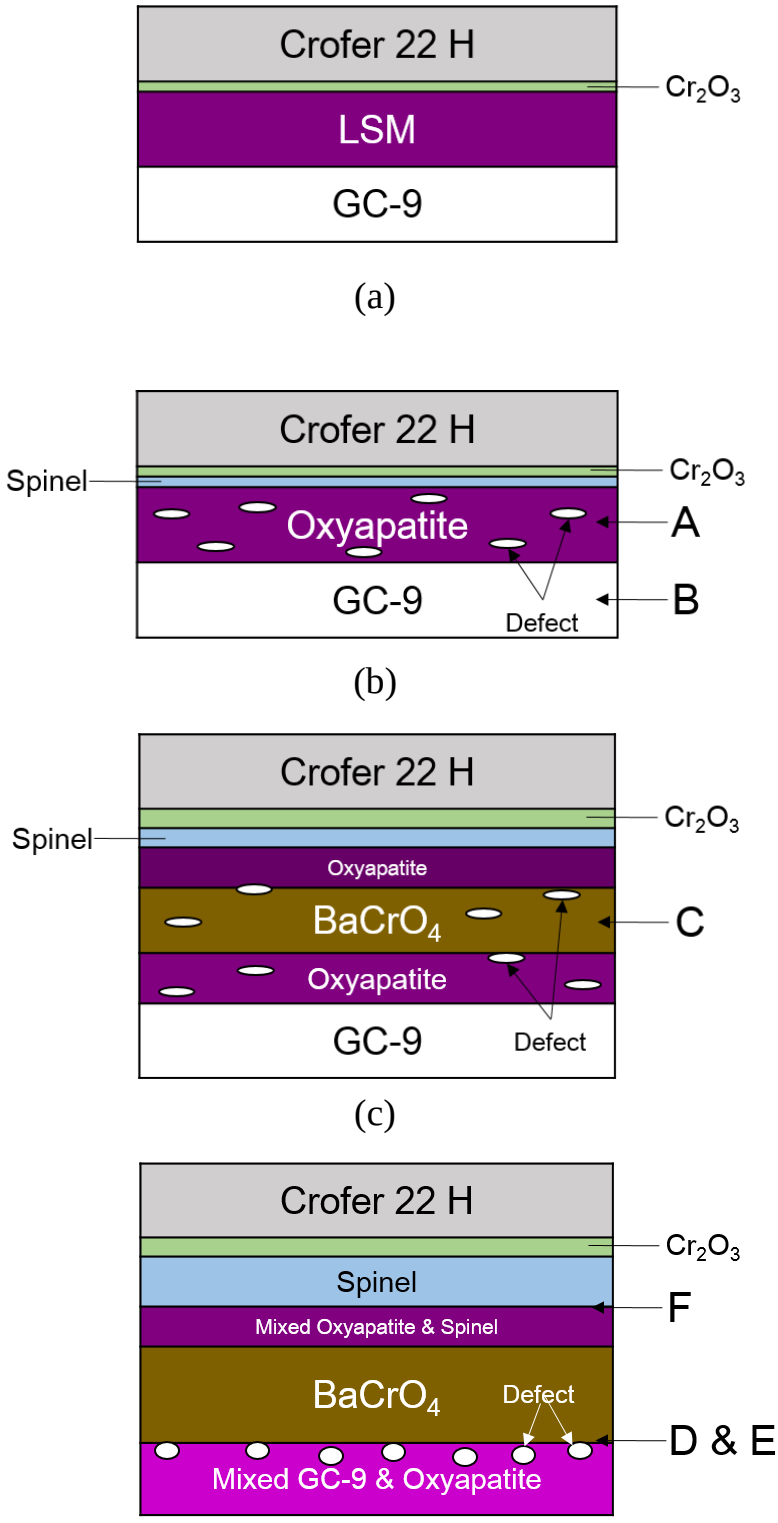

Fig. 61 Schematic diagrams of cross section of joint specimens: (a) as-assembled specimen before sintering; (b) non-aged specimen (as-joined after sintering); (c) non-aged specimen with a medium-term creep rupture time; (d) 1000 h-aged specimen. (Letters A-F represent various fracture sites.)